THE LARGE-EDDY SIMULATION OF INCOMPESSIBLE FLOWS IN SIMPLE AND COMPLEX GEOMETRIES

by

Stephen A. Jordan

Dissertation Submitted to the Faculty of the
Virginia Polytechnic Institute and State University in
Partial Fulfillment of the Requirements for the Degree of

DOCTOR OF PHILOSOPHY

in

Engineering Mechanics

APPROVED:

Dr. Saad A. Ragab, Chairman

Dr. Demetri P. Telionis

Dr. William J. Devenport

Dr. Scott L. Hendricks

Dr. Robert A. Heller

August, 1994

Blacksburg, Virginia

THE LARGE-EDDY SIMULATION OF INCOMPRESSIBLE FLOWS IN SIMPLE AND COMPLEX GEOMETRIES

by

Stephen A. Jordan

Committee Chairman: Dr. Saad A. Ragab

Department of Engineering Science and Mechanics

ABSTRACT

A large-eddy simulation methodology (LES) has been developed for predicting the turbulent physics of an incompressible flow in simple and complex geometries. The Cartesian form of the governing equations was first verified, and then later used to investigate a three-dimensional shear-driven cavity flow. The investigation involved Reynolds numbers of 2000, 3200, 5000 and 10000 and focused on the unsteadiness and turbulent characteristics of the flow. At the low Reynolds numbers ($Re \leq 5000$) where the cavity flow is fully laminar, direct numerical simulations (DNS) were conducted whereas the LES methodology was adopted to predict the cavity flow at the higher Reynolds number ($Re = 10000$). Determining the parameters in the damped subgrid scale (SGS) turbulence model for this complex flow was guided by the DNS results at $Re = 5000$. The SGS model was also verified against DNS results at $Re = 7500$ where the cavity flow was known through laboratory experimentation to be locally transitional. The LES results using the damped SGS model verified the published experimental evidence as well as uncovered new flow features within the cavity.

LES computations were also carried-out of the three-dimensional shear-driven cavity flow at a high Reynolds number where the SGS turbulent field was represented by a dynamic model. Lilly's least-squares expression was tested for determining Smagorinsky's coefficient in the model without *ad hoc* measures such as ensemble-averaging or filtering. However, zero cutoff of negative total viscosity (kinematic plus turbulent eddy viscosity) was necessary to maintain stable solutions. A discretized filter function was derived for the

test filter. Both qualitative and quantitative comparisons to experimental data show that the dynamic model performed quite well. The dynamic model gave better comparisons to the experimental evidence than the damped model did.

Vortex formation in the wake of a circular cylinder and their subsequent downstream transport was also numerically investigated by LES. Here however, the curvilinear form of the governing equations was necessary to perform the computations. A new generalized dynamic model was derived to represent the SGS stress field in the curvilinear space. This new model introduced the contravariant velocity components as part of the field variables. New downstream boundary conditions were also formulated to permit the shed vortices to exit with minimum disturbance. The focus of the investigation was at Re = 5600 with some verification of the computations at Re = 200 and Re = 3000. At all of these Reynolds numbers, the upstream boundary layer was laminar but the wake was fully turbulent at Re = 3000 and Re = 5600. The LES results of the many interesting characteristics of the wake showed good comparisons to the experimental data.

ACKNOWLEDGMENTS

The author of this dissertation is deeply grateful to the long term training committee at the Naval Undersea Warfare Center in Newport, RI for selecting him as a candidate for Ph.D. studies at Virginia Tech. The author is also indebted to Dr. Ragab, who displayed unprecedented patience during his long distance candidacy. Ms. Cindy Hopkins at Virginia Tech is commended for her dedicated cooperation toward insuring his continuous registration. The reviews and comments of the Ph.D. committee members have been most helpful. The support and patience of his direct superiors at the Naval Undersea Warfare Center is also appreciated (Cliff Curtis and Bob White). This author wishes to thank his friends and relatives for their support; in particular, his father and mother (Arthur and Marilee Jordan).

This work was supported by the Office of Naval Research (Dr. Pat Purtell, Science Officer) under Contract No. N0001494-WX23045 and the Independent Research Program (Dr. Ken Lima, Coordinator) at the Naval Undersea Warfare Center. Their continuous financial support is greatly appreciated.

TABLE OF CONTENTS

LIST OF TABLES

LIST OF FIGURES

CHAPTER ONE
INTRODUCTION

1.1. *The Large-Eddy Simulation*

The subject of this dissertation is the numerical simulation of turbulent incompressible flows. In the engineering field of computational fluid dynamics (CFD), three methods are commonly employed to solve incompressible turbulent flows; Reynolds-averaged Navier-Stokes approach, direct numerical simulation and large-eddy simulation. These methods differ principally in their representation of the turbulent physics. Traditionally, turbulent flow solutions of practical importance are achieved using the Reynolds-averaged Navier-Stokes (RANS) approach since only the mean flow quantities are resolved by the numerical scheme. All turbulent scales are represented by a phenomenological closure model. The available turbulent models vary extensively in complexity. In particular, they range from simple algebraic eddy viscosity relationships to complex formulations which involve several additional differential equations that greatly intensify the computational effort (for a review see Ferziger, 1985). Regardless of its complexity however, each model carries a set of empirical constants whose values are usually found by comparisons with experiments on simple flows. Consequently, one can not expect the results from a RANS computation to yield the fine-scale physics of the turbulent field. To achieve that end, one must choose an alternate method.

Instead of employing modeling, one could fully resolve the turbulent physics by direct numerical simulation (DNS). Here, the time-dependent three-dimensional Navier-Stokes equations are numerically solved for all relavant scales of the turbulent fluid motion. This approach requires the numerics to spatially and temporally resolve the turbulence down to at least the dissipative scales. For practical applications therefore, where the geometries are typically irregular and the flow characterized by a high Reynolds number (Re), the DNS approach is far beyond our best super-computer capacity. Currently, DNS computations are most utilized for providing insight into the fine-scale turbulent physics of low Reynolds number flows in simple geometries. Furthermore, DNS results have helped develop and validate turbulence models as well as complement experimental testing. Future expectations of the DNS

approach is projected by Peterson et al. (1989) in Fig. 1.1. Based on the current advancement of supercomputers in 1989, they projected the usefulness of DNS for practical applications to extend well into the next century.

A viable alternative for fine-scale computation of the general class of turbulent flows is the large-eddy simulation (LES). Unlike DNS, only the larger energy-containing eddies are fully resolved by the numerics which significantly reduces the computational demand. The smaller turbulent eddies, located within the subgrid scales (SGS), are modeled. Since today's modeling efforts assume the turbulence to be in equilibrium within the SGS range (production equals dissipation), use of simple algebraic eddy viscosity relationships are common. These models typically possess coefficients whose local magnitudes must be sufficient to properly dissipate the turbulent energy at the SGS level. Otherwise, energy "build-up" in the small scales will occur which could lead to divergence.

Treatment of the turbulent scales in the LES approach can be viewed as a compromise between the RANS and DNS methods. In Fig. 1.2, we can imagine ourselves beginning at the DNS end of the turbulent energy spectrum (at dissipation wavenumber k_d) and then moving left towards the RANS end (zero wavenumber). Along the way, we carry a turbulence model that is increasing in complexity. Currently, accurate SGS modeling of the fine-scale turbulent physics stops at the inertial subrange. For the simplest case involving isotropic and homogeneous turbulence which is shown in Fig. 1.2, the state-of-the-art has succeeded in modeling down to the lower-end of the inertial subrange. On the other hand, successful modeling of complicated turbulent flows probably lies close to the upper-end of the inertial subrange. It is important to note that the LES methodology has historically benefited from DNS and RANS independent achievements. The development of stable higher-order schemes over fine grids as required for DNS computations and the continuing effort towards attaining a universal turbulence model for RANS analyses provide valuable input into improving LES. By projecting Fig. 1.1 beyond 1994, we can expect routine LES solutions of moderately difficult engineering problems (such as the airfoil) by the year 2000.

1.2. *Relevant Historical Works*

One of the earliest engineering works of LES was performed by Deardorff (1970) who focused on a three-dimensional incompressible fully-developed channel flow. He used a primitive variable formulation coupled with Smagorinsky's (1963) algebraic eddy viscosity model for the SGS turbulent field. This model represents the SGS stress field as a product of the turbulent eddy viscosity and the strain-rate tensor. Although a relatively coarse grid was used in his simulation (6720 computational points), comparisons to the experimental measurements were quite good. His results brought strong attention to the LES technique as a viable source for predicting turbulence. Deardorff's work was followed by Schumann (1975) who improved the SGS model and implemented a much finer grid (65536 computational points). Schumann's work marked a significant improvement over Deardorff's results for the incompressible turbulent channel flow problem.

Both Deardorff and Schumann approximated the channel wall layer dynamics by a boundary condition based on the logarithmic law-of-the-wall. Continuing with the same test problem, Moin et al. (1978) integrated the LES equations down to the channel wall using a stretched grid. The subgrid scales were represented by Smagorinsky's model. Except for very near the wall where streaking and bursting dominate the flow behavior, their simulation produced results in fairly good agreement with the experimental data. Following an idea by Schumann (1975), Moin and Kim (1982) decomposed the SGS turbulence model into two components to better approximate the near-wall channel flow behavior. In primitive variables, their model consisted of a homogeneous isotropic part, similar to Smagorinsky's model, and an inhomogeneous component which accounted for a poor spanwise resolution in the channel. Furthermore, the homogeneous part was modified by a van Driest (1956) damping function to simulate the asymptotic behavior of the shear stress near the no-slip channel walls. A similar damping function was also incorporated into the eddy viscosity definition for the inhomogeneous component. Using a hyperbolic tangent function to vary the grid spacing from the walls, Moin and Kim were able to predict coherent structures of low- and high-speed streaks alternating in the spanwise directions. Speziale (1985) however showed that the splitting of their SGS model was not form-invariant under a Galilean

transformation and is thus incompatible with the basic physics of the problem. Other applications of the LES methodology for the incompressible turbulent channel flow problem include those of Moin and Kim (1980) and Kim and Moin (1981).

An important physical phenomenon of turbulent flow that must be captured by LES is the energy cascade process. Leonard (1974) points out that considerable "damming-up" will occur within the smallest scales of the resolved field if the SGS model does not sufficiently dissipate the transfer of turbulent energy to the subgrid scales. Solving Burgers equation over both coarse and fine grids, Love and Leslie (1979) showed that subgrid modeling can reproduced the most significant features of turbulent energy transfer from the resolved to the subgrid scales whether a simple or more complicated algebraic SGS model is implemented. Taken together, Clark et al. (1977) and Mansour et al. (1979) assessed several models through simulation of the decay of homogenous isotropic turbulence. In Clark et al., four SGS models were evaluated that ranged in complexity from a simple constant eddy viscosity to Smagorinsky's relationship. They concluded that the best overall performance came from Smagorinsky's model, but that all four were surprisingly satisfactory for predicting high Re turbulent flows.

Mansour et al. (1979) used a rotational form of the governing LES equations as well as primitive variables. Their SGS model was similar to one tested by Clark et al., but was formulated from the resolved rotational tensor rather than the strain-rate tensor as in Smagorinsky's model. With respect to the experimental data (Comte-Bellot, 1970), both the primitive variable and rotational forms of the LES equations produced accurate profiles of the turbulent energy spectra. Although their predictions using each form were nearly indistinguishable, Mansour et al. concluded that the rotational form is better suited for predicting free shear flows while wall shear is handled more accurately by primitive variables.

To find many other early works (before a decade ago) that demonstrate the favorable aspects of the LES methodology as a useful prediction tool for incompressible turbulent flows, one should consult reviews by Rogallo and Moin (1984), Ferziger (1985) and Reynolds (1991). A brief overview of early subgrid scale modeling ideas is presented in Herring (1979).

Over the past decade LES has receive considerable recognition which has lead to its vastly expanded capabilities for resolving incompressible turbulent flows. In the work by Shao et al. (1990) for example, LES computations were performed of a shearless turbulent mixing layer with an SGS model proposed by Chollet and Lesieur (1981). Shao et al. compared their LES results to two separate RANS computations that involved either a Reynolds stress tensor (RST) or a K-ε turbulent closure model. They intended to validate the respective RANS model constants. Shao et al. found that the recommended empirical value for the constants C_s (RST) and C_m (K-ε) in the triple correlation relationship were grossly under-estimated. In a separate application, a two-point closure theory, called the Eddy Damped Quasi-Normal Markovian (EDQNM), was compared to LES predictions by Chollet (1984) to assess the energy distribution in the subgrid scales as well as the energy transfer between the resolved and subgrid scales. Chollet concluded that the foregoing concepts of eddy viscosity for SGS modeling were well justified. Metais and Lesieur (1989) also compared LES results to EDQNM and to DNS numerical data involving the decay of homogeneous isotropic turbulence. Their conclusion agreed with that of Chollet.

Transition to turbulence in the plane channel was investigated by Zang and Piomelli (1990). They studied the mechanism of energy backscatter from the subgrid scales to the finer resolved scales. Three SGS models were tested; namely, Smagorinsky's with van Driest damping, the renormalization group theory (RNG) model (Yakhot, and Orszag, 1986), and a version of Smagorinsky's model but with the model coefficient computed dynamically from the finest scales of the resolved instantaneous velocity field. Although each model predicted transition surprisingly well, the dynamic model proved to be the most accurate. In this dissertation, further details about SGS modeling is presented under a chapter five.

Recently, researchers have challenged LES to complex problems that have more practical implications. For example, a backward facing step flow, which is a popular benchmark for testing the accuracy of new numerical schemes, has been separately solved by Morinishi and Kobayashi (1990), Karniadakis et al. (1990) and Akselvoll and Moin (1993) using the LES technique. In the simulation by Morinishi and Kobayashi, artificial wall boundary conditions

with a rather coarse grid were employed. Despite these conditions however, their prediction of the reattachment length and the streamwise mean velocity profiles after the step showed impressive agreement with the experimental data. Karniadakis et al. applied the RNG model in their LES computations of transitional flow over the backward facing step. They began the simulation near the initial stages of transition and ended in the full turbulence regime. Inasmuch as their results were preliminary, the transitional stages as seen in the experimental measurements were predicted qualitatively. Akselvoll and Moin (1993) solved the backward facing step problem using a dynamic localization model developed by Ghosal et al. (1992). They compared their LES results to the experimental measurements of Jovic and Driver (1992) and the DNS computations by Le and Moin (1992). The spatial resolution in the DNS computations was 32 times finer than the subsequent LES calculation. Akselvoll and Moin obtained satisfactory agreement with the DNS results as well as the experimental data, but at a substantial reduction in computational cost.

As other examples, Weiner and Wengle (1989), Ciofalo and Collins (1990) and Yang and Ferziger [1993) independently simulated turbulent flow behind a square rib placed periodically along the channel floor. Both Weiner and Wengle and Ciofalo and Collins represented the subgrid turbulence by Smagorinsky's model. Their predictions of the fluctuating rms velocity components behind the rib agreed qualitatively with the experimental data. Yang and Ferziger also implemented Smagorinsky's model, but computed the model response coefficient two separate ways; one by using the dynamic strategy and the other from a simple damping function. In addition, they performed fine-grid DNS computations to establish a data base for LES comparisons. Yang and Ferziger reported superior results by computing the model coefficient dynamically.

Lastly, a notable successful application of LES that dealt with a difficult geometry was reported by Schumann and Krettenauer (1992). They simulated turbulent convection over a sinusoidal undulated terrain at an infinite Rayleigh number. Their governing equations and SGS model were reformulated into a curvilinear coordinate framework to accommodate a boundary fitted grid to the wavy terrain. Before attacking the convection problem, Schumann and

Krettenauer first validated the predictive accuracy of their LES scheme against DNS computations at a much lower Reynolds number. They also compared their LES results to experimental data for turbulent convection over a flat surface at a high Rayleigh number. Their LES computations were extensive, and uncovered large three-dimensional motions generated by a two-dimensional wavy terrain that were previously unseen using two-dimensional simulations.

1.3. *Importance Of Present Effort*

The previous works just described unfold significant progress of LES since its inception only slightly more than two decades ago. This CFD approach has repeatedly demonstrated its ability to predict turbulent structures in complex flows. The improvements in high-order-accurate numerical schemes, SGS turbulence modeling and supercomputer technology contribute to this rapid success. The immediate future will undoubtedly center on characterizing backscatter routinely in the turbulence model. This characteristic is a necessary model ingredient when representing inhomogeneous turbulence. Backscatter physics deal with the reverse flow of turbulent kinetic energy up the cascade from the SGS model to the finest scales of the computed field. Dissipation, which is the other but dominate characteristic, is already well identified. Venturing modeling efforts towards non-equilibrium turbulence has only just begun.

Use of today's dynamic turbulence models (ones that permit energy backscatter as well as dissipation) is not a straightforward process. The dynamics manifest stability issues that have demanded various *ad hoc* measures to reach a successful implementation. In chapter five, a detailed account of the *ad hoc* measures commonly chosen is discussed. Usually, more than one measure is needed to stabilize the computation. Herein however, a complex flow problem is solved where all but one measure is eliminated. The problem selected is an incompressible turbulent flow in an enclosed shear-driven cavity. Excellent agreement was obtained between the predicted turbulent quantities and the experimental data using the dynamic model. For comparison, the cavity flow is also solved using a damped turbulence model which is strictly dissipative. Agreement between those results and the

experimental data is less encouraging. These simulations will clearly show the importance of dynamic SGS modeling for complex turbulent flows.

The impetus behind the present work is the practical application of LES to the general class of incompressible turbulent flows in complex geometries. Because most practical flow problems involve very complicated domains, use of simple coordinate systems require boundary interpolations that lead to unnecessary approximations. The physical geometries are generally quite arbitrary, such that special mapping procedures are more suitable when attempting to predict the associated flow. Thus, the computational technique presented here is focused on extending the current LES methodology to a curvilinear coordinate framework. This formulation permits LES solutions over structured grids mapped specifically to the complex domain and eliminates geometric interpolation when applying the boundary conditions. The penalty of the mathematical transformation however is additional terms in the LES equations. Besides the governing equations, the turbulence model is also transformed to curvilinear coordinates.

Herein, all details of the transformation are carefully covered. The resultant equations are formulated in a strong conservation-law form, but differ from previous works for the purpose of optimizing the solution efficiency using the algorithms developed and tested for the LES equations in Cartesian coordinates. The test case selected to verify the new LES formulation was the prediction of turbulent vortices in the near wake of a circular cylinder. A non-orthogonal curvilinear grid was necessary to effectively encompass the cylinder wake. Prior to flow separation along the cylinder surface, the boundary layer was laminar. The wake however was fully turbulent. Besides implementing the LES equations, the computation demanded several other important factors. For example, a transformed set of downstream boundary conditions were formulated to exit the vortices with minimum distortion. In addition, the dynamic SGS model was reformulated to the curvilinear space to quantify the turbulent eddy viscosity. In this new model, Smagorinsky's coefficient was determined in a unique fashion through use of both the physical and contravariant velocity components. Experimental data in the near wake was published for this flow from which comparisons were made. One should note

that this LES computation is a first of its kind and extends the potential of LES for practical use.

In the next chapter, the fundamental LES equations in Cartesian coordinates and solution method are presented in complete detail. In chapter three, the LES equations are reformulated into curvilinear coordinates for computations in complex domains. The equations are written such that no new solutions algorithms are necessary. Chapter four discusses important concerns of implementing boundary conditions for the velocity and pressure. The damped and dynamic SGS models as well as their implementation are presented in Chapter five. This chapter also gives all details for extending these models to the complex domains. The next two chapters comprise the results of two applications. Shear-driven cavity flow results are presented in Chapter six where the Cartesian form of the LES equations and SGS model was used in the computations. Chapter seven shows the results obtained using the curvilinear formulation for the LES equations and SGS model. The test problem is cross-flow over a circular cylinder. The dissertation closes with a recapitulation of the conclusions and a discussion of future work.

CHAPTER TWO
LES EQUATIONS AND SOLUTION METHODOLOGY

2.1. Introduction

Largely through the advancements in supercomputer technology, one can compute the fine-scale quantities of complex incompressible turbulent flows. The usefulness of the results strongly depends on resolving the most important scales of the turbulent field. The LES methodology offers one the flexibility of resolving as much of the turbulence as computationally permissible. This resolution is dictated by the grid point spacing and is assumed to include the predominant scales of the turbulent field. The remaining finer turbulence levels which lie below the grid's resolution are picked-up by a representative model.

Separation between the resolved and unresolved (or modelled) fields transpires through spatial filtering of the Navier-Stokes equations. Formally, the filter operation in three-dimensional physical space (x_i) is defined by the convolution integral

$$\overline{\Phi}(x_i) = \int \Phi(x_i')G(x_i, x_i')dx_i' \qquad (2.1)$$

where the overbar symbolizes the filtered variable Φ and $G(x_i, x_i')$ is the filter function. Investigators have explored Gaussian, sharp cut-off and box type filters. While the box filter is administered in the physical domain, the Gaussian and sharp cut-off filters are applied in wavenumber space. With the sharp cut-off filter, division between the resolved and modeled fields is distinct in the wavenumber space (see Fig. 2.1). All wavenumbers are resolved by the numerics up to the cut-off wavenumber (k_c), which corresponds to twice the grid point spacing; i.e. $k_i^r \le k_c = \pi / h$, where k_i^r are the resolved wavenumbers and h is the grid point spacing. Communication between the subgrid scale turbulence model and the numerics occurs only at the cut-off wavenumber. Conversely, the Gaussian and box filters attentuate the resolved field such that the energy transfer between the numerics and the SGS model takes place over a range of wavenumbers. The model's influence on the resolved field diminishes with decreasing wavenumber below cut-off.

2.2. LES Governing Equations

The mathematical system which governs unsteady incompressible turbulent flows is the Navier-Stokes (NS) equations and continuity. In index notation, the conservative non-dimensional form of this primitive-variable system in three-dimensional (3D) Cartesian coordinates is

$$\text{Momentum:} \quad \frac{\partial u_i}{\partial t} + \frac{\partial}{\partial x_j}\left(u_i u_j\right) = -\frac{\partial p}{\partial x_i} + \frac{1}{Re}\frac{\partial^2 u_i}{\partial x_j \partial x_j} \tag{2.2a}$$

$$\text{Continuity:} \quad \frac{\partial u_i}{\partial x_i} = 0 \tag{2.2b}$$

where the velocity vector $u_i = \langle u, v, w \rangle^T$ and p is the pressure. The Reynolds number Re = UL/ν where ν is the kinematic viscosity and U and L are the characteristic velocity and length scales, respectively.

Upon filtering equation (2.2), the governing LES equations for the resolvable turbulent field are

$$\text{Momentum:} \quad \frac{\partial \overline{u}_i}{\partial t} + \frac{\partial}{\partial x_j}\left(\overline{u}_i \overline{u}_j\right) = -\frac{\partial \overline{p}}{\partial x_i} + \frac{1}{Re}\frac{\partial^2 \overline{u}_i}{\partial x_j \partial x_j} + \frac{\partial \tau_{ij}}{\partial x_j}, \tag{2.3a}$$

$$\text{Continuity:} \quad \frac{\partial \overline{u}_i}{\partial x_i} = 0. \tag{2.3b}$$

where $\overline{u}_i$ and $\overline{p}$ are the filtered velocity and pressure, respectively. The subgrid stress tensor τ_{ij} arose due to filtering the non-linear term and is defined as $\tau_{ij} = \overline{u_i}\,\overline{u_j} - \overline{u_i u_j}$. This term depicts the subgrid turbulent scales of which a model is required.

2.3. Fractional-Step Method

2.3.1. General Dissusion

Basically, three numerical schemes are available for solving the LES equations in (2.3). One particular class of methods is founded on the fractional-step procedure (also called the projection method) proposed by Chorin (1969) over twenty-five years ago. This procedure capitalizes on Helmholtz's decomposition theorem in which the convection and diffusion components of the unsteady Navier-Stokes equations are together decomposed into the sum of a divergentless vector (velocity) and an irrotational vector (pressure gradient). Splitting the operators in this way permits the

introduction of an intermediate velocity which provides the only direct link between the pressure and physical velocity fields. The Navier-Stokes equations are replaced by a two-step process which involves solution of an unsteady convection-diffusion equation for the intermediate velocity followed by an update of the physical velocity field. In the original two-dimensional scheme by Chorin, the method of artificial compressibility was implemented to establish a separate equation for solution of the pressure variable. Given the intermediate velocity field, the physical velocity and pressure fields were successively updated until the iterations converged. Convergence was defined by the allowable error in the incompressibility constraint. At each time increment, many iterations were necessary to minimize that error. Herein, a variation of Chorin's original fractional-step method is utilized. But before presenting the details of the technique, alternate methods that one can choose for solving unsteady incompressible flows are discussed.

Full predictor-corrector type schemes have also been applied to unsteady incompressible flows. One approach (referred to as a pressure-based method) involves replacing the continuity equation with a pressure-Poisson type equation which is derived by taking the divergence of the momentum equation and invoking the incompressibility constraint. The pressure-Poisson equation along with momentum are converged at each new time level by a semi-implicit prediction and correction sequence. Convergence is commonly achieved by minimizing the residual (or error) of the discretized pressure-Poisson equation. For steady flows, large time steps are allowed to accelerate convergence to steady-state. The most recent release of this approach is called PISO (Pressure-Implicit with Splitting of Operators) (Issa, 1985). Its roots lie in the SIMPLE (Semi-Implicit Method for Pressure-Linked Equations) algorithm [Patankar and Spalding, 1972). In PISO, the predictor-corrector steps arise from a splitting of operators in the discretized momentum and pressure-Poisson equations. For the steady flow problem, SIMPLE iterates to steady-state convergence while PISO advances in time. Thus, PISO is equally applicable to unsteady and transient flows. However, due to the explicit definitions in the corrector steps, under-relaxation may be necessary in PISO to sustain convergence during the predictor-corrector solution sequence (Wanik and Schnell, 1989).

The third basic approach for predicting unsteady incompressible flows is the "method of pseudo-compressibility" (Chang and Kwak, 1984). This method was introduced by Chorin (1967) for computing steady incompressible flows. Chorin's idea resolved the difficulty of having an explicit definition for the pressure variable in the incompressible flow equations. He proposed to couple the continuity and momentum equations by adding a pressure-like time-dependent term to the continuity equation. This term physically represents the imposition of finite-speed pressure waves onto the incompressible velocity field. The pressure waves are time-advanced (along with momentum) until they theoretically vanish. At convergence the incompressibility constraint is satisfied, but with the pressure field now fully known. For the steady flow problem, it is important to note that the advancement of the velocity and pressure fields to steady-state is accomplished strictly through pseudo time. Consequently, the intermediate solutions are not time accurate. Recently however, the method of pseudo-compressibility was extended to unsteady incompressible flows (see Soh and Goodrich, 1988 for example). The new system of flow equations is essentially the same as the original set except for a second time-dependent velocity term in the momentum equation. While the original time-dependent term represents real time, the second term allows for marching in pseudo time. Thus, pseudo steady-state convergence is achieved for each physical time increment. When using this approach, one should be concerned about the local error tolerance associated with pseudo steady-state convergence relative to the leading temporal truncation error of the physical system.

Presented next is a solution technique for solving the LES governing equations that is based on the original fractional-step method developed by Chorin along with the variations proposed by Kim and Moin (1985) and Rai and Moin (1989). In the current chapter, the numerical accuracy of the solution technique and consistancy of the boundary conditions are verified by simulating an exact solution of the two-dimensional Navier-Stokes equations with continuity. In the applications chapter, this solution technique is tested by predicting the unsteady laminar flow characteristics in a three-dimensional shear driven cavity flow.

2.3.2. Formulation

Chorin's original fractional-step method along with the variations proposed by Kim and Moin (1985) and Rai and Moin (1989) are combined to temporally discretize the LES system of equations (2.3). Kim and Moin time-split the convective and diffusive terms in the momentum equation using an explicit second-order-accurate Adams-Bashforth method and an implicit Crank-Nicolson scheme, respectively. Use of the Crank-Nicolson scheme eliminates the viscous stability restriction which can be severe near the wall even in high-Re wall-bounded flows. As pointed out by Rai and Moin however, the Adams-Bashforth method is unconditionally unstable when applied to the linear convection equation. In their subsequent solution technique, they chose to time-split the convective terms using a third-order-accurate, low-storage, Runge-Kutta procedure. The classification "low-storage" means that information from only the previous time step must be stored in memory. For the linear convection equation, this particular scheme is conditionally stable. Contrasting the numerical stability of the Adams-Bashforth method and Runge-Kutta procedure is formally presented in a section 2.4.

As just described, a Runge-Kutta/Crank-Nicolson solution sequence is adopted here for time-advancement of the LES equations. This sequence involves three complete steps to update the physical velocity and pressure fields and has the form

Intermediate Velocity ($\hat{u}_i^m$):

$$\frac{\hat{u}_i^m - u_i^{m-1}}{\Delta t} = -\alpha^m \left(u_j \frac{\partial u_i}{\partial x_j} \right)^{m-1} - \beta^m \left(u_j \frac{\partial u_i}{\partial x_j} \right)^{m-2} + \gamma^m \frac{\partial}{\partial x_j} \left[\left(\hat{\tau}_{ij}^m + \tau_{ij}^{m-1} \right) + \frac{1}{Re} \frac{\partial \left(\hat{u}_i^m + u_i^{m-1} \right)}{\partial x_j} \right] \qquad (2.4a)$$

Velocity Update $\left(u_i^m\right)$:

$$\frac{u_i^m - \hat{u}_i^m}{\Delta t} = -\frac{\partial \Phi^m}{\partial x_i}, \qquad (2.4b)$$

Pressure Variable $\left(\Phi^m\right)$:

$$\frac{\partial^2 \Phi^m}{\partial x_i \partial x_i} = \frac{1}{\Delta t} \frac{\partial \hat{u}_i^m}{\partial x_i}, \tag{2.4c}$$

Physical Pressure (p):

$$p = \phi + \frac{\Delta t}{2Re} \frac{\partial^2 \phi}{\partial x_i \partial x_i}, \tag{2.4d}$$

where $\alpha^m = \left\langle \frac{8}{15}, \frac{5}{12}, \frac{3}{4} \right\rangle$, $\beta^m = \left\langle 0, -\frac{17}{60}, \frac{5}{12} \right\rangle$, $\gamma^m = \left\langle \frac{4}{15}, \frac{1}{15}, \frac{1}{6} \right\rangle$

and $\Phi^m = \alpha^m \phi^m + \beta^m \phi^{m-1}$.

The parameter m signifies the three steps of the Runge-Kutta procedure. In the intermediate velocity equation for example, the velocities $u_i^{-1} = 0$ (m=-1), $u_i^0 = u_i^n$ (m=0) and $u_i^3 = u_i^{n+1}$ (m=3). The second parameter n denotes the current time level. Thus, $u_i^3 = u_i^{n+1}$ is the updated velocity for the next time level n+1. A pressure variable ϕ replaces the physical pressure p in the velocity update equation due to the implicit treatment of the diffusion term. An exact relationship between ϕ and p is given by the simple expression in (2.4d). Since the intermediate velocity and pressure-Poisson equations are solved independently, it is not necessary to treat the Runge-Kutta coefficients explicitly for updating the physical velocity field u_i. A second scalar variable Φ is therefore introduced of which the physical pressure can be computed anytime during the computation. As in the pressure-based method, a Poisson equation is derived for solution of the pressure variable Φ by taking the divergence of the velocity update equation in (2.4b) and enforcing continuity (2.3b). The result, shown in equation (2.4c), gives the Laplacian of Φ as a function of the divergence of the intermediate velocity field $\hat{u}_i$. The intermediate velocity field does not satisfy incompressibility because the pressure gradient is separated from the momentum equation. Although the Runge-Kutta procedure is third-order accurate in time, the overall solution sequence is second-order time accurate because the diffusive terms are treated with the Crank-Nicolson scheme.

The convective terms in equation (2.4a) are now in a nonconservative form. This form facilitates implementation of high-order spatial accuracy for these terms. Inasmuch as sharp discontinuities are absent from incompressible

flows, the nonconservative form should give results comparable to that of the conservative form (Rai and Moin, 1989). Except for the convective terms, all spatial derivatives shown in the Runge-Kutta/Crank Nicolson solution sequence are discretized by second-order central differences. The convective terms are explicit and are spatially discretized by a third-order-accurate, five-point, upwind-biased stencil. This stencil offers artificial dissipation in the discretization of the convective term as given by the leading fourth-order truncation error. At computational points adjacent to the grid boundaries only three points are available for discretizing the derivatives which are normal to the boundary; one on the boundary itself and two in the field. At these adjacent points, second-order central differences were found to be satisfactory for the convective terms normal to the grid boundary. This overall spatial discretization scheme leads to numerical solutions which are second-order accurate in space.

Implicit treatment of the diffusive term by the Crank-Nicolson scheme creates a sparse 3D coefficeint matrix in the final discretized equation for solution of the intermediate velocity. This equation is solved here by approximate-factorization (A-F). The A-F technique factors the sparse 3D coefficient matrix into a series of three uni-directional solutions (x, y and z directions) that can each be easily handled by a standard tridiagonal solver. The payoff is a substantial reduction in computational effort in terms of real solution time and memory. Solution of the intermediate velocity by the A-F technique has the form (Kim and Moin, 1985)

$$\left(1-A_1\right)\left(1-A_2\right)\left(1-A_3\right)\left(\hat{u}_i^m - u_i^{m-1}\right) = \Delta t\left(-\alpha^m H_j^{m-1} - \beta^m H_j^{m-2} + 2\gamma^m D_j^{m-1}\right) \qquad (2.5)$$

where $A_i = \dfrac{\Delta t\,\gamma^m}{Re}\dfrac{\delta^2}{\delta x_i^2}$, $H_j = u_j\dfrac{\partial u_i}{\partial x_j}$ and $D_j = \dfrac{\partial}{\partial x_j}\left(\tau_{ij} + \dfrac{1}{Re}\dfrac{\partial u_i}{\partial x_j}\right)$

The term $\delta^2 / \delta^2 x_i$ symbolizes the discrete finite difference operator of the total stress term (D_j). The product of the coefficients A_i in equation (2.5) show that approximate-factorization is accurate to $O\left(\Delta t^2\right)$ which is the formal solution accuracy of the overall scheme. Thus, no numerical error is introduced into

the solutions due to the factorization. Solution of intermediate velocity components $\hat{u}_i$ actually proceeds by rearranging equation (2.5) into an alternating direction implicit (ADI) sequence. Because this equation is not coupled explicitly to the pressure-Poisson equation in terms of the scalar Φ^m, it is solved only once for each intermediate velocity component at the outset of each Runge-Kutta step. Thus, the computational efficiency of this fractional-step technique is governed primarily by the CPU time required to solve the pressure-Poisson equation.

2.3.3. Solution of the Pressure-Poisson Equation

The pressure-Poisson equation satisfies the incompressible constraint to within a user-specified error tolerance, and its rapid convergence by an iterative scheme is essential to the overall solution procedure. For this purpose the modified strongly implicit (MSI) scheme, developed by Schneider and Zedan (1981), is implemented in a residual form of the pressure-Poisson equation. The MSI procedure was presented by Schneider and Zedan as a general purpose solver for a linear set of equations defined by a nine-point computational molecule. Its application however reduces easily to five-point molecules by setting the corner points to zero. The computational efficiency of the MSI scheme over point-successive relaxation and alternating directional implicit techniques was demonstrated by Jordan and Spaulding (1993) for 2D grid-generation and by Jordan (1992) for solving the vorticity-stream function equations in 2D steady-state flow problems. Extension of this solver to the 3D pressure-Poisson equation is a straightforward process. It can be viewed as an implicit solver of a planar surface (either x-y, x-z or y-z) that passes through the computational volume in a direction (z, y or x, respectively) which is normal to the surface. The 2D solver sweeps through the volume analogously to the manner an implicit line solver sweeps along a planar surface.

The residual form of the discretized pressure-Poisson equation appears as

$$\left[A_1 + A_2 + A_3\right]\delta^{\ell+1} = -R^{\ell}, \tag{2.6}$$

where the coefficient matrix has components $A_1 = \delta^2 / \delta x_1^2$, the increment $\delta^{\ell+1} = \Phi^{m,\ell-1} - \Phi^{m,\ell}$ and R^{ℓ} is the residual. The parameter ℓ denotes successive updates to the variable Φ^m and m is the particular Runge-Kutta step.

For the pressure-Poisson equation, the residual is defined as

$$R^{\ell} = \frac{\partial^2 \Phi^{m,\ell}}{\partial x_i \partial x_i} - \frac{1}{\Delta t} \frac{\partial \hat{u}_i^m}{\partial x_i}. \tag{2.7}$$

Solution of the increment δ in equation (2.7) by the MSI scheme is a three-step process which constitutes a single iteration ℓ. Each step reflects a single sweep of the solution scheme through the computational volume. The directional order of each sweep is irrelevant to the final solution, although the number of total iterations required for convergence may sometimes be affected. The three-step sequence chosen here is in the order of z,x,y and has the form

$$\left(A_i + A_j\right)\delta^{\ell+1} = -R^{\ell}, \tag{2.8}$$

where i,j are cyclic indices. For quickest convergence, the residual is recomputed after each sweep. The full 3D solution is now dimensionally reduced to three 2D implicit solutions for which the MSI scheme is directly applied. Convergence is monitored by computing the root-mean-square (RMS) of the residual. At convergence $R_{RMS}^{\ell} \cong 0$ meaning that the incompressibility constraint has been satisfied to within the error tolerance specified by the user.

By factoring the coefficient matrix in this way, the MSI scheme can be implemented easily. Inasmuch as this scheme was originally designed as a nine-point implicit solver, it is well-suited to handle a 2D curvilinear form of the pressure-Poisson equation. By conveniently eliminating the appropriate components, it can be applied effectively to the Cartesian coordinate system in equation (2.8). If the pressure-Poisson equation is recast into a residual form first, rather than implementing the MSI scheme directly, the solution methodology gains several distinct advantages. From an accuracy standpoint, the residual which is a necessary computation in the residual form is a justified gauge for monitoring convergence. Also, from a programmer's viewpoint, implementation of the MSI scheme is greatly simplified. This is because the residual term is zero-valued everywhere on the grid boundaries; therefore tracking those boundaries in the computation is not necessary. This latter advantage is particularly important when computing flow in domains having internal boundaries.

2.4. *Computational Molecule*

Establishing proper coupling between the velocity components and the pressure variable is an essential ingredient of the solution strategy to inhibit spurious oscillations. As illustrated in detail by Patankar (1980), fully staggered grids satisfy this demand ideally, but require extrapolation or reflection of the field results for assigning values to the point velocities which lie outside the geometric boundaries. The extrapolation becomes particularly cumbersome for spatial differencing approximations that are higher than second order. In most cases, the spatial accuracy of the outside point velocity is reduced to first-order. As an alternative, one can implement a semi-staggered pattern in which the velocity components are positioned at the grid points and the pressures are located at the grid cell centers. Besides having the velocity field now defined directly on the boundary, this grid also offers the advantage of deriving a consistent set of boundary conditions for the intermediate velocity. Without proper care in the discretization definitions, solution difficulties with this choice will arise because the grid cell pressures can actually become uncoupled from their adjacent neighbors (Maliska and Raithby, 1984). Described below is a computational molecule and solution procedure that exploits the advantages of the semi-staggered grid pattern while maintaining strong coupling between the velocity components and pressure variable. This approach is new and resolves the important issue of pressure-velocity decoupling in semi-staggered grid systems.

The two-dimensional computational molecule in Fig. 2.2 shows the relative positions of the velocity components and the pressure variable on the grid. The velocity components are collocated with the grid points, but the pressure variable is staggered. The source term in the pressure-Poisson equation is computed by averaging the grid cell corner velocities. If the pressure gradient in the velocity update equation is now determined by averaging the pressures at the grid cell centers, then the semi-staggered grid which uncouples the cell pressures from their adjacent neighbors will be recovered. To avert this dilemma, the pressure gradients are computed at the cell interfaces first (as indicated by the arrows in Fig. 2.2) by a fourth-order-accurate compact differencing formula. The pressure gradients needed to update the point velocities are obtained by simply averaging the appropriate values at the adjacent cell interfaces. For example, the u-velocity at point 5 is updated by

averaging the pressure gradients at cell interfaces marked N and S. Likewise, the pressure gradients at the W and E cell interfaces are averaged together to update the corresponding v-velocity. By computing the pressure gradients in this manner, the velocity components and pressure variable remain strongly coupled. Also, no superfluous errors are introduced because the accuracy of the pressure gradients are within the leading truncation error of the overall solution technique.

The procedure for computing the pressure gradients at the cell interfaces will now be explained. After solving the pressure Poisson equation for Φ^m, the pressure gradient is computed by the fourth-order-accurate compact scheme. For example, at the cell interface labeled S in Fig. 2.2,

$$f_{i+1} + 22f_i + f_{i-1} = \frac{24\left(\Phi^m_{i+1/2} - \Phi^m_{i-1/2}\right)}{\Delta x}, \tag{2.9}$$

where $f_i = (\partial\Phi^m / \partial x)_i$. The index i symbolizes the center point at cell interface S and i+1/2 denotes the cell center marked (b). Likewise, at cell interface W

$$g_{j+1} + 22g_j + g_{j-1} = \frac{24\left(\Phi^m_{j+1/2} - \Phi^m_{j-1/2}\right)}{\Delta y}, \tag{2.10}$$

where $g_j = (\partial\Phi^m / \partial y)_j$. The interface center point is denoted by index j and j+1/2 signifies cell center (d). Application of the compact scheme to all cell interfaces in the domain produces an algebraic set of equations which can be solved by a standard tridiagonal solver. The required boundary conditions are determined from the respective velocity update equation (2.4b). For example, application of equation (2.9) at cell interface i = S in Fig. 2.2 requires a boundary definition for f_{i-1}. This definition is supplied by the velocity update equation as

$$\frac{\left(u^m_{i-1} - \hat{u}^m_{i-1}\right)}{\Delta t} = -\left(\frac{\partial\Phi}{\partial x}\right)^m_{i-1} = -f_{i-1}, \tag{2.11}$$

where u^m_{i-1} and $\hat{u}^m_{i-1}$ are the averaged velocity boundary values centered between grid points 1 and 4. The pressure gradient g_{j-1} in equation (2.10) is treated similarly. There

$$\frac{\left(v^m_{j-1} - \hat{v}^m_{j-1}\right)}{\Delta t} = -\left(\frac{\partial \Phi}{\partial y}\right)^m_{j-1} = -g_{j-1}, \tag{2.12}$$

where v^m_{j-1} and $\hat{v}^m_{j-1}$ are the averaged velocity boundary values centered between grid points 1 and 2. One should note that the pressure gradients for updating the w-velocity components are computed in an analogous manner. Finally, the effectiveness of this new procedure for guaranteeing strong velocity pressure coupling in semi-staggered grid patterns is illustrated later in the applications chapter.

2.4. Numerical Stability

Many previous applications of the fractional-step method to unsteady viscous flows temporally discretized the convective term by the Adams-Bashforth method (see Antonopoulos-Domis (1981) and Kim and Moin (1985) for example). This scheme holds the advantages of being second-order-accurate, one-step and low-storage (only information from the previous time step needs to be saved). Unfortunately, a Fourier stability analysis will reveal that the method is unconditionally unstable if applied to the linear convection equation. The linear convection equations has the form

$$\frac{\partial u}{\partial t} + c\frac{\partial u}{\partial x} = 0 \qquad (2.13)$$

As shown in Fig. 2.3, the instability of the Adams-Bashforth method is weak for Courant numbers (σ) less than 0.5; $\sigma = c\Delta t/\Delta x$. If a diffusive term is added to the linear convection equation, then the method becomes stable; which explains why the method has been successful for solving many viscous flow problems. Yet for certain viscous flow problems where at some point the convective terms dominate the physics, very small time steps would be necessary to sustain stable solutions. A typical example would be the outset of an impulsively started flow. This limitation of the Adams-Bashforth method is an unnecessary risk when attempting to develop a useful numerical technique for solving a general class of incompressible flows.

The fractional-step technique developed here should demonstrate strong stability characteristics. As pointed out earlier, a third-order-accurate, three-step, low-storage, Runge-Kutta procedure was chosen to meet this need in lieu of the Adams-Bashforth method. This particular procedure is conditionally stable when applied to the linear convection equation. As shown in Fig. 2.4, if this procedure is combined with the third-order-accurate spatial differences that are used here for the convective terms, the linear convection equation is always stable for Courant numbers $\sigma \leq 1.6$. In the case of the impulsively started viscous flow problem then, reasonable time increments would be permitted early in the simulation. Also, as the relative influence of the viscous term increases with time, the stability limit $\sigma = 1.6$ will relax even further.

2.7. Solution Accuracy Verification

The temporal and spatial accuracy of the overall solution procedure as well as the consistency of the intermediate velocity boundary conditions was verified by simulating an exact solution of the 2D unsteady Navier-Stokes equations. Through reduction of the mesh spacing under a constant CFL value, the numerical results displayed second-order improvement as given by the leading truncation error of the overall solution technique. The exact solution of the 2D unsteady Navier-Stokes equations that was simulated by the fractional-step technique has the form (Chorin, 1967)

$$u(x,y,t) = -\cos(x)\sin(y)e^{-2t} \tag{2.14a}$$

$$v(x,y,t) = \sin(x)\cos(y)e^{-2t} \tag{2.14b}$$

$$p(x,y,t) = -\tfrac{1}{4}[\cos(2x) + \cos(2y)]e^{-4t} \tag{2.14c}$$

These equations portray the decay of periodic vortices. The simulation was initialized by the exact solution for time t = 0.0. The spatial domain was defined as $0 \leq x,y \leq \pi$. Using an exact set of boundary conditions for the physical velocity with the definition in equation (2.14) for the intermediate velocity, the initial flow field was advanced to the same physical time for each grid tested. This physical time was t = 0.35 seconds which corresponds to a reduction of the maximum boundary velocity to one-half of its initial value. The simulation results are plotted in Fig. 2.5 where the grid factor is the ratio of the grid spacing in the reference grid (11 x 11 uniform) to the refined grid. The exact error in the figure is the absolute maximum difference between the numerical predictions and the exact solution normalized by the maximum value in the domain. Fig. 2.5 clearly shows a linear reduction of the velocity and pressure errors by refining the grid. These reductions indeed signify a solution technique that is second-order accurate. Thus, the numerical accuracy of this fractional-step technique was verified through this 2D simulation.

CHAPTER THREE
LES IN CURVILINEAR COORDINATES

3.1. Introduction

Once again, the LES methodology resolves (or computes) the energy dominate scales of turbulence while modeling the remaining finer subgrid scale levels. To extend this strategy to arbitrary configurations, the Navier-Stokes equations must first be transformed to a curvilinear coordinate system. As in the Cartesian system, the resultant formulation is then filtered to acquire the governing set of LES equations pertinent to complex geometries. Under the curvilinear coordinate framework, the LES equations can not be solved by traditional spectral methods. A high-order-accurate discretization technique must be developed in the form of either a finite difference, finite volume or finite element method.

A crucial condition on this new LES development is the ultimate possession of a solution technique that displays strong convergence properties and insures proper coupling between all variables in cuvilinear space; especially between pressure and velocity. Usually, one chooses either the physical or contravariant form of the velocity components consistantly throughout the transformation (see Patankar (1980) and Rubin and Reddy (1988) for example). Herein however, the velocity variables are mixed to facilitate implementation of the same solution algorithms that were developed for the Cartesian system. By simply reformulating the pressure-Poisson and physical velocity update equations to contravariant form, the same computational molecule previously described for the Cartesian coordinate system and the fast MSI elliptic solver are directly applicable. Since it is well-known that pressure convergence consumes most of the computational effort in the solution of incompressible flows, this particular approach tends to minimize the CPU requirement.

3.2. Transformed LES Equations

Transformation of the Navier-Stokes equations (2.2) to curvilinear coordinates where the physical velocity components are the primary dependent variable can have the form

Momentum:

$$\frac{\partial\sqrt{g}u_i}{\partial t}+\frac{\partial u_i U^k}{\partial\xi^k}=\frac{\partial\sqrt{g}\,\xi^k_{x_i}\,p}{\partial\xi^k}+\frac{1}{Re}\frac{\partial}{\partial\xi^k}\left[\sqrt{g}\,g^{k\ell}\frac{\partial u_i}{\partial\xi^\ell}\right] \tag{3.1a}$$

Continuity:

$$\frac{\partial\sqrt{g}\;\xi^k_{x_i}\,u_i}{\partial\xi^k}=0 \tag{3.1b}$$

where the contravariant velocity components U^k are defined as $U^k=\sqrt{g}\,\xi^k_{x_j}\,u_j$. The Jacobian $\sqrt{g}$ of the transformation appears in the formulation to place it in strong conservation-law form (Anderson et al., 1984). Expressions for the transformation coefficients $\xi^k_{x_j}$, the contravariant metric coefficients $g^{k\ell}$ and the Jacobian are given in Anderson et al. (1984). To derive the corresponding LES equations, these transformed equations must be filtered the same way as before except now in curvilinear space. Each term is filtered according to

$$\overline{\Phi}(\xi^k)=\int\Phi(\hat{\xi}^k)H(\xi^k,\hat{\xi}^k)d\hat{\xi}^k \tag{3.2}$$

where $H\left(\xi^k,\hat{\xi}^k\right)$ is the filter function in the curvilinear space. This filter function can take on mathematical forms similar to the Gaussian, sharp cut-off and box filters shown earlier for Cartesian coordinate systems. Since the partial differentiation and filtering commute in the cuvilinear space, only the non-linear term introduces additional terms into the filtered equations in form of a transformed Reynolds stress. Accordingly, the governing set of LES equations in curvilinear space are

Momentum:

$$\frac{\partial\sqrt{g}\,\overline{u}_i}{\partial t}+\frac{\partial\overline{u}_i\overline{U}^k}{\partial\xi^k}=\frac{\partial\sqrt{g}\,\xi^k_{x_i}\,\overline{p}}{\partial\xi^k}+\frac{\partial\sigma^k_i}{\partial\xi^k}+\frac{1}{Re}\frac{\partial}{\partial\xi^k}\left[\sqrt{g}\,g^{k\ell}\frac{\partial\overline{u}_i}{\partial\xi^\ell}\right] \tag{3.3a}$$

Continuity:

$$\frac{\partial\overline{U}^k}{\partial\xi^k}=0 \tag{3.3b}$$

where the subgrid scale stress tensor $\sigma_i^k = \overline{u_i}\,\overline{U}^k - \overline{u_i U^k}$. The contravariant velocity is now the dependent variable in the transformed continuity equation. The relationship between the tensor σ_i^k and its Cartesian counterpart τ_{ij} is shown by the following. The SGS stress tensor in terms of only the Cartesian velocity components appears as

$$\sigma_i^k = \overline{u_i}\,\overline{\sqrt{g}\,\xi^k_{x_j} u_j} - \overline{u_i \sqrt{g}\,\xi^k_{x_j} u_j} \tag{3.4}$$

By removing the metrics from the filtering process, the definition for σ_i^k becomes

$$\sigma_i^k = \sqrt{g}\,\xi^k_{x_j}\left(\overline{u_i}\,\overline{u_j} - \overline{u_i u_j}\right) \tag{3.5}$$

which can be redefined in terms of τ_{ij} as $\sigma_i^k = \sqrt{g}\,\xi^k_{x_j}\tau_{ij}$. This last expression will be used later to derive a SGS turbulence model in curvilinear coordinates. One must remember however, that by extracting the metrics from the filtering process, the expression is a simplification of the subgrid stress definition specifically for the model development.

Application of the fractional-step solution technique previously described (with the Runge-Kutta/Crank-Nicolson sequence) to the curvilinear form in equation (3.3) appears as

Intermediate Velocity (u_i):

$$\frac{\sqrt{g}\left(\hat{u}_i - u_i^{m-1}\right)}{\Delta t} = -\alpha^m\left(U^k \frac{\partial u_i}{\partial \xi^k}\right)^{m-1} - \beta^m\left(U^k \frac{\partial u_i}{\partial \xi^k}\right)^{m-2} + \gamma^m \frac{\partial}{\partial \xi^k}\left[\left(\sigma_i^k\Big|^m + \sigma_i^k\Big|^{m-1}\right) + \frac{1}{Re}\sqrt{g}\,g^{k\ell}\frac{\partial\left(\hat{u}_i^m + u_i^{m-1}\right)}{\partial \xi^\ell}\right] \tag{3.6a}$$

Contravariant Velocity Update (U_i):

$$\frac{\left(U^k\right)^m - \left(\hat{U}^k\right)^{m-1}}{\Delta t} = -\sqrt{g}\,g^{kl}\frac{\partial \Phi^m}{\partial \xi^l} \tag{3.6b}$$

Pressure Variable (Φ):

$$\frac{\partial}{\partial \xi^k}\left[\sqrt{g}\, g^{k\ell}\frac{\partial \Phi}{\partial \xi^\ell}\right]=\frac{1}{\Delta t}\frac{\partial \hat{U}^k}{\partial \xi^k} \tag{3.6c}$$

The pressure-Poisson equation (3.6c) was derived by taking the divergence of the velocity update equation (3.6b) and enforcing continuity (3.3b) all in the computational space. Notice that by reformulating of the velocity update and pressure-Poisson equations with the contravariant velocity components instead of the physical components, the resultant form of the governing equations is identical to the original Cartesian system except for the introduction of the metric coefficients and Jacobian. These new metric terms are easily handled by the computational molecule and discretization strategy described earlier. They are located at the grid points and averaged exactly the same way as the velocity components. In this form, no new solution schemes for the intermediate velocity and pressure variable are necessary to attain LES results in the computational domain. Due to the non-orthogonal components in the pressure-Poisson equation, the MSI elliptic solver now has contributions from all nine points.

A mandatory requirement of the above formulation is satisfaction of the conservative property by the pressure solution in curvilinear space. This condition can be quickly checked by appling the divergence theorm to the discretized pressure-Poisson equation in terms of the contravariant intermediate velocities $\hat{U}^k$. In the curvilinear space, the divergence theorm can be defined as

$$\iiint_{\Omega} \nabla \bullet \hat{U}\, d\Omega - \iint_{\Lambda} \hat{U} \bullet n\, d\Lambda = 0 \tag{3.7}$$

where (Ω, Λ) symbolize the curvilinear space volume and boundary surface, respectively. The del and normal operators are implemented in the computational domain. By examing the computational molecule shown in Fig. 4, one can see that the volume integral is satisfied by summing the discretized field representation of the Laplacian in the pressure-Poisson equation. This is done by substituting the Laplacian of the pressure variable for the divergence of $\hat{U}^k$. The cell volume fluxes of pressure (designated by the arrows at the cell surfaces) will sum to zero in the field volume if the boundary contributions are

ignored. If the cells adjacent to the wall boundary are included, a volume summation nets velocity and pressure gradient flux across the boundary. For example, at cell (a) in Fig. 4, a velocity and pressure flux remain between boundary points (4) and (1) and between (2) and (1). These fluxes are

$$\left[\sqrt{g}\, g^{11}\frac{\partial \Phi}{\partial \xi} + \sqrt{g}\, g^{12}\frac{\partial \Phi}{\partial \eta}\right]_E + \left[\sqrt{g}\, g^{21}\frac{\partial \Phi}{\partial \eta} + \sqrt{g}\, g^{22}\frac{\partial \Phi}{\partial \xi}\right]_S + \hat{U}^E + \hat{V}^S = 0 \qquad (3.8)$$

Cancellation of these fluxes is acheived by simply treating the contravariant velocity update equation (3.6b) as a normal condition on the boundary. Thus, the divergence theorm in the computational domain is satisfied by the discretized pressure-Poisson equation with the contravariant velocity equation used as a normal boundary flux. This proof verifies conservation which guarantees incompressibility at each time step.

CHAPTER FOUR

DISCUSSION OF BOUNDARY CONDITIONS

4.1. Intermediate Velocity

The impetus for collocating the velocity components with the grid points is to facilitate derivation of a consistent set of boundary conditions for the intermediate velocity components along no-slip walls. For the semi-staggered grid, deriving such boundary conditions begins by projecting equation (2.4a) onto the wall. The result is

$$\hat{u}_i^m - u_i^{m-1} = \Delta t\,\gamma^m \frac{\partial}{\partial x_j}\left[\left(\hat{\tau}_{ij}^m + \tau_{ij}^{m-1}\right) + \frac{1}{Re}\frac{\partial\left(\hat{u}_i^m + u_i^{m-1}\right)}{\partial x_j}\right] \tag{4.1}$$

which is implicit in $\hat{u}_i^m$. Devising an implicit solution scheme to accommodate this equation is not an easy task. To simplify matters, a similar explicit expression can be derived which is still second-order accurate in time. First, we note that $\nabla\Phi^m = \nabla\Phi^{m-1} + O(\Delta t)$. We then modify the velocity update equation (2.4b) to approximate the components of $\hat{u}_i^m$ in terms of $\hat{u}_i^{m-1}$;

$$u_i^m - \hat{u}_i^m = -\Delta t\nabla\Phi^{m-1} - O(\Delta t)^2 = u_i^{m-1} - \hat{u}_i^{m-1} - O(\Delta t)^2 \tag{4.2}$$

Since $u_i^m = u_i^{m-1}$ along the wall and $u_i^m = u_i^{m-1} + O(\Delta t)$ in the field, equation (4.2) shows that $\hat{u}_i^m = \hat{u}_i^{m-1} + O(\Delta t)^n$ where n = 1 at the field points and n = 2 along the wall boundary. By substituting this result into equation (4.1), the definition for the intermediate velocity at no-slip walls becomes explicit and has the form

$$\hat{u}_i^m - u_i^{m-1} = \Delta t\,\gamma^m \frac{\partial}{\partial x_j}\left[\left(\hat{\tau}_{ij}^{m-1} + \tau_{ij}^{m-1}\right) + \frac{1}{Re}\frac{\partial\left(\hat{u}_i^{m-1} + u_i^{m-1}\right)}{\partial x_j}\right] \tag{4.3}$$

In this expression, terms tangent to the wall are accurate to $O(\Delta t)^3$ while those normal to the wall boundary are accurate to $O(\Delta t)^2$. The overall accuracy of this expression is therefore $O(\Delta t)^2$ which is consistant with the field solution. To maintain the same spatial accuracy at the boundary points as in the field,

the tangential and normal terms are approximated by standard second-order-accurate central and one-sided differences, respectively.

A consistant set of wall boundary conditions must also be derived for the intermediate velocity in the curvilinear coordinate framework. Equation (4.3) in curvilinear coordinates appears as

$$\hat{u}_i^m - u_i^{m-1} = \Delta t\, \gamma^m \frac{\partial}{\partial \xi^k}\left[\left(\hat{\tau}_{ik}^{m-1} + \tau_{ik}^{m-1}\right) + \frac{1}{Re}\sqrt{g}\, g^{k\ell}\frac{\partial\left(\hat{u}_i^{m-1} + u_i^{m-1}\right)}{\partial \xi^\ell}\right] \tag{4.4}$$

where the quantities in the bracket, according to a finite volume discretization, are the flux vectors defined at the half points. Terms coincident with the wall are evaluated as usual using two flux vectors (or three boundary points). But to maintain second-order accuracy in the spatial differencing of the terms normal to the wall, four points or three flux vectors are necessary. Labeling the wall boundary point as the zero point, second-order accuarcy for these terms requires that

$$\Delta\left(f_i'\right)_0' = a f_i'\big|_{1/2} + b f_i'\big|_{3/2} + c f_i'\big|_{5/2} \tag{4.5}$$

where Δ is the grid point spacing and the constants a, b and c are to be determined. In the computational space, $\Delta = 1$. The flux vector f_j' is defined as

$$f_i'\big|_j = \left(\hat{\tau}_{ik}^{m-1} + \tau_{ik}^{m-1}\right)\Big|_j + \frac{1}{Re}\sqrt{g}\, g^{k\ell}\frac{\partial\left(\hat{u}_i^{m-1} + u_i^{m-1}\right)}{\partial \xi^\ell}\Bigg|_j \tag{4.6}$$

where, in terms of the grid points, the SGS stress terms are evaluated

$$\left(\tau_{ij}\right)_j = 1/2\left[\left(\tau_{ij}\right)_{j+1/2} + \left(\tau_{ij}\right)_{j-1/2}\right] \tag{4.7}$$

and the first-order velocity terms are

$$\frac{\partial u_i}{\partial \xi^\ell}\Bigg|_j = \left(u_i\right)_{j+1/2} - \left(u_i\right)_{j-1/2} \tag{4.8}$$

After expanding each component in equation (4.5) according to a Taylor series and enforcing second-order accuracy, the coefficients are a = -2, b = 3 and c = -1. Thus, the projection of equation (4.4) onto a no-slip curvilinear wall gives

$$\left(\hat{u}_o^m - u_o^{m-1}\right)_w = \frac{\Delta t\,\gamma^m}{\sqrt{g}\,Re}\left[-2f'_{1/2} + 3f'_{3/2} - f'_{5/2}\right] \tag{4.7}$$

which is again second-order accurate in space. The consistancy of this wall expression against standard finite differences can be quickly checked by applying it to the Cartesian coordinate definition in equation (4.3) without the SGS stress terms. The u-component becomes

$$\left(\hat{u}_o^m - u_o^{m-1}\right)_w = \frac{\Delta t\,\gamma^m}{Re(\Delta x)^2}\left[-2(f_1 - f_0) + 3(f_2 - f_1) - (f_3 - f_2)\right] \tag{4.8}$$

where $f_i = \hat{u}_i^{m-1} + u_i^{m-1}$. After simplfying

$$\left(\hat{u}_o^m - u_o^{m-1}\right)_w = \frac{\Delta t\,\gamma^m}{Re(\Delta x)^2}\left[2f_0 - 5f_1 - 4f_2 - f_3\right] \tag{4.9}$$

which is standard second-order-accurate, one-sided differencing of a diffusive term normal to the wall.

4.2. <u>Pressure</u>

As noted earlier, two important concerns are satisfied by staggering the pressure variable in the computational molecule. The pressure field is staggered from the velocity field to eliminate spurious oscillations in the flow solutions (Patankar, 1980). Due to the staggered grid arrangement, specification of a grid boundary condition for the pressure variable is not required. The corresponding velocity component is used instead of the normal pressure gradient at all grid cell boundaries that are geometrically coincident with the cavity walls. Since the shear-driven cavity is fully enclosed, no boundary condition is therefore needed for the pressure variable to solve the discretized pressure-Poisson equation. Besides inhibiting spurious oscillations in the numerical solutions, no numerical definition is necessary for the pressure variable at wall boundaries. This can be illustrated effectively by the following simple example. The residual for the one-dimensional form of the discretized pressure-Poisson equation at the center cell point i = a in Fig. 1 is

$$R^{\ell} = \left(\Phi_{i+1} - 2\Phi_i + \Phi_{i-1}\right)^{m,\ell} - \frac{\Delta x}{2\Delta t}\left[\left(\hat{u}_5 + \hat{u}_2\right) - \left(\hat{u}_4 + \hat{u}_1\right)\right]^m \tag{4.10}$$

The u-velocity update equation applied at the no-slip wall $\left(u_1^n = 0\right)$ to the left of grid cell (a) becomes

$$\frac{\Delta x}{2\Delta t}\left(\hat{u}_4 + \hat{u}_1\right)^m = \left(\Phi_i + \Phi_{i-1}\right)^{m,\ell} \tag{4.11}$$

Substitution of this equation into equation (4.10) in terms of $\left(\hat{u}_4 + \hat{u}_1\right)$ reveals that the evaluation of the residual closest to the wall boundary does not require a definition for the pressure variable at the wall (or outside the wall) in terms of the field values. As a consequence, the pressure field remains conservative and second-order accurate, and the rate of convergence significantly improves because the boundary definition commonly appears as a Neuman type condition. Extension of this example to three-dimensions will yield the same result.

CHAPTER FIVE
SUBGRID SCALE TURBULENCE MODELS

5.1. Introduction

Since inception of the large-eddy simulation (LES) for numerical solution of turbulent flows, substantial effort has been devoted to developing a ubiquitous turbulence model. While the numerics of the computation resolve the larger energy-bearing eddies of the turbulent field, the model must properly dissipate turbulent energy at the subgrid scale (SGS) level. By far the most tested SGS turbulence model is Smagorinsky's eddy viscosity model (Smagorinsky, 1963). Smagorinsky assumed that the turbulence at the fine scale level was strictly dissipative, homogeneous and in equilibrium (production equals dissipation). Consequently, his algebraic model carries an empirical coefficient which must reflect the global dissipative nature of the fine-scale turbulent field. Smagorinsky's coefficient is actually embedded in the length scale definition for the subgrid scale eddies. In isotropic turbulent flows, defining the length scale is unambiguous. But for anisotropic turbulence, the length scale cannot be expressed uniquely. For example, turbulent boundary layer flows require a length scale whose coefficient is approximately equal to one-half of that acceptable for free-shear layers. Furthermore, the length scale itself must be appropriately damped to satisfy the asymptotic behavior of the turbulent shear stress at points near the wall boundaries. Up until recently, simple algebraic expressions were commonly used to accommodate that behavior. Some expressions included a van Driest type function which utilized several constants to dampen the length scale. One was saddled with selecting an appropriate expression from the literature, or conversely, developing a separate length scale definition that was specific to the problem at hand.

Mathematically, demarcation between the resolved and unresolved (or modeled) turbulent scales results from spatially filtering the Navier-Stokes (N-S) equations. This spatial filter is commonly referred to as the grid filter. Those scales removed by the filter operation must be properly represented by the turbulence model while the computed turbulence is that which is resolved explicitly by the physical grid. By filtering the N-S equations a second time (by

a test filter), an intermediate field arises that lies within the finest scales of the resolved turbulence. Exploitation of this intermediate field to provide local values for Smagorinsky's coefficient is the premise behind the dynamic model conceived by Germano, Piomelli, Moin and Cabot (1991); hereinafter labeled as GPMC. This new model responds dynamically to the computed flow physics. It can display the correct asymptotic behavior near solid walls and produce minimal contributions within laminar flow regions. The dynamic model is also capable of representing backscatter (or negative dissipation). Backscatter appearances in a turbulent flow reflect local reversal of energy flow up the cascade from the fine scales to the larger ones. After replacing a van Driest damped SGS model with their dynamic model in both a transitional and a fully developed turbulent channel flow, GPMC indeed produced better comparisons to the corresponding DNS results Also, by interrogating DNS results of a turbulent channel flow, Piomelli et al (1991) revealed backscatter phenomena throughout the channel. Backscatter characteristics have been reported in other turbulent flows as well (Hartel and Kleiser, 1993 for example). Thus, intermittent backscatter effects would be an essential ingredient toward achieving a ubiquitous SGS turbulence model.

Unfortunately, the algebraic expression for Smagorinsky's coefficient as proposed by GPMC can be locally indeterminate; in particular, the denominator of the expression can approach zero. To circumvent this ill-conditioned problem in their turbulent channel flow simulation, they ensemble-averaged the resolved field over grid planes parallel to the channel walls. The spatial dependence of the model coefficient was therefore reduced to only the normal direction. Lilly (1992) modified the dynamic model by deriving a well-posed algebraic expression for Smagorinsky's coefficient using a least-squares approach. His expression will yield coefficients which are both temporally and spatially dependent and will recognize backscatter by permitting negative values. However, use of Lilly's expression in the purest sense may lead to numerical instabilities. The solutions may eventually diverge because the total viscosity (turbulent eddy viscosity plus the kinematic viscosity) can sustain negative values over long time periods. Commonly, *ad hoc* measures are employed to alleviate this problem; such as filtering the coefficient or assuming homogeneous flow directions. As examples, Squires (1993) assumed global

homogeneity in a rotating turbulent flow which resulted in a model coefficient that was only time dependent. And in a turbulent cavity flow simulation by Zang et al. (1993), a zero total viscosity cut-off was necessary even after locally averaging the model coefficient. Realizing the shortcomings of Lilly's expression for general applications, Akselvoll and Moin (1993) tested a more complex dynamic localization model (Ghosal et al., 1992) in their LES computations of a turbulent flow over a backward facing step. Since backscatter phenomena is excluded from the dynamic localization model (by constraining the model coefficient to only positive values), *ad hoc* measures are not necessary to maintain convergence. Comparisons between the numerical results using the dynamic localization model and those of the modified dynamic model (with spanwise ensemble averaging and zero total viscosity cut-off) showed only minor differences. For practical problems then, the dynamic localization model seems more attractive. But in the backward facing step test case, it required two times more CPU overhead (40 percent) than the modified dynamic model did.

5.2. *Smagorinsky Model*

5.2.1. Damped

For all the LES computations presented here, Smagorinsky's eddy viscosity model was implemented to represent the subgrid scale turbulence. In Cartesian tensor notation, this model has the form (Smagorinsky, 1963):

$$\tau_{ij} - 1/3\,\delta_{ij}\tau_{kk} = 2\,\nu_T \overline{S}_{ij} \tag{5.1a}$$

$$\overline{S}_{ij} = \frac{1}{2}\left(\frac{\partial u_i}{\partial x_j} + \frac{\partial u_j}{\partial x_i}\right) \tag{5.1b}$$

$$\nu_T = \ell^2 \sqrt{2\overline{S}_{ij}\overline{S}_{ij}} \tag{5.1c}$$

$$\ell = C_s \overline{\Delta} \tag{5.1d}$$

In this model, ℓ is the turbulence characteristic length scale, C_S is the global dissipation coefficient and $\overline{\Delta}$ is the grid filter width. As a minimum $\overline{\Delta} = 2h$, where h is the grid point spacing. The overbar symbolizes first level filtering of the turbulent quantities. Removal of the trace in the SGS stress tensor τ_{ij} is necessary because the flows under consideration here are incompressible. To

partially account for anisotropic turbulence through refinement of the grid spacing, Deardorff (1970) defined the filter width as $\bar{\Delta} = \left(\bar{\Delta}_1 \bar{\Delta}_2 \bar{\Delta}_3\right)^{1/3}$. The subscripts 1, 2 and 3 depict the filter width in the x, y and z directions, respectively.

In the damped form of Smagorinsky's model, the length scale is modified by a van Driest damping function to account for the effects of solid wall boundaries (van Driest, 1956). The length scale now becomes

$$\ell = C_s\left[1 - \exp\left(-y^+ / A^+\right)^m\right]^n \left(\bar{\Delta}_1 \bar{\Delta}_2 \bar{\Delta}_3\right)^{1/3} \qquad (5.2)$$

The wall length unit y^+ is the minimum field value of $y\sqrt{\tau_w/\rho}/\nu$, where τ_w is the magnitude of the wall shear stress. The constant A^+ has the value 26. An historical summary of the various values assigned to the exponents m and n in the van Driest damping function was reported by Piomelli et al. (1988).

Presented in the next chapter is the application of the damped model for representing the SGS field of a turbulent flow in an enclosed shear-driven cavity. The need to damp the length scale in Smagorinsky's model became apparent after applying the undamped version, shown in equation (5.1d), to the cavity flow problem. The undamped model repeatedly predicted high levels of turbulent eddy viscosity near the cavity walls which is contrary to the reported experimental observations of Koseff and Street (1984a). By damping the length scale according to the form in equation (5.2), the turbulent eddy viscosity near the cavity walls was reduced and agreed qualitatively with the experimental evidence.

The damped model however has several major drawbacks. First, since Smagorinsky's coefficient in the model is a constant and always positive, backscatter of turbulent energy from the subgrid scales to the resolved scales cannot occur. Secondly, this model will show significant turbulent levels in pockets or regions that are primarily deterministic. There is no intrinsic mechanism for minimizing the SGS turbulent stress levels in flow regions which are transitional or laminar. Finally, the damping function for the length scale cannot be genuinely sensitive to the true asymptotic behavior of the shear stress near no-slip walls. In the SGS model presented next, these drawbacks

are alleviated because Smagorinsky's coefficient is mathematically coupled to the physical dynamics of the resolved turbulent field.

5.2.2. Dynamic

To facilitate discussion of the dynamic model, Smagorinsky's relationship is repeated, but now in a more compact form than shown above. Again in Cartesian tensor notation, the SGS stress tensor τ_{ij} is modeled as

$$\tau_{ij} - 1/3\delta_{ij}\tau_{kk} = 2C\overline{\Delta}^2|\overline{S}|\overline{S}_{ij} \tag{5.3a}$$

$$|\overline{S}| = \sqrt{2\overline{S}_{ij}\overline{S}_{ij}} \tag{5.3b}$$

In this particular form the turbulent eddy viscosity ν_T is characterized by a local Smagorinsky coefficient C, the grid filter width $\overline{\Delta}$ and the magnitude $|\overline{S}|$ of the resolved strain-rate tensor $\overline{S}_{ij}$; i.e. $\nu_T = C\overline{\Delta}^2|\overline{S}|$. According to the derivation by GPMC, an expression for C is achieved by first filtering the LES system in equation (2.3) by a test filter. A new stress term $T_{ij} = \overline{\overline{u}_i\overline{u}_j} - \overline{\overline{u_i u_j}}$ arises as well as a Leonard-type term $L_{ij} = \overline{\overline{u}_i\overline{u}_j} - \overline{\overline{u}_i}\,\overline{\overline{u}_j}$. The second overbar in both definitions symbolize the test filter operation. By equating these two definitions in terms of $\overline{\overline{u}_i\overline{u}_j}$, Germano (1992) established an identity defined as $L_{ij} = T_{ij} - \overline{\tau}_{ij}$. The tensor L_{ij} is calculated directly from the resolved field. Furthermore, Smagorinsky's eddy viscosity scaling law is assumed valid for representing the new stress tensor T_{ij}. The model for T_{ij} appears as

$$T_{ij} - 1/3\delta_{ij}T_{kk} = 2\overline{\overline{\Delta}}^2|\overline{\overline{S}}|\overline{\overline{S}}_{ij} \tag{5.4}$$

From Germano's identity, the resolvable field L_{ij} has the form

$$L_{ij} - 1/3\delta_{ij}L_{kk} = 2C\overline{\Delta}^2 M_{ij} \tag{5.5a}$$

$$M_{ij} = \alpha^2|\overline{\overline{S}}|\overline{\overline{S}}_{ij} - \overline{|\overline{S}|\overline{S}_{ij}} \tag{5.5b}$$

where the filter ratio $\alpha = \overline{\overline{\Delta}}/\overline{\Delta}$. At this point, Lilly (1992) performed a least squares minimization to derive an algebraic expression for C that is dynamically computed from the finest scales of the resolvable turbulent field. This expression is

$$C = -\frac{L_{ij}M_{ij}}{2\overline{\Delta}^2 M_{ij}M_{ij}} \tag{5.6}$$

Inasmuch as the grid filter width $\overline{\Delta}$ is set equal to the local grid point spacing, the only input parameter is the filter ratio α. Through numerical experiments, GPMC showed that $\alpha = 2$ is an optimum choice.

Applications demonstrating the superiority of the dynamic model over the damped model have been reported by GPMC and Zang and Piomelli (1990). In this dissertation, it will also be shown that dynamic model produced better comparisons to the experimental data than the damped model did in a LES computation of a turbulent flow in a shear-driven cavity.

5.3. Generalized Dynamic Model

To generalize the dynamic model for applications in complex geometries, the model must first be mathematically transformed to the computational domain. It should be emphasized that modeling the SGS turbulent field in the computational domain is new work in the LES research arena. The procedure for deriving the generalized model is identical to that of GPMC except for the fact that the SGS stress tensor components are now products of the physical and contravariant velocity components. This new form of the stress tensor must be maintained throughout the derivation to arrive at an equivalent expression for the model coefficient as shown in equation (5.6). Finally, the grid and test filter operations exercised earlier in Cartesian coordinates is certainly valid for the computational space. Except now, the filters are defined in curvilinear coordinates with their spatial widths equal to unity.

As shown earlier in chapter 3, the grid filter operation for deriving the LES equations in curvilinear coordinates produced a transformed SGS turbulent stress tensor defined as $\sigma_i^k = \overline{u}_i \overline{U}^k - \overline{u_i U^k}$ where $\overline{U}^k$ signifies the filtered contravariant velocity components; $\overline{U}^k = \sqrt{g}\, \xi^k_{x_j}\, \overline{u}_j$. Also, σ_i^k in terms of its Cartesian counterpart τ_{ij} is $\sigma_i^k = \sqrt{g}\, \xi^k_{x_j}\, \tau_{ij}$. Using this last expression, a generalized dynamic model (GDM) for the SGS stress tensor can be defined as

$$\sigma_i^k - 1/3\, \zeta_i^k \tau_{\ell\ell} = 2C\overline{\Delta}^2 |\overline{S}| \overline{S}_i^k \qquad (5.7)$$

where C is Smagorinsky's constant. The turbulent eddy viscosity is defined as $\nu_T = C\overline{\Delta}^2 |\overline{S}|$ where $|\overline{S}| = \sqrt{2\, \overline{S}_{ij}\, \overline{S}_{ij}}$. The strain-rate tensor $\overline{s}_{ij}$ is computed in the computational space according to

$$\overline{S}_{ij} = \frac{1}{2}\left(\frac{\partial \overline{u}_i}{\partial x_j} + \frac{\partial \overline{u}_j}{\partial x_i}\right) = \frac{1}{2}\left(\xi^k_{x_j}\frac{\partial \overline{u}_i}{\partial \xi^k} + \xi^k_{x_i}\frac{\partial \overline{u}_j}{\partial \xi^k}\right) \tag{5.8}$$

Finally, the term ς_i^k is defined as $\varsigma_i^k = \xi^k_{x_j}\delta_{ij} = \xi^k_{x_i}$.

Like the SGS stress tensor σ_i^k, the resolvable strain-rate field $\overline{S}_i^k$ in the computational space is $\overline{S}_i^k = \sqrt{g}\,\xi^k_{x_j}\,\overline{S}_{ij}$. Combining this transformation with equation (5.8) gives the complete definition of $\overline{S}_i^k$ in terms of the Cartesian velocity components. This definition is

$$\overline{S}_i^k = \frac{\sqrt{g}}{2}\left(\xi^k_{x_j}\xi^\ell_{x_j}\frac{\partial \overline{u}_i}{\partial \xi^\ell} + \xi^k_{x_j}\xi^\ell_{x_i}\frac{\partial \overline{u}_j}{\partial \xi^\ell}\right) \tag{5.9}$$

With the contravariant metric tensor $g^{k\ell}$ defined as $g^{k\ell} = \xi^k_{x_j}\xi^\ell_{x_j}$, the resolvable strain-rate tensor in the computational space can be reformulated in terms of the physical and contravariant velocity components as

$$\overline{S}_i^k = \frac{1}{2}\left(\sqrt{g}g^{k\ell}\frac{\partial \overline{u}_i}{\partial \xi^\ell} + \overline{U}_f^k\right) \tag{5.10a}$$

$$\overline{U}_f^k = \xi^k_{x_j}\,\overline{u}_j^f \tag{5.10b}$$

$$\overline{u}_j^f = \frac{\partial \sqrt{g}\xi^\ell_{x_i}\,\overline{u}_j}{\partial \xi^\ell} \tag{5.10c}$$

One can now easily see that the first term in this definition is the direct contribution of the generalized SGS turbulence model to the transformed diffusion term in equation (3.1a). The second term represents the contravariant components of the transformed cell flux vectors (u_j^f).

The procedures of Germano et al. (1991) and Lilly (1992) were used to derive an expression for Smagorinsky's coefficient in the GDM. To implement their procedures directly however, the SGS stress tensor σ_i^k was kept as a product of the Cartesian and contravariant velocity components. In this case, the metrics remain as part of the filtering process. It should be noted at this point, that both the grid and test filter operations in the computational space have spatial widths equal to unity. To acquire an expression for Smagorinsky's coefficient in the computational space, the governing LES equations in curvilinear coordinates were filtered a second time (by the test filter). Test filtering these equations produced terms similar to those obtained by Germano

et al. (1991) in the Cartesian coordinate system. In the computational space however, a new resolvable Reynolds stress tensor arises as well as a Leonard tensor. These tensors are:
Reynolds stress tensor $\mathcal{T}_i^k$:

$$\mathcal{T}_i^k = \overline{\overline{u}_l \overline{U^k}} - \overline{\overline{u_l U^k}} \tag{5.11}$$

Leonard tensor $\mathcal{L}_i^k$:

$$\mathcal{L}_i^k = \overline{\overline{u}_l \overline{U^k}} - \overline{\overline{u}_l \overline{U^k}} \tag{5.12}$$

where the second overbar indicates test filtering. The tensor $\mathcal{L}_i^k$ is resolvable, and is computed by test filtering the Cartesian and contravariant velocity components of the resolved field. The identity derived by Germano (1992) for the Leonard term in Cartesian coordinates has a similar form in the computational space, but now the identity is defined as $\mathcal{L}_i^k = \mathcal{T}_i^k - \overline{\sigma}_l^k$. Consistent with model scaling law for σ_l^k, the stress tensor $\mathcal{T}_i^k$ is modeled as

$$\mathcal{T}_i^k - 1/3\,\zeta_i^k \mathcal{T}_{\ell\ell} = 2C\overline{\overline{\Delta}}^2 |\overline{\overline{S}}| \overline{\overline{S_i^k}} \tag{5.13}$$

Using the identity, the resolvable tensor $\mathcal{L}_i^k$ in the computational space becomes

$$\mathcal{L}_i^k - 1/3\,\zeta_i^k \mathcal{L}_{\ell\ell} = 2C\overline{\Delta}^2 \mathcal{M}_i^k \tag{5.14}$$

$$\mathcal{M}_i^k = \alpha^2 \overline{\overline{|S|}}\,\overline{\overline{S_i^k}} - \overline{\overline{|S|}}\,\overline{\overline{S_i^k}} \tag{5.15}$$

Following the least-squares minimization procedure of Lilly (1992), the GDM coefficient in equation (5.7) is computed as

$$C = -\frac{\mathcal{L}_i^k \mathcal{M}_i^k}{2\overline{\Delta}^2 \mathcal{M}_i^k \mathcal{M}_i^k} \tag{5.16}$$

In this equation, the tensorial components in $\mathcal{L}_i^k$ and $\mathcal{M}_i^k$ are given in equations (5.12) and (5.15), respectively..

After substitution of equations (5.7) and (5.10) into equation (3.3a), the final form of momentum in the computational space becomes

$$\frac{\partial \sqrt{g}\,\overline{u}_l}{\partial t} + \frac{\partial \overline{u}_l \overline{U}^k}{\partial \xi^k} = \frac{\partial \sqrt{g}\,\xi_{x_l}^k (\overline{p} + 1/3\,\tau_{\ell\ell})}{\partial \xi^k} + \frac{\partial}{\partial \xi^k}\left[(\nu_T + 1/\mathrm{Re})\sqrt{g}\, g^{k\ell} \frac{\partial \overline{u}_l}{\partial \xi^\ell} + \nu_T U_f^k \right] \tag{5.17}$$

In the total diffusion term, the Crank-Nicolson and Adams-Bashforth schemes were used for the Cartesian and contravariant velocity component terms, respectively.

5.4. Test Filter

Smagorinsky's coefficient in equation (5.6) or equation (5.16) can be computed by test filtering either the physical or spectral elements. The functions most often used are that of a sharp cutoff, Gaussian or box filter. While the box filter is applied to the physical space variables, both the sharp cutoff and Gaussian filters operate in the spectral domain. Their resultant effect on the physical field can vary considerably however. For example, the number of backscatter points found by Piomelli et al. (1991) in a DNS data set of a turbulent channel flow decreased by 40 percent after using a Gaussian filter function as oppose the sharp cutoff filter. This reduction is attributed to the continued removal of turbulent scales by the Gaussian filter below the cutoff wave number. Attenuation of the spectral components also occurs below the cutoff wave number when applying a box filter, but not to the same degree as the Gaussian function.

The tensorial components in the above definitions for Smagorinsky's coefficient were computed here through application of a box filter. This filter was chosen because it is easy to implement and computationally efficient. The function of the box filter in Cartesian coordinates has the form

$$G(x_i, x_i') = \begin{cases} 1/\overline{\Delta}_i, & \text{if } |x_i - x_i'| < \overline{\Delta}_i/2 \\ 0, & \text{otherwise} \end{cases} \tag{5.18}$$

where $\overline{\Delta}_i$ is the filter width in the coordinate direction x_i. In curvilinear coordinates, the box filter function appears as

$$G(\xi_i, \xi_i') = \begin{cases} 1, & \text{if } |\xi_i - \xi_i'| < 1/2 \\ 0, & \text{otherwise} \end{cases} \tag{5.19}$$

In either the physical domain (Cartesian coordinates) or the computational space (curvilinear coordinates), the box filter is administered in discretized form. The one-dimensional discretized form of the box is

$$\overline{\phi}_i = \phi_i + 1/2S(\phi_{i+1} - 2\phi_i + \phi_{i-1}) \tag{5.20}$$

where $\bar{\phi}_i$ is the filtered quantity at point i, and S is the filter coefficient; S = 0.5 for the box filter with grid point averaging. Attenuation of the spectral field by the corresponding Fourier component in terms of a response function R(k) is

$$R(k) = 1 - S[1 - \cos(k\bar{\Delta})] \tag{5.21}$$

With S = 0.5, the response function shows that the box filter attenuates the spectral elements at all wavenumbers (except k = 0) without a phase change. The discretized box filter function in three-dimensions is a 27-point operator defined as

$$\begin{aligned}\bar{\Phi}_i = \Phi_i &+ 1/2S(1-S)^2[\Phi_{i\pm1,j,k} + \Phi_{i,j\pm1,k} + \Phi_{i,j,k\pm1}] \\ &+ 1/4S^2(1-S)[\Phi_{i\pm1,j\pm1,k} + \Phi_{i\pm1,j,k\pm1} + \Phi_{i,j\pm1,k\pm1}] \\ &+ 1/8S^3[\Phi_{i\pm1,j\pm1,k\pm1}]\end{aligned} \tag{5.22}$$

which attenuates the spectral domain according to (S = 0.5)

$$R(k_1,k_2,k_3) = \cos^2(k_1\bar{\Delta}_1)\cos^2(k_2\bar{\Delta}_2)\cos^2(k_3\bar{\Delta}_3) \tag{5.23}$$

The subscripts 1, 2 and 3 in this function indicate the three coordinate directions. It should be pointed out that this same response function can also be derived from the Fourier components of a box filter operation with volume averaging (see Schumann, 1975).

The discretized filter function in equation (5.22) is administered in either the physical domain or computational space without alteration. As shown in the preceding two sections, the difference between the operations lies only in the filtered components. Inasmuch as a filter ratio α is introduced (which is set equal to 2), the difference in the respective filter widths between the physical domain and computational space does not affect the computation of the turbulent eddy viscosity.

As previously noted, experience with the dynamic model has demonstrated that diverging solutions will result if *ad hoc* measures are not exercised to eliminate points of negative total viscosity. Usually, it is not enough to simply truncate all negative contributions to zero. Additional measures have been necessary such as averaging in homogeneous directions (sometimes assumed), combined with subsequent spatial or temporal filtering of the coefficient itself. These measures reduce the directional dependence of the coefficient and

dampen or even eliminate discrete points contributing to backscatter. In the LES results of the cavity flow presented in the next chapter, one measure was absolutely required to inhibit divergence. Because the stability limits of the numerical scheme prohibit negative diffusion, all field points carrying negative total viscosity were cutoff to zero. Consequently, backscatter contributions were permitted in the turbulence model, but their magnitudes were truncated to the equivalent of negative molecular diffusion.

5.5 *Verification of Smagorinsky's Model*

Before the damped and dynamic versions of the SGS turbulence model were tested, the model as originally introduced by Smagorinsky was first incorporated into the fractional-step computational sequence and verified. Verification of the model was a relatively straightforward task since the procedure is well-established in the literature. The test case entails predicting the decay of isotropic turbulence. A 64x64x64 uniform grid was used with periodic boundary conditions along all surfaces. The procedure requires producing a divergence-free initial flow field through specific treatment of the output from a random number generator. The total energy and energy spectra of the initial velocity field were adjusted to exactly match spectra taken from experimental data; in this case, turbulent data reported by Comte-Bellot and Corrsin (1971). Comte-Bellot and Corrsin produced a homogeneous, isotropic turbulent flow using a square wire mesh. The idea of the computation is to advance the initial field (by the LES scheme) to a later time where the energy spectra acquired from experimental measurements is also known. At the later time, comparisons of the LES results and experimental data are made to study the performance of Smagorinky's model.

Since the turbulence is homogeneous and isotropic, Smagorinsky's coefficient is constant. According to Piomelli et al. (1988). $C_S = 0.1$. Initial flow conditions were generated that mimicked the turbulent velocity field of Comte-Bellot and Corrsin (1971) at time T = 240; $T = U_0 t/M$ where U_0 is the upstream velocity (10 m/s), M is the mesh size (2.54 cm) and t is physical time. This initial field was advanced to target time T = 385. Both DNS and LES computations were performed to assess implementation of Smagorinsky's model and the grid's resolution.

DNS and LES results of the decay of homogeneous, isotropic turbulence are shown in Fig. 5.1 at time T = 276. Both computations were stopped, but for different reasons. Since no turbulence model is invoked in the DNS computations, the grid resolution must resolve all scales of the turbulent field. The 64x64x64 grid clearly did not meet this requirement by evidence of the energy build-up at the higher wavenumbers. If the DNS computation was allowed to continue, divergence was inevitable. Thus, a subgrid scale model was required to dissipate the cascade of turbulent energy from the finest resolved scales. The opposite effect however is indicated by the LES results. There, the energy levels were seemingly over-dissipated at the higher wavenumbers, but as discussed below, this is a false observation.

For this test case, the convective terms in the LES governing equations were differenced by second-order central differences. This differencing scheme is equivalent to filtering the computational results by a box filter. Attenuation of the initial and target turbulent energy spectra of Comte-Bellot and Corrsin (1971) by the box filter is shown in Fig. 5.3. As expected, the highest wavenumbers are most affected. After time-advancing the initial velocity field that matched the attenuated spectra, the final LES results agreed closely with the target spectra. This comparison is shown in Fig. 5.4. Thus, Smagorinsky's model with $C_S = 0.1$ was verified by this test case.

CHAPTER SIX
SHEAR DRIVEN CAVITY FLOW

6.1. Introduction

For more than three decades, the shear-driven cavity flow problem has served as an excellent test case for verifying new or improved numerical solution techniques of incompressible flows. Usually, the test case involves simulating a 2D cavity flow at a low Reynolds number (Re $\leq$ 1000). Under these conditions, the flow is strictly laminar and steady. The primary purpose of the simulations is to illustrate the rapid speed of convergence to steady state and the solution method's ability to capture the basic features of the flow. Some 2D simulations (for example, Ghia et al., 1982 and Gustafson and Halasi, 1986) include a discussion of the flow characteristics and have revealed important salient features of the steady flow at much higher Reynolds numbers (Re $\leq$ 10000). The extensive results of Ghia et al., in particular, serve most often as a base for comparison of new 2D predictions because of the fine grid resolution they used at the corresponding Re. Only a few numerical studies have reported the turbulent characteristics of the shear-driven cavity flow [Gosman et al., 1968, Young, et al., 1976, Ideriah, 1978, and Gaskell and Lau, 1988, for instance]. Each study simulated a 2D geometry with the turbulence fully modeled. Treatment of the results was focused primarily on validating the particular numerical scheme or evaluating the particular turbulence model.

Separate studies showing the flow evolution in the 2D cavity under an impulsively started lid and an oscillating lid were reported by Soh and Goodrich (1988). In both simulations, the flow was laminar (Re = 400) and the predictions continued until a periodic state was reached. Published results of 3D simulations include those of Kim and Moin (1985), Freitas et al. (1985), and Prasad et al. (1988) where the Reynolds number was restricted to low to moderate values (Re $\leq$ 3200). There, the flow was also laminar. The simulations showed the appearance of pairs of quasi-steady and unsteady spanwise Taylor-Görtler-like vortices along the cavity bottom. Besides validating the conservativeness of their particular solution technique, each group revealed this important 3D characteristic which had been observed experimentally, but was eluded numerically.

In addition to furnishing us with a classic problem for validating solution techniques of incompressible flows, the predominant features of the shear-driven cavity flow also have important physical significance in engineering design. For example, the main flow characteristics created by 3D geometries such as recessed cavities, recurrent ribs or slots and curved ducts, for the purposes of mass and/or energy exchange, are similar to those of this model problem. Given this fact, the primary objective of the computing the 3D cavity flow is to identify and characterize, through DNS and LES methodologies, the unsteadiness and turbulence. In the LES computations, both the damped and dynamic turbulence models are utilized for achieving this primary objective. There are also two secondary objectives for solving the cavity flow. While experimental verification of the DNS computations justifies the numerical molecule strategy, the LES calculations will acknowledge any improvements in the predictions by switching from the damped SGS model to the dynamic one.

The numerical investigations were performed for Reynolds numbers of 2000, 3200, 5000 and 10000. The moderate Reynolds number test cases ($Re \leq 5000$) were DNS computations because the flow is unsteady but laminar. The LES methodology was used for higher Reynolds number ($Re = 10000$). Although extensive experimental results of the high-Re 3D cavity flow have been reported for just over ten years now, this LES investigation is a first attempt to study the turbulent flow characteristics numerically. Recently, Zang et al. (1993) performed an LES calculation of the shear-driven cavity flow, but they focused the results on verification of their new dynamic turbulence model. They showed good agreement between the LES results and the experimental measurements in terms of the turbulent quantities through the cavity centerline at the spanwise mid-plane. Their investigation however did not include discussions of the time-dependent characteristics such as the spanwise vortices or the secondary eddies. In the present work, the numerical results are first scrutinized thoroughly against the experimental evidence, before discussing any new unsteady or turbulent flow characteristics. Thus, these LES computations verify the published experimental data as well as reveal some new features about the flow.

6.2. Experimental Observations

Geometrically, the classic 2D configuration consists of a closed cavity of unit height (H) and unit width (W) with a lid moving horizontally at unit velocity (U). The Reynolds number is defined as $Re = UW/\nu$, where ν is the kinematic viscosity. The associated recirculation flow is characterized basically by a primary vortex, a downstream secondary eddy, an upstream secondary eddy and an upper secondary eddy. These basic features are sketched in Fig. 6.1. The upper secondary eddy appears at $Re \geq 3200$. At higher Re (≥ 5000) the 2D predictions show a tertiary eddy in each of the lower corners. However, these tertiary eddies are not supported by the experimental observations of Koseff and Street (1984c) of the three-dimensional (3D) cavity flow. Koseff and Street also reported that the horizontal and vertical centerline velocity profiles of the recirculation flow are similar in shape throughout the cavity span at high Reynolds numbers where the flow is locally transitional.

In the 3D cavity, new vortical structures are formed. In a spanwise plane, there are several pairs of Taylor-Görtler-like (TGL) vortices and a lower corner vortex at the end-walls (see sketch in Fig. 6.2). According to Koseff and Street (1984b) and Prasad et al. (1988), the impetus manifesting the TGL vortices is the instability of the concave free shear layer that separates the primary vortex from the downstream secondary eddy. Generation of the vortices occurs just above the concave surface much like the experimental observations of Taylor (1923) for the flow between rotating cylinders and also the concave boundary layer investigated by Görtler (1954). The size and number of pairs of TGL vortices depends strongly on the Reynolds number and the cavity spanwise aspect ratio (SAR). In the flow visualization results reported by Rhee et al. (1984) for $Re \leq 6000$ and SAR = 3.0, the spanwise flow maintained symmetry about the mid-span plane. Although the TGL vortices meander slowly along the cavity bottom at moderate Re, Koseff and Street (1984a) noted that their basic spanwise flow character still remains symmetric. The other important feature in the spanwise direction is the lower corner vortex. The origin of this flow structure was explained by Koseff and Street (1984b) after examining the experimental results of de Brederoede and Bradshaw (1972). Manifestation of this vortex is a consequence of the shear and pressure force adjustment in the streamwise recirculating flow caused by the no-slip condition along the

spanwise end-wall. Like the TGL vortices, the corner vortex becomes unsteady at moderate Reynolds numbers (Re $\geq$ 3200). The size and extent of the corner vortex strongly influences the TGL vortices. Thus, the numerical simulations must provide sufficient resolution, spatially and temporally, to capture its characteristics accurately.

Experimental observations show the first sign of turbulence taking place within the free shear layer that lies between the primary vortex and downstream secondary eddy. This local transition to turbulence occurs at a Reynolds number somewhere between 6000 and 8000 (Koseff and Street, 1984a). The flow within that region is unsteady. If the Reynolds number is increased, turbulence diffuses the TGL vortices such that their deterministic structure becomes obscured. At Re = 10000, frequency spectra of both the horizontal and vertical fluctuations within the region of the free shear layer display an inertial subrange. It should be noted that the visualization results show the flow within the free shear layer at Re = 10000 as being still transitional.

6.3. Boundary and Initial Conditions

The DNS and LES computations involved two cavity geometries. The first cavity geometry, shown in Fig. 6.3, was modeled with a cavity width W = 1.0 (x-direction), a height H = 1.0 (y-direction) and a span L = 1.5 (z-direction). One boundary of the span was modeled as a plane of symmetry (z = 0.0) and the other a solid end-wall (z = 1.5). The span boundaries were model in this way because the published flow visualization data for Re $\leq$ 6000 (Koseff and Street, 1984a, 1984a and 1984c) and previous simulations for Re $\leq$ 3200 (Freitas et al., 1985, Prasad et al., 1988 and Jordan and Ragab, 1993) report a symmetric flow about the mid-span. The spanwise aspect ratio of the cavity ($SAR \equiv 2L/W$) was therefore equal to 3.0. Reynolds numbers of 2000, 3200, 5000 and 10000 were simulated. In view of the experimental evidence, the cavity flow is entirely deterministic at low to moderate Reynolds numbers (Re $\leq$ 5000). Therefore, the simulation results reported here at Re $\leq$ 5000 are from DNS predictions. For the LES computation at the highest Re, the SGS turbulent field was represented by the van Driest damped model.

The second cavity geometry was the same as the first except the full span was modeled with 2L = 1.0 (see Fig. 6.4). Thus, the second cavity had a SAR = 1.0. The computations involved Reynolds numbers equal to 5000 and 10000. A DNS computation was carried out for the lower Re (Re = 5000) while the LES methodology was exercised for Re = 10000. For LES computation, only the dynamic SGS model was used. It is worth noting at this point that in the recent LES computation by Zang et al. (1993), the cavity spanwise aspect ratio was 0.5. While all the TGL vortices display strong spanwise meandering activity in the cavity with a SAR = 3.0 and a weaker activity with SAR = 1.0, the single TGL vortex pair in the cavity with a SAR = 0.5 is locked in position at the mid-span (Prasad and Koseff, 1989).

In the present work, the lid moved horizontally with unit velocity (U = 1.0). Each simulation was initialized by an impulsively started lid. Inasmuch as the convective terms are time-split by the Runge-Kutta technique, extremely small time increments were not necessary early in the simulation to maintain stability. It was found that CFL values near the stability limit in the DNS computations at Re = 5000 distorted the TGL vortex structures. A low CFL value of 0.5 was therefore chosen to insure proper temporal resolution of the flow unsteadiness rather than control the numerical stability. This same CFL value was also used in the LES computations. No-slip conditions were enforced along all boundaries except at the mid-span plane in the first cavity (SAR = 3.0) which was treated numerically as a plane of symmetry. All grids selected had uniform point spacing and all times (T) were non-dimensional; $T = tU/W$. Computational results which are labeled T_r = 0.0 represent solutions that had been time-advanced until the transient effects of the impulsively started lid on the flow evolution became negligible.

As a final note, in the DNS computations of these cavity flows the CPU requirement was approximately 1.3×10^{-5}s per grid point per Runge-Kutta step on a CRAY-YMP platform. This requirement compares competitively to the computational requirements reported by Kim and Benson (1992); 1.7×10^{-5}s (iterative time marching), 2.5×10^{-5}s (simplified marker-and-cell), and 4.5×10^{-5}s (PISO).

6.4. *DNS Results (Cavity SAR = 3.0)*

6.4.1. Re = 2000

For the cavity flow test case at Re = 2000, a 41 x 41 x 51 uniform grid (x, y, z directions) was used with CFL = 2.4. A high resolution in the spanwise direction was chosen to insure prediction of the complete TGL vortex structure. Three sets of snapshots are shown in Fig. 6.5 of the recirculation and spanwise flow at non-dimensional times of T_r = 0.0, 8.0 and 16.0. The recirculation velocity vectors typify the flow at the mid-span plane. For clarity, they are normalized with respect to their own magnitudes; thus, the vectors shown in the snapshots have unit length. The spanwise velocity vectors show the flow at a plane where x $\cong$ 0.77; subsequently called the I77 plane. At the initial time (T_r = 0.0), three small TGL vortex pairs span the cavity bottom with a large corner vortex located at the lower end-wall. The corresponding recirculation flow displays strong 2D features which is a consequence of the weak spanwise flow. After an additional eight time units however (T_r = 8.0), the TGL vortex closest to the mid-plane nearly doubled its physical size. This now larger vortex pair impacts the recirculation flow locally by extracting kinetic energy from the downstream region; consequently reducing the size of the downstream secondary eddy. At time T_r = 16.0, three TGL vortices clearly appear with a fourth much weaker one positioned near the corner vortex. The prediction of four TGL vortices at Re = 2000 agrees with the flow visualization results reported by Rhee el al. (1984).

In the flow visualization experiments at this Reynolds number, the TGL vortices meandered slowly along the cavity bottom as well as varied their physical size. This behavior is also illustrated in Fig. 6.6 where five snapshots of the computations are shown at unit time intervals beginning with T_r = 26. The sequence of snapshots show creation and stationary growth of a TGL vortex pair directly next to the mid-span plane. Conversely, the TGL vortex closest to the end-wall is reduced and reverses its lateral path three times. Furthermore, this particular vortex meanders across approximately 15 percent of the cavity bottom. The remaining two TGL vortices also display large variations in their physical size, but meander comparatively to a much lesser degree.

To graphically verify the claim of strong coupling between the velocity components and pressure variable, three pressure variable profiles are displayed in Fig. 6.7. The pressure variable is plotted instead of the actual pressure to avoid the natural smoothing of the diffusive term as given in equation (2.4d). The profiles represent cuts at $y = 0.1$ through the free shear layers that separate the primary vortex from the secondary eddies. These profiles extend from the upstream wall ($x = 0.0$) to the downstream wall ($x = 1.0$) at the mid-, 1/3rd and 2/3rds planes along the cavity span. Notice that the profiles depict smooth continuous curves that are devoid of spurious oscillations. These characteristics illustrate proper coupling between the pressure variable and velocity components as given by the discretization molecule.

6.4.2. Re = 3200

A 51 x 51 x 65 uniform grid was selected for the test case at Re = 3200 and a CFL value of 1.5. This mesh resolution was partially based on the simulation reported by Freitas et al. (1985) where a 32 x 32 x 45 grid was used that was non-uniform in the recirculation planes. Figs. 6.8a and 6.8b show typical snapshots of the unsteady flow ($T_r = 12.0$). The recirculation velocity vectors (Fig. 6.8a) represent the flow at the mid-span plane whereas the spanwise flow (Fig. 6.8b) is shown at the I77 plane. Once again for clarity, the recirculation velocity vectors are normalized with respect to their own magnitudes. Four TGL vortex pairs span the cavity bottom. Their position is marked by grid lines referenced to the cavity mid-span. This number of TGL vortices agrees with the experimental observations reported by Rhee et al. (1984). Normalized recirculation velocity vectors representing 18 minute sample averages at the 1/3rd and 2/3rds planes from the spanwise end-wall are shown in Fig. 6.9a and 6.9b, respectively. At these planes, downstream and upstream secondary eddies are clearly visible. Freitas et al (1985) also reported this result and both numerical results agree with the flow visualization data (Rhee et al, 1984 and Koseff and Street, 1984b). Furthermore, the 1/3rd plane vectors show the primary vortex core positioned in the upper right quadrant of the recirculation plane whereas the core at the 2/3rds plane lies close to the geometric center. This result also agrees

qualitatively with the experimental observations and is due to the proximity influence of the end-wall on the recirculation flow.

The experimental and computed time-averaged u and v velocity profiles through the cavity center at the mid-span are compared in Figs. 6.10a and 6.10b, respectively. Also included in the figure are the steady 2D velocity profiles for a 51 x 51 uniform grid and the time-averaged 3D results of Freitas et al. (1985). Comparisons between both 3D computations and the experimental results are quite good. On the other hand, comparisons between the 2D computation and the 3D results are quite poor. This confirms the conclusion drawn by Koseff and Street (1984b), that the three-dimensional effects on the recirculation flow manifest significant differences between the 2D and 3D mean velocity profiles. One should notice that the present time-averaged velocities away from the cavity walls agree better with the experimental data than the corresponding results of Freitas et al (1985) for two possible reasons. The first is their lower sampling window, but more importantly, they sacrificed the grid field resolution by clustering lines near the cavity walls in the recirculation planes.

6.4.3. Re = 5000

For the DNS computation of the shear-driven cavity flow at Re = 5000, the a 65 x 65 x 65 (x, y, z-direction) uniform grid was used. Comparisons between the DNS results and the experimental data show that this spatial resolution captured the flow characteristics accurately. Further refinement of the grid did not alter the flow structure. Figs. 6.11a and 6.11b show a set of snapshots of the unsteady flow results at time T_r = 15.0. The velocity vectors in Fig. 6.11a represent the recirculation flow at the mid-span plane whereas those in Fig. 6.11b depict the spanwise flow at the I77 plane. Although there seems to be significant effects in the upper half of the spanwise plane, their magnitudes are small and therefore have little influence on the flow structure. At this instant in time (T_r = 15.0), the basic characteristics of the recirculation flow which are common to the 2D simulations are distinctly visible. Likewise, the primary vortex core is positioned close to the cavity center. This agreement with the 2D simulations is due primarily to the minimal influence of the spanwise flow on the mid-span recirculation flow (see Fig. 6.11b). The spanwise flow vectors

show four TGL vortices of nearly the same height that lie fully within the cavity span. Since the static pressure attains a minimum within the vortex core, contours of the pressure variable can verify the existence of each vortex. An example of this is portrayed in Fig. 6.11c. A few grid lines are superimposed over the pressure contours and the corresponding velocity vectors to help identify each respective vortex.

At time T_r = 181.0, the snapshots paint a very different picture (see Figs. 6.12a and 6.12b). The three-dimensional effects on the basic recirculating flow features are clearly displayed. For example, the TGL vortex that straddles the mid-span plane severely distorts the basic structure of the downstream secondary eddy (DSE). Throughout most of the simulation, a TGL vortex structure straddled the mid-span plane which precluded development of the local DSE. According to the experimental results (Rhee et al., 1984), 8 pairs of TGL vortices were visualized at Re = 3200 and 11 vortex pairs at Re = 6000. At Re = 5000, 9 vortex pairs were found; one typically straddling the mid-span plane and four others spanning the cavity floor. This result is shown in Fig. 6.13 which is a plot of the x-vorticity contours at completion of the simulation (T_r = 181.0). Notice that the streamwise extent of each vortex pair does not strongly interact with the upstream secondary eddy (USE). This is because the flow process of fluid entrainment from the primary vortex to sustain the structural integrity of each TGL vortex is terminated once the primary vortex separates upstream. Particle traces which illustrate this flow process are presented in the next section.

In the literature, neither velocity time traces nor mean velocity experimental data appear for the 3D cavity flow at Re = 5000 and SAR = 3.0. Here, we show in Figs. 6.14a through 6.14d time traces of a vertical and horizontal velocity component and their power spectra for the Re = 5000 test case. The traces were extracted from recordings taken in the vicinity of the downstream free shear layer. For reference, the power spectra include Kolmogorov's slope of the inertial sub-range. Both spectra show numerous amplified frequencies signifying an unsteady flow which is still deterministic. In Fig. 6.15, the computed mean horizontal velocity along the mid-span center-line is compared against the reported experimental data for SAR = 1.0 and SAR = 0.5 (Prasad and Koseff, 1989). The DNS profile illustrates a further weakening of the

"energy-sink" effect of the spanwise end-walls on the primary recirculation vortex core when the cavity SAR is extended to three.

The contribution of the present DNS results at Re = 5000 to the LES methodology lies in attempting to estimate the turbulent length scale damping parameters. In particular, parametric studies were performed on the DNS results at intermittent time intervals to find values for the exponents (m and n) in the van Driest damping function. There is no strong fundamental basis for obtaining these parameters in this way since the flow is not turbulent at Re = 5000. However, the LES results at Re = 10000 (where the flow is turbulent) will show that the turbulent eddy viscosity magnitudes and distribution throughout the cavity were in good agreement with the experimental evidence. The procedure used here to determine the model damping parameters closely follows the SGS turbulence model development by Clark et al. (1977). The damping parameters were judged according to the best overall set of coefficients acquired from correlations between the exact (computed from the DNS data) and the model results in terms of the SGS stresses τ_{ij}. The correlation coefficient (c_{ij}) is defined as

$$< c_{ij} >=< e_{ij} m_{ij} > / < e_{ij}^2 >^{1/2} < m_{ij}^2 >^{1/2} \qquad (6.1)$$

where $< e_{ij} >$ and $< m_{ij} >$ are the spatially ensemble-averaged exact and model τ_{ij} components, respectively. Inasmuch as the spanwise flow direction was assumed to be homogeneous, only the coefficients c_{11}, c_{22} and c_{12} were determined of which only positive values were considered. Furthermore, signs of transition first emerge within the downstream free shear layer (Koseff and Street, 1984a). By knowing this information a priori, it is also possible to perform quality checks on the model in terms of the turbulent eddy viscosity magnitudes and distribution. In the following figures, the turbulent eddy viscosity (ν_τ^*) is normalized by the kinematic viscosity. Since the TGL vortices severely disturbed the basic features of the recirculating flow, the model quality was inspected only on planes lying between the spanwise vortex pairs.

The best set of fully-averaged correlation coefficients attained from a parametric study of the DNS results was c_{11} = 0.30, c_{22} = 0.29 and c_{12} = 0.31. The corresponding global model constants are m = 8.0, n = 0.14 and C_s

= 0.1. Distribution of the c_{12} coefficient, plotted in Fig. 6.16, shows pockets of nearly perfect correlation close to the cavity walls and near the region of downstream free shear layer. Notice that the poorest correlations occur primarily where the model ν_τ^* levels are expected to be low. As an example, see Fig. 6.17a where the highest ν_τ^* levels found in the individual recirculation planes are shown for the DNS results at completion of the simulation. This figure also reveals that the model predicts ν_τ^* magnitudes and distributions in accordance with the experimental observations.

As a final note, the model constants as acquired from the Re = 5000 simulation were also checked against DNS results from a higher Reynolds number test case (Re = 7500) where the flow is locally transitional (Koseff and Street, 1984a). The highest ν_τ^* levels computed on the individual recirculation planes are shown in Fig. 6.17b. Indeed, the peak levels of ν_τ^* are concentrated within the downstream free shear layer which is in agreement with the experimental data.

6.5. LES Results (Cavity SAR = 3.0)

The uniform grid selected for the LES computations at Re = 10000 was 101 x 101 x 81. Based on the turbulent scales estimated by Koseff and Street (1984c) for the 3D cavity flow at Re = 10000, this grid provides a higher spatial resolution than that needed to resolve Taylor's microscale. Shown in Figs. 6.18a and 6.18b are snapshots of the velocity field at a sample time T_Γ = 6.5. The spanwise velocity vectors represent flow at the I77 plane while the DSE region is shown at various planes between the TGL vortices. Besides the corner vortex, the spanwise velocity vectors show five additional vortex structures that appear distorted when compared to the DNS results at the lower Reynolds number (Re = 5000). Breakdown of the TGL vortex structure is due to the onset of turbulence within the adjacent downstream free shear layers. Prasad and Koseff (1989) (SAR=1.0) and Koseff and Street (1984a) (SAR=3.0) also reported a loss of TGL vortex structure at this Re, but were unable to visualize the vortex flow patterns due to the rapid lateral dispersion of the dye streaks. The existence of the vortex structures and their streamwise extent is further illustrated in Figs. 6.19 and 6.20 in the form of stream function contours. In Fig. 6.19, these contours are computed on each recirculation plane (x-y) as if

the flow is 2D and then stacked side-by-side from the spanwise end-wall to the symmetry plane. The stream function contours in Fig. 6.20 are computed similarly on the z-y planes and then stacked in the x-direction from the downstream to the upstream walls. In both figures, only the stream function contours from the lower half of the cavity are shown. The marking of grid lines in Fig. 6.20 and in the velocity vectors (Fig. 6.18b) help quantify the intensity, spanwise size and streamwise extent of each vortex. The instability mechanism of TGL vortex generation still exists at this Re as evidenced by the vortex structure created above the DSE between grid lines 49 and 62. Like the DNS results, neither the TGL vortices nor the corner vortex interact with the USE. Thus, the basic structure of the USE remains intact throughout the cavity span. On the other hand, the irregular development of the DSE in the spanwise direction suggests complex interactions between the unsteady effects of the primary recirculation vortex and the TGL vortices. As an example, Koseff and Street (1984b) and Prasad et al. (1988) reported appearances of spiraling spanwise motions within the DSE which they attributed to its interaction with the local vortices. Verification of their observations as well as uncovering other interactions are presented next.

Between the spanwise vortices shown in Fig. 6.20, the stream function contours form four surfaces that give a cave-like impression. Beneath these surfaces, the basic two-dimensional structure of the DSE develops due to separation of the primary recirculation vortex from the downstream wall (see Fig. 6.18a). The vortices adjacent to the DSE strongly influence its spanwise characteristics. An attempt to understand these complicated characteristics as well as the other flow features of the 3D cavity at Re = 10000 is illustrated in Fig. 6.21 at the sample time T_r = 6.5. There, five sets of particle traces were initiated either within the DSE region or the outer extremes of the primary recirculation vortex; in particular, the first computational point off the downstream wall (x = 0.99). Also, each set originated half way up the downstream wall (y = 0.5) except set number five which started at y = 0.05. Set number 1 contains three particle traces that were initiated directly over the center of the large TGL vortex (grid line k = 10). After release, all three particles were entrained by the downwash flow of the large vortex. Their spiraling path then traversed streamwise only a short distance before being entrained by the

upwash region of the vortex as given by the mid-span recirculation flow. Particles from sets three and four had a similar fate. Set number three initiated above and to the left of the TGL vortex at grid line k = 28 while set four originated between the TGL vortices marked grid lines k = 28 and k = 36. Initially, each particle was convected by the primary recirculation vortex which traced a path that coincides with the streamline surface shown in Fig. 6.19. As the particles neared the cavity bottom, they were entrained by the respective vortex instead of the DSE. The reason for this is illustrated by particle sets two and five. Set two started above and to the right of the TGL vortex at grid line k = 28 while set five was centered just above the tiny flow structure that is positioned between grid line k = 62 and the end wall. As the particles of set two approached the cavity bottom they were entrained by the DSE. However, because the large adjacent vortex induced a dominant spanwise velocity component on the DSE, the particles traced a broad spanwise spiral which turned quickly streamwise once fully entrained by the vortex. This spanwise spiral within the DSE region is also traced by particle set number five. From these observations, we can conclude that the streamwise extent of the TGL vortex structures shown in Fig. 6.20 are sustained through two patterns of fluid entrainment. Close to the downstream wall, these vortices entrain fluid from the adjacent DSE regions which in turn extract fluid from the primary recirculation vortex. As mentioned earlier, this flow pattern was also observed locally in the 3D cavity in the flow visualization experiments. Upstream from the DSE region however, the TGL vortices entrain fluid from the primary vortex directly. Loss of the vortex structure occurs upstream once the primary vortex separates from the cavity bottom.

Having this understanding of the flow pattern within the DSE region, the tiny flow structure between grid line k = 62 and the span's end wall is a another vortex pair. Creation of this secondary vortex pair is due to the opposing spanwise viscous interactions of the corner vortex, the adjacent TGL vortex and the no-slip condition along the cavity bottom. Above its center position lies an imaginary surface within the DSE region that demarcates fluid entrained by the corner vortex apart from that extracted by the adjacent TGL vortex. The existence of this flow surface is illustrated by the right and left particle traces in set number five. As shown in Fig. 6.21, the spanwise spiral

trace of each particle is in opposite directions. Thus, these particles started on opposite sides of the flow surface. Because the adjacent TGL vortices change size and meander along the cavity floor over time, the flow surfaces and corresponding secondary vortices are not stationary. As a matter of fact, flow visualizations of the numerical results showed extremely complicated dynamics that governed these tiny structures. However, their impact on momentum and energy transfer throughout the cavity was never significant.

The effects of the symmetry plane assumption on these LES results will now be discussed. Koseff and Street (1984c) noted that the mean recirculation flow in the 3D cavity with SAR = 3.0 became similar when the Reynolds number was increased to 10000. By examining the comparisons between the computed center-line mean velocity profiles and the experimental results in Figs. 6.22a and 6.22b, one can see that this is indeed the case. While the experimental data is at the mid-span plane, the computed profiles are shown along the center-line of recirculation plane z = 0.28; hereinafter called the K15 plane. In both profiles, the averaged error (as compared to the data) is less than 2 percent. Thus, the symmetry plane assumption has a negligible effect on the mean recirculation at the K15 plane and throughout the remainder of the cavity span. Unfortunately, no center-line Reynolds stresses or turbulent velocity fluctuations were published of the 3D cavity flow with SAR = 3.0. However, data was reported by Prasad and Koseff (1989) at the mid-span plane for SAR = 1.0. Quantitative comparisons between that data and the LES results at the mid-span, K15 and end planes are shown in Figs. 6.23a and 6.23b in terms of the center-line root-mean-square (rms) velocity fluctuations. The end plane profile in each figure was computed at recirculation plane z = 1.25. Both figures clearly show large discrepancies between the computed and experimental mid-span plane rms results. Conversely, rms profiles at the K15 and end planes agree reasonably well with each other as well as with the experimental mid-span plane data. Furthermore, the computed profiles extend the overall observed trend that turbulent kinetic energy is lost near the cavity walls when the cavity SAR is reduced (Koseff and Street, 1984b and Prasad and Koseff, 1989) . Hence for this test case, these observations along with the experimental agreement of the computed mean recirculation flow illustrated a localized effect of the spanwise symmetry plane assumption on the LES results.

Finally, we could pose the following questions. Do these LES computations support the explicit understanding that turbulence dominates the flow characteristics near the downstream free shear layer ? And at this Reynolds number, what are the spatial distributions of the velocity fluctuations elsewhere in the cavity ? Figures 6.24a and 6.24b show the energy spectrum of the velocity fluctuations calculated from a T_r = 90 sample record taken in the vicinity of the downstream free shear layer. Both spectral profiles display an inertial subrange with about an order of magnitude larger energy content within the vertical fluctuations. This result as well as the bandwidth over which the inertial subrange occurs agree with similar analyses conducted on the experimental data (Koseff and Street, 1984c). In Figs. 6.25a and 6.25b, distributions of the vertical rms fluctuations and shear stress component $\overline{u'v'}$ at the K15 plane indeed disclose highest levels within the downstream free shear layer region. However, one should note that the rms levels of the vertical velocity fluctuation are also significant along the downstream wall.

6.6. DNS Results (Cavity SAR = 1.0)

The final uniform grid chosen for this test case was a 101x 101x 85 (x, y, z directions). Recirculation streamlines at the cavity mid-span plane and spanwise streamlines at the I77 plane are plotted in Figs. 6.26a and 6.26b, respectively. Counter-rotation is signified by the dashed contours. These streamlines were computed from snapshots taken of the instantaneous velocity vectors at reference time T_r = 0.0 which represents an actual time of T ≅ 60 since lid start-up. The streamlines in the figures distinctly reveal a downstream and upper secondary eddy in the recirculation flow and two TGL vortex pairs which lay nearly symmetric about the mid-span plane. Prediction of these two TGL vortices as well as the overall spanwise symmetry agrees with the flow visualization observations of Prasad et al (1988). In Fig. 6.27, the mean recirculation flow vectors (averaged over T_r = 180) at the mid-span plane show downstream and upstream secondary eddies, but the upper eddy seems to have been averaged out. Koseff and Street (1984b) published results at a slightly higher Reynolds number (Re = 5700) and showed a similar result.

Mean velocity profiles through the geometric center of the mid-span and one-third (z = 1/3) planes is plotted in Fig. 6.28 along with the mid-span

experimental measurements of Prasad and Koseff (1989). The stronger boundary layer but weaker core flow shown in the one-third plane profile is due to the higher energy drain on the primary recirculation vortex by the spanwise end-walls. Overall, the DNS results show good agreement with the experimental data, but the specific differences in magnitude between them suggest that line clustering near the cavity walls as given by a stretched grid would provide better spatial resolution.

As previously discussed, the DNS results were interrogated to estimate the predictive ability of the SGS turbulence model. Without the zero cutoff restriction, application of the model to the DNS results at $T_r = 0.0$ gave global correlation coefficients of $c_{11} = 0.42$, $c_{22} = 0.39$ and $c_{12} = 0.40$. The x-y distribution of the c_{12} coefficient (ensemble-averaged in the z-direction) is shown in Fig. 6.29a where the dashed contours signify negative correlations. Generally the distribution is quite good, except near the upstream secondary eddy region where $c_{12} \rightarrow -1.0$. The highest ν_τ^* levels found on the recirculation planes are shown in Fig. 6.29b. Since the zero cutoff restriction was not applied, the figure shows regions of negative total viscosity; $\nu_T/\nu < -1.0$. However, their magnitudes are insignificant and are concentrated in the extreme upper downstream corner. With the cutoff restriction applied, the overall correlation coefficients and their distributions changed very little (Fig. 6.29c). Analysis of the DNS results at the final time ($T_r = 180$) also revealed no discernible differences with or without the zero cutoff restriction (see Figs 6.30a and 6.30b). Note also that the distributions shown in these figures are generally the same as those in the initial data ($T_r = 0.0$) except for the higher negative correlations near the upper secondary eddy region.

6.7. LES Results (Cavity SAR = 1.0)

The same spatial resolution used for the DNS prediction just presented was tested for the LES computation. According to the turbulent scale estimates published for this cavity flow (Koseff and Street, 1984c), a 101x101 uniform distribution in the recirculation plane resolves the fine-scale turbulence near the downstream free-shear layer at least down to Taylor's microscale. In the simulation, the computations had continued until the energy spectra of the turbulent velocity fluctuations was well established at several points in the

cavity where the flow was reported as most turbulent (Koseff and Street, 1984c). A time sequence of recirculation and spanwise streamlines at the mid-span and I77 planes are shown in Figs. 6.31a through 6.31f. As before, the dashed contours depict counter-rotating flow. Although various other flow patterns are displayed by spanwise streamlines in the upper half of the cavity, their contribution to the instantaneous momentum transfer was insignificant. From an overall viewpoint, the high degree of non-uniformity in the streamlines suggests a substantial growth of flow unsteadiness in the 3D cavity from Re = 5000 to Re = 10000. This growth accounts for the large temporal changes in the downstream and upstream separation and reattachment points as well as the apparent differences in the primary vortex core.

At this Reynolds number, Prasad and Koseff (1989) noted no detection of TGL vortices in their velocity time traces which were recorded slightly above the cavity floor along the mid-span vertical centerline. As illustrated in Fig. 6.31 however, TGL vortices apparently exist near the DSE region. But unlike the DNS results (Re = 5000), their temporal and spatial attributes appear to vary randomly. This characteristic is further exemplified in Fig. 6.32 where a sequence of snapshots of the spanwise vortices are shown over a period of T_r = 120. At certain times, the vortices display signs of strong uniform structural integrity, while at other times their structure is locally contorted and irregular. This behavior suggests that the flow within the DSE region of the cavity is transitional. The regions of TGL vortex breakdown is due the intermittent high-frequency turbulent fluctuations that occur within the adjacent downstream free shear layer of the recirculating flow.

The experimental Prasad and Koseff (1989) and LES mean flow quantities through the cavity centerline at the mid-span plane are compared in Figs. 6.33a through 6.33d. The average error in the computed mean flow velocities with respect to the experimental data is 5 percent for the horizontal velocity profile and 4 percent for the vertical velocity profile. Once again, as in the DNS profiles, the magnitude differences between these profiles indicate the need for a finer grid resolution near the cavity walls to improve the accuracy of the computed mean flow. Comparison between the experimental and computed horizontal and vertical root-mean-square (rms) velocity profiles is shown in Figs. 6.33c and 6.33d. Their close agreement clearly shows that the dynamic

model performed well. As an example, the subtle fluctuation in the experimental data near the cavity floor is adequately captured by the LES results. Furthermore, agreement between the peak magnitudes suggests that the dynamic model properly dissipated the high-wave number turbulence ($k\Delta x \geq \pi$).

Significant backscatter contributions by the dynamic model were confined primarily to the upper downstream corner. This condition is shown in Fig. 6.34 at typical times of $T_r = 10$ and $T_r = 157$ in terms of the maximum ν_t^* levels found on the recirculation planes as computed by the model without the cutoff restriction. Notice that the dynamic model predicts the highest positive levels of turbulent activity near the DSE region. Furthermore, the levels indicate that the turbulent eddy viscosity within that region is on the same order of magnitude as the kinematic viscosity. This result infers that the onset of turbulence occurs within the DSE region and that the flow at this Reynolds number is probably transitional. According to the experimental measurements and observations, this prediction is qualitatively correct.

As a final note, the maximum power spectral energy of the velocity fluctuations at the mid-span in the vicinity of the DSE is shown in Figs. 6.35a (horizontal direction) and 6.35b (vertical direction). The contours represent the maximum density levels taken from the frequency spectra results of the individual time trace data. To obtain the time trace data, the instantaneous velocities were sampled at a frequency of approximately 20 Hz. According to the figures, peak energy levels of the vertical velocity fluctuations are substantially higher than the horizontal velocity levels and occur at different locations with the DSE region. Spectral density levels of the vertical fluctuations crest near coordinates (0.83, 0.07) while the corresponding horizontal levels peak near coordinates (0.85, 0.12). Both figures however show a rapid decline of energy levels away from peak. Typical spectral frequency results of both velocity fluctuations are plotted in Figs. 6.36a (horizontal) and 6.36b (vertical). For reference, each plot includes Kolmogorov's slope of the inertial subrange. Both figures show the existence of an enertial subrange over approximately one decade beginning at approximately 0.1 Hz.

6.8. Conclusions

The LES and DNS methodologies were used to study the unsteady and turbulent characteristics of the three-dimensional shear-driven cavity flow at Reynolds numbers 2000, 3200, 5000 and 10000. The 3D shear-driven cavity flow was also used as an example problem to study the performance of the dynamic model in a LES computation. Lilly's expression without any *ad hoc* measures such as ensemble-averaging or filtering was tested for determining the model coefficient. But due to the conditional stability of the numerical scheme, negative total viscosity was cutoff to zero to preclude divergence. Based on the numerical results, the following conclusions are offered:

6.8.1. SAR = 3.0

- At Re = 2000 (DNS results), the flow is laminar. Pairs of TGL vortices are created that maintain their size while slowly meandering in a direction toward the mid-plane. Between the TGL vortices, the recirculation flow features are comprised of a primary vortex and a downstream and upstream secondary eddy. These basic features agree with the experimental observations and the two-dimensional steady flow results.
- At Re = 3200 (DNS results), the flow is also laminar. While meandering towards the mid-plane, the TGL vortices now change size and their enhanced spanwise extent distorts the basic features of the adjacent recirculation flow.
- At Re = 5000 (DNS results), the flow is still entirely deterministic, but the three-dimensionality and unsteadiness severely disturbs the basic structure of the classic recirculation flow features. The TGL vortices change rapidly in size and they meander only locally. Nine TGL vortex pairs were predicted that span the cavity bottom. One of the TGL vortices straddles the mid-span plane.
- At Re = 10000 (LES results, damped SGS model) the instability mechanism for TGL vortex generation still exists, but the vortices themselves have now become distorted due to the onset of turbulence within the downstream free shear layer. Their physical characteristics throughout the 3D cavity vary randomly. The combined effects of the primary recirculation vortex and the TGL and corner vortices cause a complicated irregular development of the DSE. Near the downstream wall the TGL vortices extract fluid from the downstream eddy region which concurrently entrains fluid from the primary

recirculation vortex. Upstream of the downstream eddy region, the TGL vortices entrain fluid directly from the primary vortex. Lastly, secondary vortex pairs are created intermittently within the DSE region due to the viscous interactions among the adjacent larger vortices and the cavity floor.

- A van Driest damped turbulence model was used for the subgrid scale field. The constants of length scale damping function in the model were estimated from a DNS computation of a deterministic flow (Re = 5000). The spatial distributions of the vertical rms fluctuations and shear stress as given by the model for the turbulent flow agreed with the experimental data.

6.8.2. SAR = 1.0

- Exclusive of the upper corners, the dynamic model with Lilly's expression for Smagorinsky's coefficient predicted low turbulent levels throughout the cavity volume at Re = 5000. This result occurred for both the initial (T = 0.0) and final (T = 180) DNS results and is consistent with the published experimental data.
- At Re = 10000 (LES results, dynamic SGS model) where the cavity flow is now locally turbulent, the dynamic model gave significant contributions of backscatter only in the upper downstream corner of the recirculation flow. The distributions of the turbulent eddy viscosity predicted by the model agreed qualitatively with the reported experimental data. Good quantitative agreement between the LES and experimental turbulent rms fluctuations showed that the dynamic model performed well in this particular application. In fact, the LES results using the dynamic model improved the comparisons to the experimental data by a significant margin.

CHAPTER SEVEN
WAKE OF A CIRCULAR CYLINDER

7.1 Introduction

A comprehensive study of the turbulent vortex formation behind a circular cylinder as well as the transport of the vortices downstream has many important and practical implications. As a example, the shedding characteristics associated with an airfoil can be similar to that of the cylinder. Resolution of these characteristics in the wake possesses an excellent challenge for LES. In the case of the circular cylinder, the large scale vortex motion remains strongly coherent for many diameters downstream. Since the impetus of LES is full resolution of the large scale motion, the computational results can provide specific information regarding the cyclic formation and downstream transport of the turbulent vortices including their individual internal physics.

Only two LES investigations of the circular cylinder have been previously reported. The first was a 2D study by Song and Yuan (1990) at a high Reynolds number. Since vortex stretching strongly dominates turbulence production in the near wake (Cantwell and Coles, 1983), the 2D simulation of Song and Yuan ignored important physical phenomena. The other study was reported by Kato et al. (1993) who concentrated on predicting aerodynamic noise in the near wake. Their 3D LES computations by the finite element method provided the fluctuating pressures along the cylinder surface for the Lighthill-Curle equation of the radiated far field sound pressure. Due to their simple SGS turbulence model however, and relatively coarse mesh in the wake, good agreement with the experimental data in terms of the turbulent energy power spectrum was obtained only at the low frequency levels. For their particular need, resolution of the fine scale turbulent physics was unimportant.

The present LES investigation is centered on resolving the early wake formation of a circular cylinder as well as the subsequent vortex shedding motion in the near-wake. The Reynolds number in the simulation was 5600, which is based on the cylinder diameter (D) and a uniform freestream velocity (U_∞). To adequately encompass the near wake, a non-orthogonal O-type grid topology was generated. Consequently, the mathematical form of the governing

LES equations were in curvilinear coordinates. Before performing the LES investigation however, the fundamental form of the transformed equations were first verified for the cylinder flow problem at a much lower Re. Specifically, early wake formation and the subsequent vortex shedding behavior were simulated at Re = 200. This particular Reynolds number is a good choice for verifying the numerical accuracy of the solution scheme because a wealth of the experimental and numerical data already exists in the literature. For the turbulent wake flow at Re = 5600, the transformed LES equations with the GDM were solved in the computational space. Inasmuch as non-orthogonal topologies are often necessary to properly resolve the flow characteristics in many problems including the cylinder wake, this generalized LES formulation with the turbulence model has extensive applicability.

Two important attributes of any cylinder flow calculation are the lift and drag forces. In the discussions below of these forces, the conventional forms of the lift and drag coefficients (C_L and C_P) are presented. Values for C_L and C_P were determined by

$$C_L = C_{L_P} + C_{L_\omega} \qquad C_D = C_{D_P} + C_{D_\omega} \tag{6.1}$$

where $C_{L_p} = \frac{1}{2}\int_0^{2\pi} P_S D \sin\theta \, d\theta$, $\quad C_{L_\omega} = \frac{1}{Re}\int_0^{2\pi} \omega_S D \cos\theta \, d\theta$,

$C_{D_p} = \frac{1}{2}\int_0^{2\pi} P_S D \cos\theta \, d\theta$, $\quad C_{D_\omega} = \frac{1}{Re}\int_0^{2\pi} \omega_S D \sin\theta \, d\theta$

The quantities P_S and ω_S are the pressure and vorticity magnitudes along the cylinder surface, respectively. Also along the surface, the distribution of the pressure coefficient is presented. This coefficient is defined as $C_p = (P_S - P_0 + \frac{1}{2}\rho U_\infty^2)/(\frac{1}{2}\rho U_\infty^2)$ where P_0 is the pressure value at the upstream stagnation point. Since the LES equations are actually non-dimensional, the coefficient of pressure is appropriately calculated from $C_p = 1 + 2(\overline{p}_S - \overline{p}_0)$ where $\overline{p}$ is the filtered cell pressure quantity computed along the cylinder surface. Finally, the vortex shedding frequency is quantified by the Strouhal number which is defined by $S_t = fD/U_\infty$ where f is the frequency of shedding.

7.2 Some Important Experimental Observations

Formation of the near wake depends partially on the developed boundary layer upstream of separation. Proper resolution of the upstream boundary layer is therefore critical to achieving accurate results of the near wake physics.

Insurance that sufficient resolution has been established within that region can be gained by verifying the computational results early in the simulation both qualitatively and quantitatively. In this section, a brief description of the important early flow characteristics is given over the range of Reynolds numbers in the simulations. This description considers an implusive start of the flow and is taken from published experimental observations of Bouard and Coutanceau (1980). It will later serve to verify the computational results from a qualitative perspective.

At non-dimensional time $T = 0^+$, the flow around the circular cylinder is symmetrical and everywhere irrotational (Telionis, 1981); $T = tU_\infty/D$. Two stagnation points exist; one each along the horizontal centerline on the upstream and downstream sides of the cylinder surface. For times $T > 0^+$ and $Re > 4.4$, the adverse pressure gradient on the downstream side causes the developing boundary layer to separate forming the cylinder wake. Early evolution of the wake characteristics (before any instabilities) depends strongly on the Reynolds number; although for the Reynolds numbers considered here ($Re \leq 5600$), the wake formation remains essentially symmetric. Up until $Re \cong 500$, the early developing spatial scales of the wake (length and width, for example) are entirely characterized by a single vortex which is hereinafter identified as the main eddy (actually two main eddies since the wake is symmetric). For $100 \leq Re \leq 500$, the flow path of main eddy deviates from the cylinder surface curvature forming a knot in the streamline pattern (see Fig. 7.1a). This distortion of the main eddy manifests a kink in the external boundary of the wake. Generally, this pattern develops at $T \cong 1$. At slightly higher Reynolds numbers ($500 \leq Re \leq 800$) and $T > 1$, the knot matures into a secondary eddy whose flow path is counter-rotative to the main eddy (Fig. 7.1b). The kink in the wake's external boundary concurrently becomes more pronounced and is much easier to visualize experimentally. If $Re > 800$, the secondary eddy grows with time until it occupies a portion of the recirculation region just beyond the separation point. The eddy then adjusts to the local exterior shear layer of the separated region by splitting into two smaller eddies as shown in Fig. 7.1c. These smaller eddies are permanent, nearly equivalent in size, and completely isolate the main eddy from the separation physics associated with the upstream boundary layer. Pairs of secondary eddies have

also been detected at much higher Re, especially during the infancy stages of the wake's evolution. For example, the sketch in Fig. 7.1d illustrates an early pair of elongated secondary eddies which have been observed when Re > 3000 and T < 1.5. As time progresses, this eddy pair quickly thickens and appears to coalesce to form the main eddy of the wake. During that time, the permanent secondary eddy pair originates adjacent to the separation point. The important characteristics just described will be recalled to verify the qualitative accuracy of the curvilinear coordinate formulation and the corresponding solution scheme.

For reasons still not physically apparent, the cylinder wake eventually destabilizes when Re > 40 and transitions into a persistent pattern of alternating shed vortices. As the vortices convect and diffuse downstream from the cylinder, they mark the well-known Karman vortex street. Experimental measurements of the shed vortices in near wake at Re = 5600 were reported by Zhou and Antonia (1993). As shown in Fig. 7.2, they identified the near wake as $0.5 \leq x \leq 60$ where x is the non-dimensional downstream centerline distance referenced to the cylinder center. At Re = 5600, the boundary layer along the cylinder surface is still laminar up to separation. Beyond the separation point, the wake quickly destabilizes and forms the alternating periodic vortices. The shedding of vortices occurs at $S_t \cong 0.2$. According to Zhou and Antonia, the vortices themselves in the near wake are fully turbulent. Their topology is sketched in Fig. 7.2 where little variation is shown in their relative cross-sectional area. Zhou and Antonia measured no change in the vortex cross-sectional area for $10 \leq x \leq 60$. At x = 10, the convection velocity (U_c) of the shed vortices was about 85% of the freestream velocity and slowly increased further downstream. At x = 60 for example, $U_c \cong 0.92\ U_\infty$. The experimental measurements revealed a loss of peak vorticity within the vortices with distance downstream, but their relative internal vorticity distribution remained unchanged. Also, the time-averaged velocity fluctuations showed a relative decrease with distance downstream. Peak horizontal magnitudes occurred at the vortex center while the vertical distributions closely mimic the circumferential velocity of an Oseen vortex. A large part of the work of Zhou and Antonia was focused on developing an Oseen vortex model to correctly predict the magnitudes and transport of the turbulent vortices. Their

experimental results provided empirical adjustments to the model parameters to better represent the true internal turbulent physics of the vortices in the near wake.

7.3 Boundary and Initial Conditions

The downstream boundary conditions for the cylinder flow problem are by no means a trivial matter. They must allow the shed vortices to exit without affecting the vortices themselves or wake physics further upstream. Customarily, one chooses to set the streamwise gradients of pressure and velocity to zero at the downstream boundary (Rhie and Chow, 1983 for example), or update the exit conditions by second-order extrapolation (Lin and Pauley, 1993). For the cylinder flow problem however, both these conditions caused the vortices to experience severe distortions at exit. In the first attempt to correct this dilemma, the exit conditions recommended by Pauley et al. (1990) for Cartesian coordinate systems were simply rewritten for the computational space and applied. Pauley et al. successfully used the linear convection equation as a downstream boundary condition for the velocity components in a 2D DNS computation of vortex generation over a flat plate. In the application of the reformulated equations for the cylinder flow problem, no definition was enforced for the pressure variable. This condition was permissible because the pressures are staggered form the velocities in the computational molecule. Although the structural integrity of the vortices appeared unaffected by transforming the exit conditions of Pauley et al., the pressure solution required many iterations to converge. Convergence took much longer than expected because no provision is available in the application of the linear convection equation for satisfying continuity at the exit boundary. The second attempt to achieve a functional downstream boundary condition involved combining Eulers equation with continuity. Again, no conditions were invoked for the pressure variable. This exit condition significantly reduced the convergence requirement for the pressure solution, but over predicted the pressure distribution around the cylinder. An excessive amount of pressure built up in the wake region adjacent to the cylinder due to a reflection of pressure waves from the exit boundary. Consequently, these conditions did not yield an unstable wake in the Re = 200 computation even with the exit

boundary located 6 diameters downstream of the cylinder center. The most successful conditions required the specification of a zero tangential gradient of pressure along the downstream boundary in addition to the contravariant velocity definitions. This set of boundary conditions rendered the fewest pressure iterations, accurate drag and lift predictions, and no discernible disturbance to the vortices at exit.

Mathematically, the downstream boundary conditions for the cylinder flow problem were

$$\frac{\partial \overline{U}^i}{\partial t} + \xi^i_{x_j} \overline{U}^k \frac{\partial \overline{u}_j}{\partial \xi^k} = -\sqrt{g} g^{ik} \frac{\partial \overline{p}}{\partial \xi^k} \qquad \text{(Euler)} \qquad (7.1)$$

$$\frac{\partial \overline{U}^i}{\partial \xi^i} = 0 \qquad \text{(Continuity)} \qquad (7.2)$$

Because pressure is not known along the downstream boundary, it was eliminated from Eulers equation by insuring that either the metrics (through orthogonality) or the pressure gradients were appropriately set to zero. Eulers equation then reduced to the non-linear convection equation which was combined with continuity to establish a velocity exit condition. As a typical example, consider the plane where η is constant (ξ, ς plane). First, the grid lines are orthogonal (or nearly orthogonal) along the boundary so that all off-diagonal metrics in Eulers equation are negligible. The contravariant velocity component $\overline{V}$ is determined from continuity (7.2), whereas the other two components ($\overline{U}, \overline{W}$) are obtained using Eulers equation (7.1) with the tangential pressure gradients along the ξ, ζ plane set equal to zero.

The initial conditions for the cylinder flow problem were the following. The flow was impulsively started with a unit velocity, zero reference pressure and a fixed non-dimensional time step of $\Delta T = 0.0002$; $T = tU_\infty/D$. A small time step initialized each simulation to guarantee incompressibility very early in the computation. Once incompressibility was attained (at least 100 time steps), the new velocity and pressure conditions just described were imposed along the downstream boundary. The inner boundary which was the cylinder surface was always no-slip and the upstream centerline axis was a branch cut. Boundary conditions for the velocity components and pressure variable along the coincident lines of the branch cut were identical to those traditionally

administered for periodic boundaries. For each grid generated, the curvilinear lines were made normal to the cylinder surface. This simple requirement greatly facilitated implementation of the intermediate velocity boundary condition in the curvilinear space. Finally, the spanwise boundary conditions for the pressure variable and velocity components were periodic in the LES simulations.

7.4 Results and Discussion

Reynolds numbers of 200, 3000 and 5600 were simulated for the flow over a circular cylinder. As noted earlier, the LES investigation of the cylinder flow was focused on the turbulent physics at Re = 5600. The lower Re values served other purposes. Because the entire flow is deterministic at Re = 200, its solution was in essence a 2D DNS computation. The primary purpose of this computation was to verify the accuracy of the numerical approach and to ascertain a consistent downstream boundary condition which will exit the shed vortices without noticeably disturbing them. The LES results at Re = 3000 had a dual purpose. Not only were the effects of the GDM examined, but the results also served as a check for the minimum spatial resolution needed along the cylinder surface in the LES computation at Re = 5600. This check was justified because Bouard and Coutanceau (1980) discerned similar structural characteristics of early wake formation behind the circular cylinder for $1000 < Re < 10000$. Through comparisons to their reported experimental measurements of early wake formation, the Re = 3000 computation helped estimate the minimum grid required adjacent to downstream cylinder surface for the higher Re simulation.

7.4.1. Re = 200

Two separate concentric orthogonal grids were generated to verify the numerical scheme at this Re. The coarse grid was 81x79 (ξ,η directions) with $(\Delta y)_{min} = 0.005$ and the second finer grid comprised 121x99 with $(\Delta y)_{min} = 0.004$. The exterior boundary in each grid was fixed at 6 diameters. Comparisons of the predicted exterior boundary of the early wake with the experimental data (Bouard and Coutanceau, 1980) are shown in Fig. 7.3 for times 0.5, 1.0, 2.0 and 3.0. This exterior boundary represents the zero streamline. Using the finer grid, the computation shows good agreement to the

experimental data, but still under predicted the maximum point of wake growth by 3.7 percent. Comparisons of the corresponding velocities along the downstream horizontal centerline are shown in Fig. 7.4. In this figure, results from the coarse grid computation are included at time T = 3.0 to demonstrate grid convergence. The computation using the fine grid gave a 30 percent improvement in the average error over that of the coarse grid. The maximum error of the fine grid computation (located at the minimum point of velocity) was 10 percent whereas the coarse was 15 percent.

Initial signs of an unstable wake appeared at approximately T = 25.0. Transition from the stable wake to emergence of the vortex shedding phenomena took about 13 time units. Snapshots of this evolution in the form of streamlines are shown in Fig. 7.5 at times T = 26, 30, 34 and 38. The components of lift (C_{Lp} and C_{Lw}) and total lift (C_L) are plotted in Fig. 7.6a from time T = 0.02 (after the initial transients) to time T = 98.0. Total drag and its components over this same period of time are shown in Fig. 7.6b. Both figures illustrate a moderate growth in the oscillating magnitudes of lift and drag up to their maximums. Beginning at time T= 38 (after the transition period), this phase of the wake flow transpire over approximately 32 units of time to T = 70. Beyond this time, the near wake is distinctly characterized by a steady oscillatory flow with a Strouhal number of 0.205. Time-averaged values of lift and drag calculated over 7 cycles starting at T = 70 are listed in Table 7.1. Experimental determinations as well as other numerically acquired values are also listed. Agreement between the present computed force coefficients and the others is acceptable.

7.4.2. Re = 3000 and Re = 5600

The final grid for the LES computations of the turbulent wake was 241x241x16 (x,y,z directions). In both simulations at Re = 3000 and 5600, the inflow and outflow boundaries were set at 10 and 20 diameters, respectively. The grid resolution and outflow boundary location were established through comparisons to the experimental data in terms of early wake formation at Re = 3000 and the downstream loss of peak vorticity within the individual shed vortices at Re = 5600. The distribution of points along the cylinder surface (s) was $\Delta s \cong 0.011\pi$ for the upstream laminar boundary layer and $(\Delta s)_{min} \cong 0.003\pi$

for the turbulent wake. Normal to the cylinder surface $\langle \Delta y^+ \rangle = 4$ for Re = 5600. The spanwise spacing was uniform at $\Delta z \cong 0.04\pi$.

Two snapshots of the early wake formation for Re = 3000 are shown in Fig. 7.7 at non-dimensional times of T = 1.0 and T = 1.5. For emphasis and clarity, the velocity vectors shown in the figures are plotted at every other grid point and each vector is normalized by its own respective magnitude. At time T = 1.0 (Fig. 7.7a), the entire wake is characterized by two elongated symmetric vortices. These vortices are the wake's main eddies. Compared to the cylinder diameter, the wake at this instance in time is relatively narrow. After a short period of time ($\Delta t = 0.5$) however, the main eddies grew rapidly to over twice their original size (see Fig. 7.7b). Two secondary eddies also arose between each main eddy and the upstream separation point. It is these features that persist throughout the remaining development of the stable wake. While the main eddies drive the downstream maturity of the wake, the secondary eddies locally thicken the wake and, more importantly, they interact with the upstream separation point. These characteristics of early wake development at Re = 3000, as given by the LES computation, agree qualitatively with the experimental observations (Bouard and Coutanceau, 1980).

Bouard and Coutanceau (1980) measured early wake formation and the concurrent horizontal velocity profiles behind a circular cylinder at Re = 3000. Comparisons of those measurements and the present LES computations are shown in Fig. 7.8 at times T = 1.0 and T = 2.5. The computational results shown in the figures are taken from the span's mid-plane. DNS results are included in the velocity comparisons to examine the effects of the GDM. Although the LES and DNS results agree closely with the experimental velocity measurements at T = 1.0, a higher grid resolution is necessary to capture the complete wake profile. This requirement is due to the rapid growth of the main eddies at this particular instance in time that quickly thicken the overall extent of the wake. At T = 2.5 (Fig. 7.8b), agreement between the LES results and experimental measurements is good for both the wake formation and the velocity profiles. Conversely, the DNS computations under predicted the minimum horizontal velocity component in the wake by 5 percent. This difference signifies the importance of the GDM contribution even at this lower Reynolds number (Re = 3000).

Presentation of the LES results at Re = 5600 begins with snapshots of the early wake development at times T = 1.0, 1.5 and 3.0; Fig. 7.9. The first snapshot at time T = 1.0 shows the appearance of an elongated secondary eddy which separates each main eddy from the upstream separation point. Compared to the previous results at Re = 3000, this secondary eddy is a new feature for Re = 5600. Its resolution by the LES computation agrees with the experimental observations discussed earlier. Like the Re = 3000 results, the main eddies at Re = 5600 grew rapidly when T > 1.0 (see Fig. 7.8b). Furthermore, each elongated secondary eddy split into two asymmetric eddies. As time progressed to T = 3.0, the main eddies grew assiduously, but two tertiary eddies evolved within each secondary eddy region. One tertiary eddy appears adjacent to the upstream separation point while the other borders the main eddy. The evolution of these eddies was not discussed by Bouard and Coutanceau (1980). With further advancement in time, these five structures (one main eddy, two secondary eddies and two tertiary eddies) characterize the early formation of the stable wake.

The wake began to destabilize after the cylinder moved approximately 11 diameters (T ≅ 11) since its impulsive start. Fig. 7.10 shows the corresponding streamlines and pressure contours. The wake closure point along the horizontal centerline is located approximately 2 diameters downstream. Except near wake closure, no discernible signs of asymmetry are displayed by the streamlines. Conversely, the pressure contours indicate distinct asymmetric attributes within the secondary and tertiary eddy regions of the wake adjacent to the cylinder surface as well as near wake closure. After the cylinder traversed two additional diameters, the entire wake became asymmetric by evidence of the streamlines in Fig. 7.11. Tendencies towards wake destabilization are now more obvious. Asymmetry in the pressure contours are again noticeable within the secondary eddy regions. Judging from both sets of pressure contours shown at times T = 11 and T = 13, the mechanism which destabilizes the early wake apparently initiates near the secondary separated regions adjacent to the cylinder surface. However, the vorticity contours do not support this observation. They are shown in Fig. 7.12 where negative vorticity is represented by dashed lines. Like the streamlines, the vorticity contours at time T = 11 are asymmetric only near wake closure. At the later time however,

the mechanism which seems to characterize destabilization of the wake has propagated upstream along the exterior wake boundary. The vorticity contours shown in Fig 12b at time T = 13 indicate severe breakdown of the wake's downside exterior boundary. The corresponding pressure and streamline plots show only broad subtle dimples in the contours at these same locations.

Early profiles of total lift and drag are plotted in Fig 7.13 up to time T = 25. Initially, the drag force quickly builds to a maximum, after which it exponentially decays to a constant level before transitioning to oscillations characteristic of vortex shedding. Total lift, on the other hand, remains at zero (as it should) while the wake is stable. The figure shows that the total drag and lift coefficient are in phase and the drag's fundamental frequency is twice that of the lift's. These characteristics are in agreement with our basic understanding of the early wake formation.

Vorticity contours taken just after occurrence of a typical shed vortex are shown in Fig. 7.14 where the dashed contours denote negative vorticity. The shed vortex size is approximately equal to one diameter. The snapshot clearly shows a separated mixing layer of small eddies just aft of the lower separation point. According to the experiments of Roshko (1954) and Tritton (1959), instabilities within this mixing layer precipitate transition. The corresponding turbulent eddy viscosity levels (υ_T^*) as predicted by the GDM without the zero cutoff are shown in Fig. 7.15. These levels are normalized by the kinematic viscosity with negative levels represented by dashed lines. The GDM properly predicts minor levels within the upstream laminar flow regions. For this particular flow structure, significant negative contributions are restricted to within the attached upper primary and secondary eddies.

During the computation over twenty shedding cycles, the shedding frequency displayed a large variation. This variation was also observed by Norberg (1992) in his flow visualization experiments. Norberg noticed that when Re > 5000, the flow becomes spasmodic. This particular phase is associated with local "bursts" occurring in the cylinder wake that cause a complete breakdown in the similarity of the vortex shedding characteristics. The "bursts" originated large relative bandwidths in Norberg's pressure measurements along the cylinder surface.

In an attempt to detect Norberg's "burst" phenomena in these LES computations, profiles of the lift and drag force coefficient over approximately 23 shedding cycles along with the amplitudes of the corresponding frequency spectra are shown in Fig. 7.16. Maximum peak in the lift spectra occurs at f = 0.21 which identifies the Strouhal frequency. This fundamental frequency is close to the value of 0.205 reported by Zhou and Antonia (1993) and characterizes one complete cycle of vortex shedding (actually two vortices). Other peaks in the lift frequency spectra are of minor consequence. The drag force frequency spectra suggests a different story. Two dominate peak amplitudes occur in the spectra at f = 0.19 and f = 0.45. Another two peaks appear at f = 0.09 and f = 0.27, but both are of lesser amplitude. Inasmuch as the periodicity of the drag coefficient is one-half that of the lift, the fundamental harmonic in the drag frequency spectra is expected to be near $1/2\ f_s$ (or $\cong$ 0.105) with the higher frequencies $1/2\ (n+1)\ f_s$ (n = 1, 2, 3 $\cdots$) signifying subharmonics. The predominate modes in the drag frequency spectra follow this criteria approximately, except for the fact that the amplitudes of the subharmonics (f = 0.19 and f = 0.45) are higher than the amplitude associated with fundamental frequency. This occurrence may be partially explained by the "burst" phenomena observed by Norberg in his pressure measurements. However, the natural frequency (f_b) of the mixing layer vortices also plays an important role; f_b is used here to acknowledge the original work of Bloor (1964). This frequency characterizes manifestation of Tollmien-Schlichting waves in the mixing layer. Since the natural frequency of the mixing layer is higher than the Strouhal frequency (Bloor, 1964), interacting modes of f_s with f_b can excite certain subharmonics in the drag force frequency spectra thereby producing higher amplitudes. Without a temporal pressure record in the mixing layer however, it is difficult to isolate the mixing layer contribution. Further work addressing this issue is therefore certainly warranted.

LES pressure results along the cylinder surface are compared to Norberg's time-averaged measurements in Fig. 7.17. While the mean pressure shows good agreement with the experimental data, the highest rms magnitudes are over-predicted. Qualitatively however, the rms results are in very good agreement with the experimental data. The corresponding mean drag

coefficient is 1.18 which is the same value obtained after time-averaging the drag coefficient data in Fig. 7.16b.

In the cylinder wake, the vortex detection frequency of the Strouhal vortices displayed a large variation. A snapshot of the vortices is shown in Fig. 7.18 where again the dashed contours denote negative vorticity. Notice particularly, the non-uniform streamwise and relative transverse spacing between subsequent vortices. This characteristic was typical of the wake region throughout the computation and explains the wide variability seen in the detection frequency. The time-averaged (20 cycles) downstream decay of the vortex detection frequency is plotted in Fig. 7.19 along with experimental data points from Zhou and Antonia (1993) at exit and at $x = 10$. Agreement between the LES results and the experimental measurements is good even close to exit, indicating the use of a proper exit condition for the vortices.

Comparisons of the LES mean horizontal velocity and Reynolds stresses with the experimental time-averaged data reported by Zhou and Antonia (1993) at 10 diameters downstream ($x = 10$) are shown in Fig. 7.20. In the experiments of Zhou and Antonia, they took measurements over a duration of 30 seconds at a shedding frequency of 110 Hz. Thus, their experimental data in Fig 7.20 represents approximately 3300 cycles of time-averaged measurements. On the other hand, the LES results were collected over only 20 cycles which is apparently insufficient to establish statistically steady-state as illustrated by the wavy profiles in the Fig. 20. The mean velocity, in particular, clearly reflects the passing of the Strouhal vortices. The profile marks the passing of counter-rotating vortices at $y/D < 0$. Moreover, because a coarse spanwise resolution was used ($\Delta z \cong 0.04\pi$), the contours of Reynolds stress do not reflect any spanwise instabilities. One positive note however is that the LES results do agree at least qualitatively with the experimental data.

Finally, contours of mean streamwise and crossflow Reynolds normal stress and mean Reynolds shearing stress in the vicinity of the immediate wake are plotted in Fig. 21. Again, the contours display LES results that were time-averaged for 20 shedding cycles which appears to be sufficient to reach near statistical steady-state in the immediate wake by evidence of the distinct symmetric character of the contours. The figure shows negligible levels of

Reynolds stress correctly computed by the SGS model in the upstream laminar boundary layer. Unfortunately, Zhou and Antonia (1993) did not conduct measurements in the immediate wake, therefore no direct comparisons to experimental data can be made. However, Cantwell and Coles (1983) reported Reynolds stress data in the immediate wake, but for Re = 140,000. Although the present computation is for Re = 5600, both Reynolds numbers are below drag crisis (Re ≅ 300,000) which means they share similar dynamics. Qualitatively, the Reynolds stress results for both Reynolds numbers do compare quite well. In particular, the distributions of the normal and Reynolds stress in Fig. 21 appear quite similar to that reported by Cantwell and Coles. Quantitatively however, both results differ, but not by a large margin. For instance, the maximum measured Reynolds shear stress at Re = 140,000 was 0.125 which compares to the computed value of 0.16 for Re = 5600.

7.5 Conclusions

DNS and LES computations were conducted to investigate the wake of a circular cylinder. The governing equations and SGS model (LES computations only) were formulated in curvilinear coordinates where both the Cartesian and contravariant velocity components were utilized. For the simulated Reynolds numbers of 200, 3000 and 5600 the following conclusions are offered:

- The Euler equation combined with continuity provided a mechanism for exiting vortices with minimal disturbance to their characteristics.
- DNS results at Re = 200 showed good comparisons to the experimental data in the form of the early wake and shedding characteristics. The DNS results verify the curvilinear form used here for the Navier-Stokes equations.
- At Re = 3000, good agreement was obtained between the LES results and the experimental data in terms of early wake formation and the corresponding horizontal velocity profiles. The simulation verified the LES formulation and helped establish the grid resolution for the Re = 5600 computation.
- In the Re = 5600 simulation, initial destabilization of the early wake was predicted near wake closure which then propagated upstream establishing transition to full periodic vortex shedding. Unlike the DNS results at Re = 200, the vortices in the LES computation at Re = 5600 were not shed in a regular pattern forming the well-known Karmon-vortex street. Instead, the shedding

produced a wide variability of the instantaneous vortex detection frequency in the near wake. A similar phenomena was experimentally detected by Norberg (1993).

- The LES computation at Re = 5600 continued for 20 cycles. Computed mean and root-mean-square pressure results along the cylinder surface compared reasonably well with the experimental data of Norberg (1992). By evidence of the comparisons of the normal and shear Reynolds stresses to the experimental data of Zhou and Antonia (1993) at 10 diameters downstream, the computation must be carried-out further than 20 cycles to achieve statistically steady-state in the near wake. However, in the immediate near wake (just downstream of the cylinder), Reynolds stress results show distinct symmetric character. Qualitatively, these results compare quite well to the experimental data of Cantwell and Coles (1983) for Re = 140,000 indicating that both results share similar dynamics.

CHAPTER EIGHT
CONCLUSIONS AND RECOMMENDED FUTURE WORK

This dissertation presents the large-eddy simulation (LES) methodology for predicting the turbulent physics of incompressible flows in both simple and complex geometries. LES departs from traditional Reynolds-averaged Navier-Stokes methods in that a portion of the turbulence is resolved directly by the numerics. When using LES, one must insure that the resolved field encompasses all of the energy-dominant scales of turbulence and that the remaining scales, which lie at the subgrid level, are properly modeled.

The governing equations for LES are obtained by filtering the Navier-Stokes (N-S) equations. The basic form of LES equations, in either Cartesian or curvilinear coordinates, differs from the original N-S equations through introduction of a new stress term which arises after filtering the convective term. This new stress term represents the subgrid scales (SGS) of turbulence. While the SGS stresses are mathematically defined by the Cartesian velocity components in the physical domain, its analog formulation in the computational space is expressed by both the Cartesian and contravariant velocity components.

Herein, both forms of the LES equations were numerically advanced in time using a fractional step strategy. A semi-staggered structured grid arrangement was implemented as the primary computational molecule. This arrangement permits easy derivation of the velocity boundary conditions because the grid lines are coincident with the geometric boundaries. However, previous use of semi-staggered grids showed that while the pressure is strongly coupled to the velocity components, the grid cell pressures are not linked to their adjacent neighbors. This dilemma is overcomed here by computing the pressure gradients using a fourth-order compact differencing scheme. This development is new and crucial technology for those who prefer semi-staggered grids as part of the key solution strategy.

The SGS models available today are founded on Smagorinsky's eddy viscosity relationship and are valid within the equilibrium range of turbulence. In this dissertation, the coefficient in the Cartesian form of the SGS model was expressed in one of two ways. The first was a simple van Driest damping

relationship while the other utilized the finest scales of the resolved field. This latter method is quite recent, and is commonly known as the dynamic model. It permits negative values for the coefficient which signifies backscatter of turbulent energy from the model to the resolved field. Previous applications of the model indicate that the computations may experience long correlation times of negative total dissipation which will quickly destabilize the computation. To circumvent this difficulty, users truncated negative contributions to zero combined with either averaging of the turbulent field in homogenous directions or local averaging in time of the coefficient itself. These *ad hoc* measures however lessen the versatility of the dynamic model by reducing its temporal or direction dependence. Here, in the application of the dynamic model to the unsteady shear-driven cavity flow, only the zero cut-off restriction was necessary to maintain stability. Upon examining the distribution of the turbulent eddy viscosity throughout the cavity volume, it was found that contributions of negative total viscosity were localized in the extreme upper cavity corners. It is believed that this favorable artifact was a result of insuring that the grid resolution was sufficient for resolving the turbulent scales lower than Taylor's microscale. Although good comparisons in terms of the cavity mid-span centerline Reynolds stresses were achieved between the LES results and the experimental data using both the damped and dynamic models, the LES results using the dynamic model were superior by a large margin. These results showed highest levels of turbulent production within the region of the downstream secondary eddy. This conclusion agrees with the experimental observations. These results further showed that significant production levels also occur along the downstream cavity wall near the cavity mid-span which was not identified in reported experimental data. Thus, the LES results using the dynamic model extended our understanding of turbulent physics in the shear-driven cavity. From a qualitative perspective, these LES results uncovered the existence of fluctuating tertiary vortices within the downstream eddy region. However, the consequence of these vortices on the momentum exchange through the region was insignificant.

The curvilinear form of the LES equations and dynamic model, as well as the numerical method, were tested for predicting the wake characteristics of a circular cylinder. The model coefficient was computed using the definition for

the SGS stress tensor in terms of the Cartesian and contravariant velocity components. The computation at the low Reynolds number of 200 was essentially a direct numerical simulation. The numerical results compared well with the published experimental and numerical data thereby verifying the formulation and overall solution scheme. At the higher Reynolds numbers (Re) of 3000 and 5600, the boundary layer upstream of separation was laminar but the wake was fully turbulent. LES results of the early wake at Re = 3000 showed good agreement with the published experimental data. At Re = 5600, the computations were carried-out for approximately 20 cycles of vortex shedding. Reasonable agreement was shown between the LES results and the experimental data in terms of the Reynolds stresses at 10 diameters downstream, but the computation must be continued to attain smooth profiles. A coarse resolution was used in the spanwise directions, thereby eliminating any effects on the results due to spanwise instabilities. The experimental data was ensemble-averaged over approximately 3300 cycles. Future applications for the curvilinear formulation of the LES equations and dynamic model should include the circular cylinder at higher Reynolds numbers as well as other geometries such as airfoils or hydrofoils. An extensive experimental data set exists of the circular cylinder at Re = 140,000 (Cantwell and Coles, 1983). Successful applications to hydrofoils will lead to more complex domains such as propulsors (including ducted) and impellers. Furthermore, because LES resolves the most dominant scales of the turbulent field, the results can become a critical source for subsequent far-field noise computations in complex domains. All of these topics are currently under exploration to demonstrate the importance of LES in computational fluid dynamics.

Finally, extending the dynamic SGS model of Germano et al. (1991) to complex domains deserves some discussion. The Cartesian form of the dynamic model was directly transformed to curvilinear coordinates under the assumption that the accompanying metrics were not part of the filtering process. This assumption became apparent after examining the curvilinear coordinate definition of the SGS stress tensor. Adverse consequences (if any) of the assumption are not known at this time since a new dynamic which include the metrics would be necessary for comparison. This is a topic for future research. In regions close to wall boundaries for example, one might expect

large differences between the two models because the metrics usually display large variability there. A suitable model is currently under investigation.

REFERENCES

Anderson, D.A., Tannehill, J.C. and Pletcher, R.H., 1984, "Computational Fluid Mechanics and Heat Transfer," Hemisphere, Washington, DC.

Antonopoulos-Dimis, M. 1981, "Large-Eddy Simulation of a Passive Scalar in Istropic Turbulence", *Journal of Fluid Mechanics*, Vol. 104, pp. 55-79.

Akselvoll, K. and Moin, P., 1993, "Large-Eddy Simulation of a Backward Facing Step Flow," 2nd International Symposium on Engineering Turbulence Modeling and Measurements, May 31-June2, Florence, Italy.

Akselvoll, K. and Moin, P., 1993, "Application of the Dynamic Localization Model to Large-Eddy Simulation of Turbulent Flow Over a Backward Facing Step," FED-Vol. 162, ASME Fluids Engineering Conference., pp. 1-6.

Bloor, M.S., 1964, "The Transition to Turbulence in the Wake of a Circular Cylinder,", *Journal of Fluid Mechanics*, Vol. 19, pp. 290.

Bouard, R. and Coutanceau, M., 1980, "The Early Stage of Development of the Wake Behind an Impulsively Started Cylinder for $40 < Re < 10^4$," *Journal of Fluid Mechanics*, Vol. 101, pp. 583-607.

Cantwell, B. and Coles, D., 1983, "An Experimental Study of Entrainment and Transport in the Turbulent Near Wake of a Circular Cylinder," *Journal of Fluid Mechanics*, Vol. 136, pp. 321-374.

Chang, J.L.C. and Kwak, D., 1984, "On the Method of Pseudo Compressibility for Numerically Solving Incompressible Flows," *AIAA-84-0252.*

Chollet, J.P., 1984, "Two-Point Closure Used for a Subgrid Scale Model in Large Eddy Simulations", *Turbulent Shear Flows III, Springer*-Verlag, pp. 347-352.

Chollet, J.P., and Lesieur, M. 1981, "Parameterization of Small Scales of Three-Dimensional Isotropic Turbulence Utilizing Spectral Closures", *Journal of Atmospheric Science*, Vol. 38, No. 12, pp. 2747-2757.

Chorin, A.J., 1967, "A Numerical Method for Solving Incompressible Viscous Flow Problems", *Journal of Computational Physics*, Vol. 2, pp 12-26.

Chorin, A.J., 1969, "Numerical Solutions of the Navier-Stokes Equations," *Math. Comput.* Vol. 23, pp 745-762.

Ciofalo, M. and Collins, M.W., 1990, "Large Eddy Simulation of Turbulent Flow in Plane and Rib-Roughened Channels",*Turbulent Shear Flows VI, Springer*-Verlag, pp. 347-352.

Clark, R. A., Ferziger, J. H. and Reynolds, W. C., 1977, "Evaluation of Subgrid-Scale Turbulence Models Using an Accurately Simulated Turbulent Flow," *Journal of Fluid Mechanics*, Vol. 91, pp. 1-16.

Deardoff, J.W. 1970, "A Numerical Study of Three-Dimensional Turbulent Channel Flow at Large Reynolds Numbers", *Journal of Fluid Mechanics*, Vol. 41, pp. 453-480.

deBrederoede, V. and Bradshaw, P., 1972, "Three-Dimensional Flow in Nominally Two-Dimensional Separation Bubbles I. Flow Behind a Rearward Facing Step," I. C. Aeronautics Report 72-19.

Feiereisen, W.J., Shirani, E., Reynolds, W.C. and Ferziger, J.H., 1981, "Direct Simulation of Homogeneous Turbulent Shear Flows on the Illiac IV Computer: Applications to compressible and incompressible modelling",

Ferziger, J.H., 1985, "Large Eddy Simulation: Its Role in Turbulent Research", *Theoetical Applications to Turbulence*, Applied Mathematical Sciences, Vol. 58, Springer-Verlag.

Ferziger, J.H., 1987, "Simulation of Incompressible Turbulent Flows", *Journal of Computational Physics*, Vol. 69, pp. 1-48.

Freitas, C. J., Street, R. L., Findikakis, A. N. and Koseff, J. R., 1985, "Numerical Simulation of Three-Dimensional Flow in a Cavity," *International Journal of Numerical Methods in Fluids*, Vol. 5, No. 6, pp. 561-576.

Gaskell, P. H. and Lau, A. K. C., 1988, "The Method of Curvature Compensation and its Use in the Prediction of Highly Recirculating Flows," AIAA/ASME/SIAM/APS 1st National Fluid Dynamics Congress, pp. 272-279.

Germano, M., 1992, "Turbulence: The Filtering Approach," *Journal of Fluid Mechanics*, Vol. 238, pp. 325-336.

Germano, M., Piomelli, U., Moin, P., and Cabot W.H., 1991, "A Dynamic Subgrid-Scale Eddy Viscosity Model," *Physics of Fluids*, A. 3, pp. 1760-1765.

Ghia, U., Ghia, K. N. and Shin, G. T., 1982, "High-Re Solutions of Incompressible Flow Using the Navier-Stokes Equations and a Multigrid Method", *Journal of Computational Physics*, Vol. 48, pp. 387-411.

Ghosal, S., Lund, T.S. and Moin, P., 1992, "A Local Dynamic Model for Large-Eddy Simulation," Center of Turbulence Research, Annual Research Briefs, Stanford University, Stanford, CA.

Görtler, H., 1954, "On the Three-Dimensional Instability of Laminar Boundary Layers on Concave Walls," NACA Technical Memorandum, 1375.

Gosman, A. D., Pan, W. M., Runchal, W. M., Spalding, D. B. and Wofshtein, 1968, "Heat and Mass Transfer in Recirculating Flows", Academic Press, London.

Gustafson, K. and Halasi, K., 1986, "Vortex Dynamics of Cavity Flows," *Journal of Computational Physics*, Vol. 64, No. 2, pp. 279-319.

Harlow, F.H. and Welch, J.E., 1965, "Numerical Calculation of Time-Dependent Viscous Incompressible Flow of Fluid with Free Surface", *Physics of Fluids*, Vol. 8, pp. 2182-2189.

Haltiner, G.J. and Williams R.T., 1980, "Numerical Prediction and Dynamic Meteorology", John Wiley, New York, NY.

Hartel, C. and Kleiser, L., 1993, "Energy Transfer Between Large and Small Scales in Wall-Bounded Turbulent Flows," FED-Vol. 162, ASME Fluids Engineering Conference, pp 21-28.

Herring, J.R., 1979, "Subgrid Scale Modelling - An Introduction and Overview", *Turbulent Shear Flows I, Spring*er-Verlag, pp. 347-352.

Ideriah, F. J. K., 1978, "On Turbulent Forced Convection in a Square Cavity", Numerical Methods in Laminar/Turbulent Flow, Proceedings 1st International Conference., pp. 257-269.

Issa, R.I., "Solution of the Implicitly Discretised fluid Flow Equations by Operator-Splitting," *Journal of Computational Physics*, Vol. 62, 1985, pp 40-65.

Jordan, S. A., 1992, "An Iterative Scheme for Numerical Solution of Steady Incompressible Viscous Flows," *Computer and Fluids*, Vol. 21, No. 4, pp. 503-517.

Jordan, S. A. and Ragab, S. A., 1994, "An Efficient Fractional-Step Technique for Unsteady Three-Dimensional Flows," *Journal of Computational Physics*, (in review).

Jordan, S.A. and Spaulding, M.L., 1993, "A Fast Algorithm for Grid Generation," *Journal of Computational Physics*, Vol. 104, No.1, pp. 118-128.

Jovic, S. and Driver, M., 1992, NASA Ames Research Center, Moffett Field, CA, Unpublished.

Karniadakis, G.E., Orszag, S.A. and Yakhot, V., 1990, "Large-Eddy Simulation of Flow Over a Backward-Facing Step", *Engineering Turbulence Modeling and Experiments*, Elsevier, NY, pp 269-278.

Kato, C., Iida, A., Takano, Y. Fujita, H. and Ikegawa, M., 1993, "Numerical Prediction of Aerodynamic Noise Radiated from Low Mach Number Turbulent Wake," *AIAA 93-0145*.

Kim, J., and Moin, P., 1981, "Large Eddy Simulation of Turbulent Channel Flow", *Journal of Fluid Mechanics*, 1981.

Kim, J. and Moin, P., 1985, "Application of a Fractional-Step Method to Incompressible Navier-Stokes Equations," *Journal of Computational Physics*, Vol. 59, pp. 308-310.

Koseff, J. R. and Street, R. L., 1984a, "Visualization Studies of a Shear Three-Dimensional Recirculating Flow," *Journal of Fluids Engineering*, Vol. 106, No. 1, pp. 21-29.

Koseff, J. R. and Street, R. L., 1984b, "On End Wall Effects in a Lid-Driven Cavity Flow," *Journal of Fluids Engineering*, Vol. 106, No. 1, 1984, pp. 385-389.

Koseff, J. R. and Street, R. L., 1984c, "The Lid-Driven Cavity Flow: A Synthesis of Qualitative and Quantitative Observations," *Journal of Fluids Engineering*, Vol. 106, No. 1, pp. 390-398.

Leonard, A., 1974, "Energy Cascade in Large-Eddy Simulations of Turbulent Fluid Flows", *Advanced Geophysics*, Vol. 18A, pp. 237-248.

Lilly, D.K., 1992, "A Proposed Modification of the Germano Subgrid-Scale Closure Method," *Physics of Fluids*, A. 4, pp. 633-635.

Love, M.D. and Leslie, D.C., 1979, "Studies of Subgrid Modelling with Classical Closures and Burgers Equation", *Turbulent Shear Flows I*, Springer-Verlag, pp. 352-369.

Maliska, C.R. and Raithby, G.D., 1984, "A Method for Computing Three Dimensional Flows Using Non-Orthongonal Boundary-Fitted Coordinates," *International Journal of Numerical Methods in Fluids*,,Vol 4, pp. 519-537.

Mansour, N.N., Moin, J., Reynolds, W.C. and Ferziger, J.H., 1979, "Improved Methods for Large Eddy Simulation of Turbulence", *Turbulent Shear Flows I*, Springer-Verlag, pp. 386-400.

Metais, O. and Lesieur, M., 1989, "Large Eddy Simulation of Istropic and Stably-Stratified Turbulence", *Advances in Turbulence* 2, Springer-Verlag, pp. 370-376.

Moin, R.D., Reynolds, W.C. and Ferziger, J,H., 1978, "Large Eddy Simulation of Incompressible Turbulent Channel Flow", Dept. Mechanics Engr., Stanford Univ., Report TF-20.

Moin, P. and Kim, J., 1980, "On the Numerical Solution of Time-Dependent Viscous Incompressible Fluid Flows Involving Solid Boundaries," *Journal of Computational Physics*, Vol. 35, pp. 381-392.

Moin, P. and Kim, J., 1982, "Numerical Investigation of Turbulent Channel Flow", *Journal of Fluid Mechanics.*, Vol. 118, pp. 341-377.

Morinishi, Y. and Kobayashi, T. 1990, "Large Eddy Simulation of Backward Facing Step", *Engineering Turbulent Modeling and Experiments*, Elsevier, NY, pp 279-286.

Norberg, C., 1992, "Pressure Forces on a Circular Cylinder in Cross Flow," *IUTAM Symposium on Bluff-Body Wakes, Dynamics and Instabilities*, ed. Eckelmann et al., Springer-Verlag, pp. 275-278.

Orszag, S.A. and Paters, A.T., 1984, "A Spectral Element Method for Fluid Dynamics; Laminar Flow in a Channel Expansion", *Journal of Computational Physics*, Vol. 54, pp. 468.

Patankar, S. V., 1980, "Numerical Heat Transfer and Fluid Flow," Hemisphere, Washington, DC.

Patanka, S.V., and Spalding, D.B., " A Calculation Procedure for Heat, Mass and Momentum Transfer in Three Dimensional Parabolic Flows", *International of Journal Heat Mass Transfer*, Vol. 15, 1972, pp. 1787-1806.

Pauley, L.L.. Moin, P. and Reynolds, W.C., 1990, "The Structure of Two-Dimensional Separation,"*Journal of Fluid Mechanics.*, Vol. 220, pp. 397-411.

Peterson, V.L., Kim, J., Holst, G.S., Deiwert, D., Cooper, M., Watson, A.B. and Bailey, F.R., 1989, "Supercomputer Requirements for Selected Disciplines Important to Aerospace," *Journal of IEEE.*

Piomelli, U., Cabot, W.H., Moin, P., Lee, S., 1991, "Subgrid Scale Backscatter in Turbulent and Transitional flows," *Physics of Fluids*, A. 3, pp. 1766-1771.

Piomelli, U., Ferziger, J. H. and Moin, P., 1988, "Model for Large Eddy Simulation of Turbulent Channel Flow Including Transpiration," Department of Mechanical Engineering Report, TF-32, Stanford U., Stanford, CA.

Prasad, A.K. and Koseff, J. R., 1989, "Reynolds Number and End-Wall Effects on a Lid-Driven Cavity Flow," *Physics of Fluids A*, Vol. 1, No. 2, pp. 208-218.

Prasad, A. K., Perng, C. Y., and Koseff, J. R., 1988, "Some Observations on the Influence of Longitudinal Vortices in a Lid-Driven Cavity Flow," AIAA/ASME/SIAM/APS 1st National Fluid Dynamics Congress, pp. 288-295.

Ragab, S.A. and Sheen, S., 1991, "Large-Eddy Simulation of a Mixing Layer", *AIAA* 91-0233.

Rai, M.M. and Moin, P.,1989, "Direct Simulations of Turbulent Flow Using Finite-Difference Schemes", *AIAA-89-0369.*

Reynolds, W.C., 1991, "The potential and limitations of direct and large eddy simulations", In Whither Turbulence, (ed. Lumley, J.L.), Springer-Verlag, NY.

Rogallo, R.S. and Moin, P., 1984, "Numerical simulation of turbulent flows", *Annual Review Fluid Mechanics*, No. 16, pp. 99-137.

Roshko, A., 1954, "On the Drag and Shedding Frequency of Two-Dimensional Bluff Bodies," NACA Report No. 1191.

Rhee, H. S., Koseff, J. R., and Street, R. L., 1984, "Flow Visualization of a Recirculating Flow by Rheoscopic Liquid and Liquid Crystal Techniques," *Experiments in Fluids*, Vol. 2, pp. 57-64.

Rhie, C.M. and Chow, C.L., 1982, "A Numerical Study of the Turbulent Flow Past an Isolated Airfoil with Trailing Edge Separation," AIAA 82-0998.

Schneider, G.E. and Zedan, M., (1981), "A modified semi-implicit procedure for the numerical solution of field problems", *Numerical Heat Transfer*, Vol. 4, pp 1-19.

Schumann, U., 1975, "Subgrid Scale Model for Finite Difference Simulation of Turbulent Flows in Plane Channel and Annuli", *Journal of Computational Physics*, No 18, pp. 376-404.

Schumann,U. and Krettenauer, K., (1990), "Numerical Simulation of Turbulent Convection Over Wavy Terrain," *Journal of Fluid Mechanics.*, Vol. 237, pp. 261-299.

Shao, L., Le Penven, L. and Bertoglio, J.P., (1990), "Study of the Modelling of the Transport Terms in One-Point Closures Using Large Eddy Simulation of Turbulence", *Engr. Turbulent Modeling* and *Experiments*, Elsevier, NY, pp 83-92.

Smagorinsky, J., 1963, "General Circulation Experiments with the Primitive Equations, I. The Basic Experiment," *Monthly Weather Review*, Vol. 91, pp. 99-164.

Soh, W. Y., and Goodrich, J. W., 1988, "Unsteady Solution of Incompressible Navier-Stokes Equations," *Journal of Computational Physics*, Vol. 79, pp. 113-134.

Song, C.C.S. and Yuan, M., 1990, "Simulation of Vortex-Shedding Flow About a Circular Cylinder at High Reynolds Number," *Journal of Fluids Engineering*, Vol. 112, pp. 155-163.

Speziale, C.G., 1985, "Galilean Invariance of Subgrid-Scale Stress Models", *Journal of Fluid Mechanics.*, Vol. 156, pp. 55-62.

Squires, K.D., 1993, "Large-Eddy Simulation of Rotating Isotropic Turbulence", FED-Vol. 162, ASME Fluids Engineering Conference., pp. 65-72.

Stone, H.L., 1968, "Iterative Solution of Implicit Approximation of Multi-Dimensional Partial Differential Equations", SIAM J. *Numerical Analysis* Vol. 5, pp. 530-558.

Taylor, G. I., 1923, "Stability of Viscous Liquid Contained Between Two Rotating Cylinders," *Philosophical Transaction of the Royal Society* (London), Vol. 223, pp. 289-343.

Taylor, L.K., 1991, "Unsteady Three-Dimensional Incompressible Algorithm Based on Artifical Compresibility," *Dissertation*, Mississippi State, MS.

Telionis, D.P., 1981, "Unsteady Viscous Flow", Springer-Verlag, NY, NY.

Tritton, D.J., 1959, "Experiments on the Flow Past a Circular Cylinder at Low Reynolds Numbers," *Journal of Fluid Mechanics*, Vol. 6, pp. 547.

Van Driest, E. R., 1956, "On the Turbulent Flow Near a Wall," *Journal of Aeronautical Sciences*, No. 23, pp. 1007-1012.

Wanik, A. and Schnell, U., 1989,"Some Remarks on the PISO and SIMPLE Algorithms for Steady Turbulent Flow Problems," *Computers and Fluids*, Vol. 17, No. 4, pp. 555-570.

Werner, H. and Wengle H., 1989, "Large-Eddy Simulation of Turbulent Flow Over a Square Rib in a Channel", *Advances in Turbulence* 2, Springer-Verlag, pp. 418-424.

Yakhot, V. and Orszag, S.A., 1986, "Renormalization Group Analysis of Turbulence I. Basic Theory", *Journal of Scientific Computing*, Vol. 1, pp. 3.

Young, D. L., Liggett, J. A., and Gallagher, R. H., 1976, "Unsteady Stratified Circulation in a Cavity," *Journal of Engineering Mechanics Divison*, ASCE 102, EM6, pp. 1009-1023.

Zang, T.A. and Piomelli U., 1990, "Large Eddy Simulation of Transition Flow", *Instability and Transition*, Springer-Verlag, Vol. 2, pp. 1-17.

Zang, Y., Street, R.L. and Koseff, J.R., 1993, "A Dynamic Mixed Subgrid-Scale Model and Its Application to Turbulent Recirculation Flows, *Physics of Fluids*, Vol. 5, No. 12, pp. 3186-3196.

Zhou Y. and Antonia, R.A., 1993, "A Study of Turbulent Vortices in the Near Wake of a Cylinder," *Journal of Fluid Mechanics*, Vol. 253, pp. 643-661.

Table 7.1: Comparisons of Lift (C_L) and Drag (C_D) Coefficients and Strouhal Number (S_t) for Cross Flow Over a Circular Cylinder at Re = 200.

Reference	C_D	C_L	S_t
Gerrard (1978) Experiment			0.18 - 0.20
Wille (1960) Experiment	1.3		
Lecointe & Piquet (1984)	1.46	0.70	0.23
Rosenfeld, Kwak & Vinokur (1993)	1.31	0.65	0.20
Present	1.43	0.68	0.205

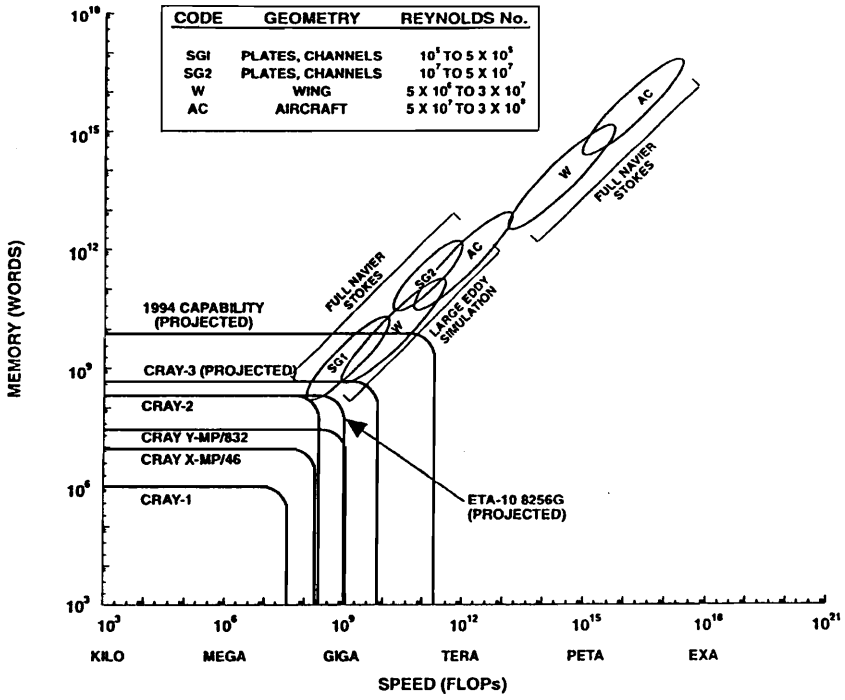

Figure 1.1. Projected Use of Simulations in Turbulence Physics (Peterson et al., 1989).

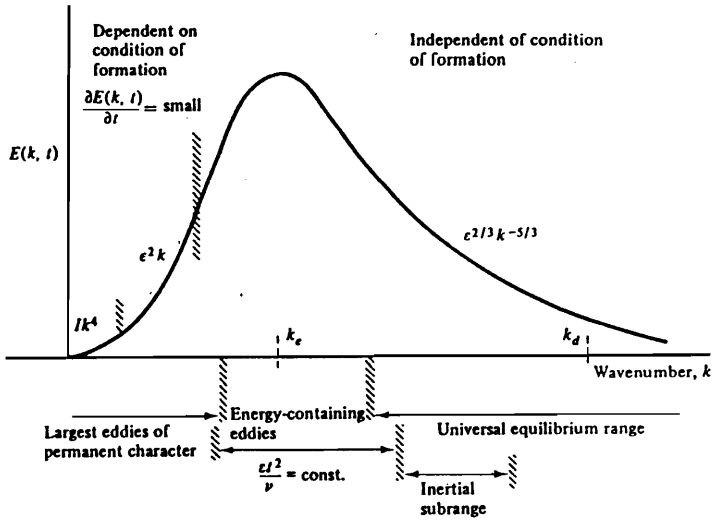

RANS|<---------- Fully Modelled ---------->>
DNS|<---------- Fully Resolved ---------->>
LES|<-------- Resolved ------->|<----- Modelled ----->>

Figure 1.2. Energy Spectra of Homogeneous, Isotropic Turbulence (Hinze, 1975).

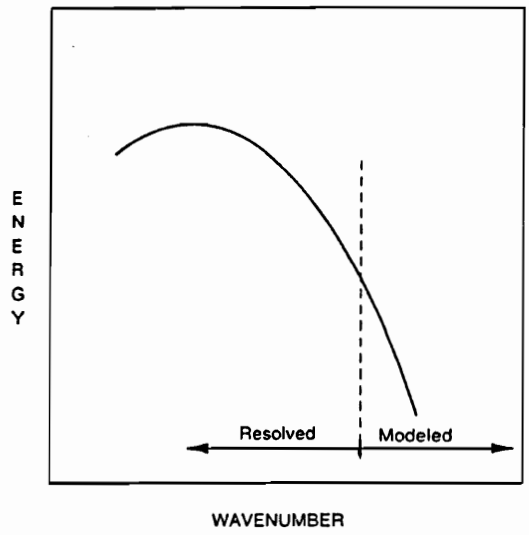

Figure 2.1. Division of Resolved and Model Fields in Wavenumber Space by the Filter Used in the Large-Eddy Simulation Methodology.

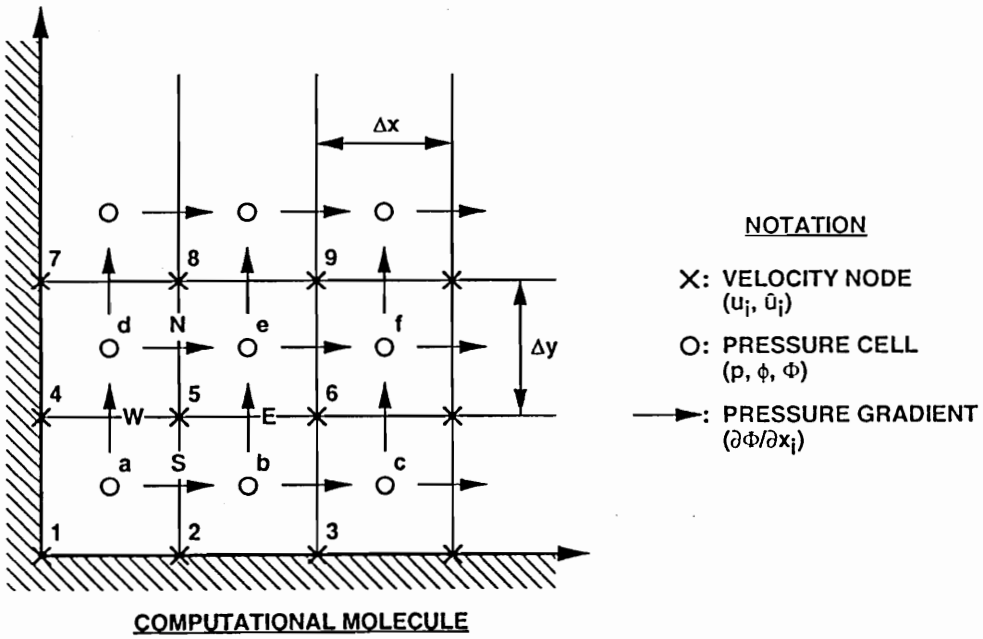

Figure 2.2. Computational Molecule Used for Discretizing the Incompressible Navier-Stokes Equations.

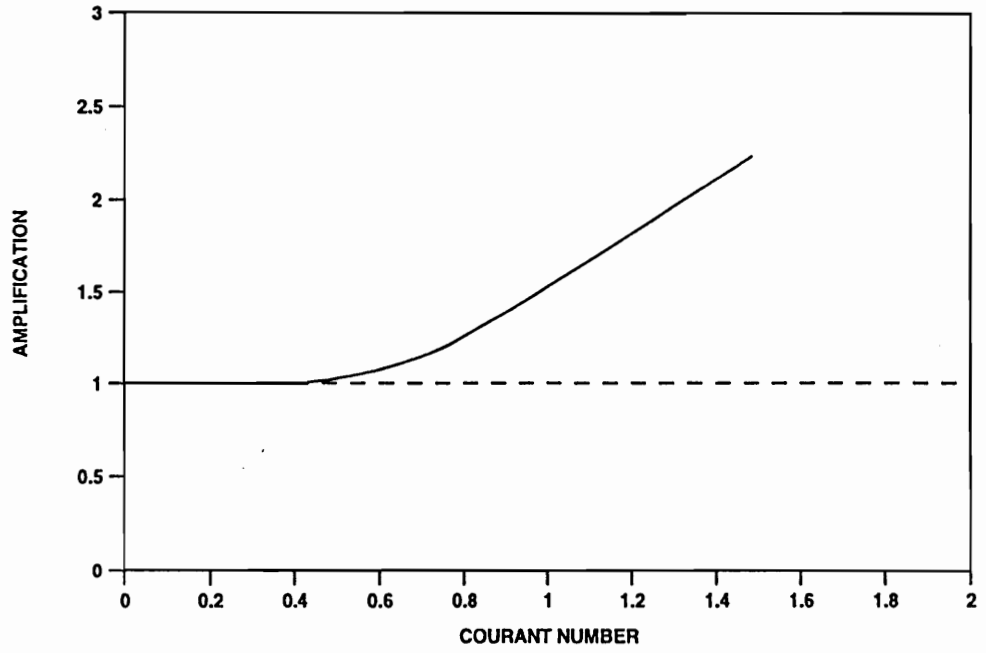

Figure 2.3. ***Numerical Stability of the Adams-Bashforth Method Applied to the Linear Convection Equation.***

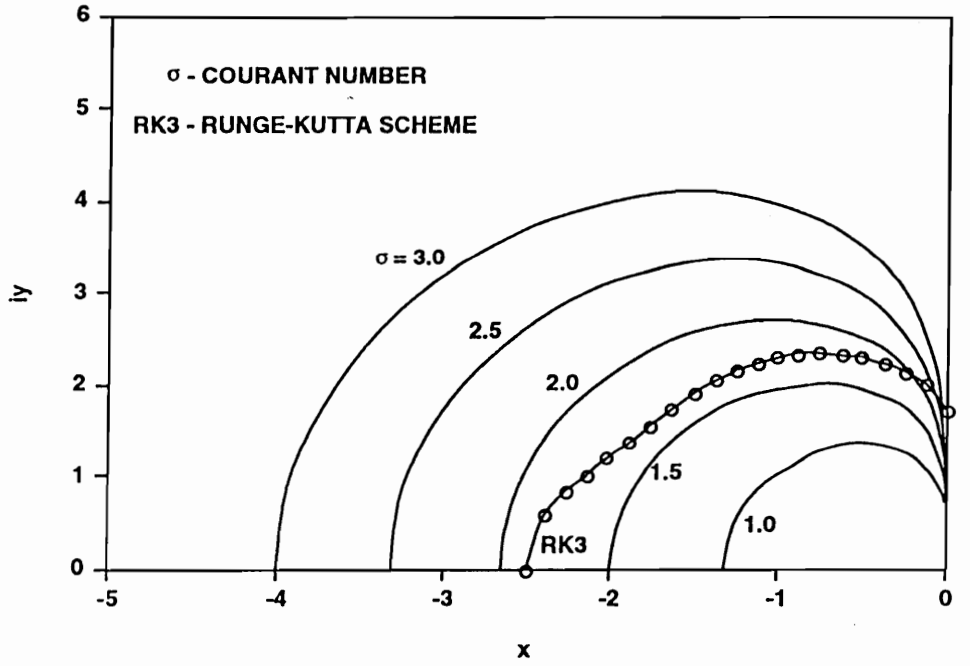

Figure 2.4. ***Numerical Stability of the Linear Convection Equation Using the Third-Order-Accurate, Three-Step, Runge-Kutta Procedure and Third-Order-Accurate, Upwind-Biased Spatial Differences.***

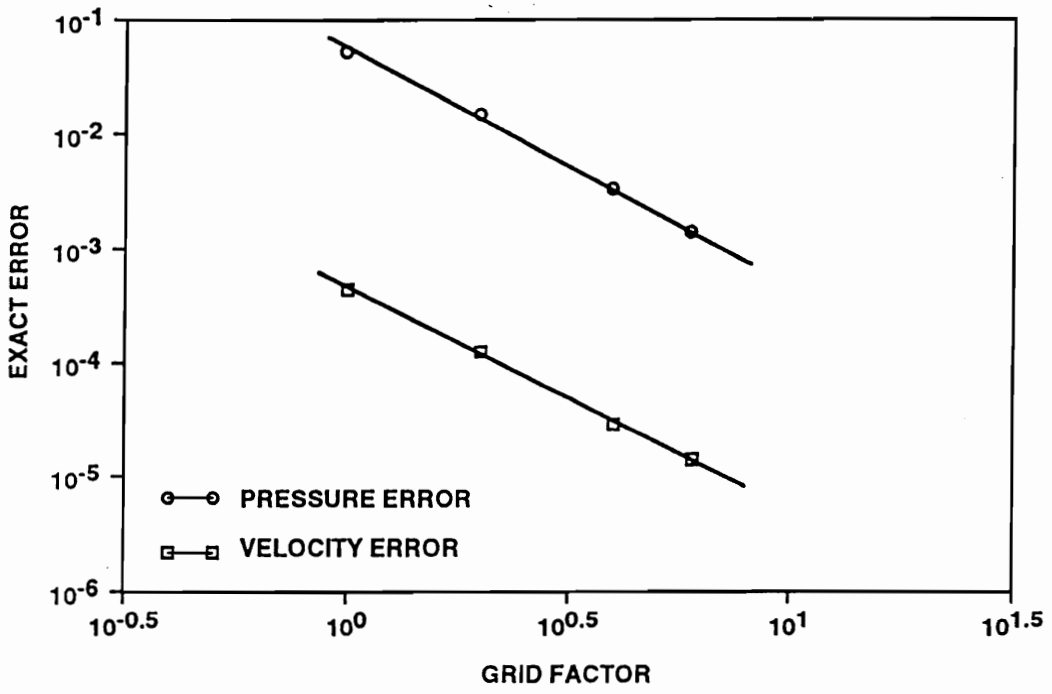

Figure 2.5. Improvement in the Exact Errors of Velocity and Pressure with Grid Refinement for a Constant Courant Number.

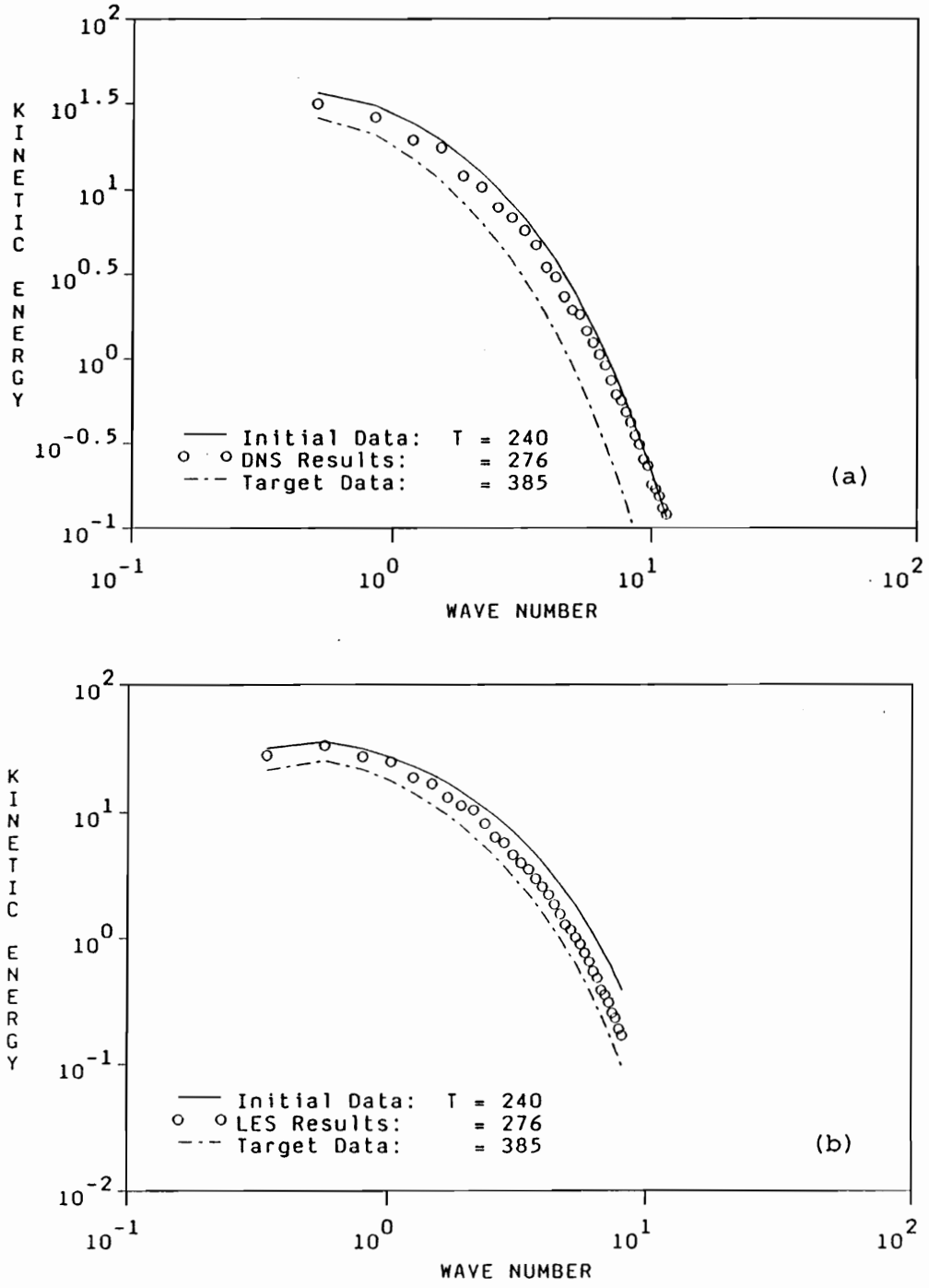

Figure 5.1. Comparisons of the Experimental Data (Comte-Bellot and Corrsin, 1971) and (a) DNS and (b) LES Results for the Decay of Isotropic Turbulence.

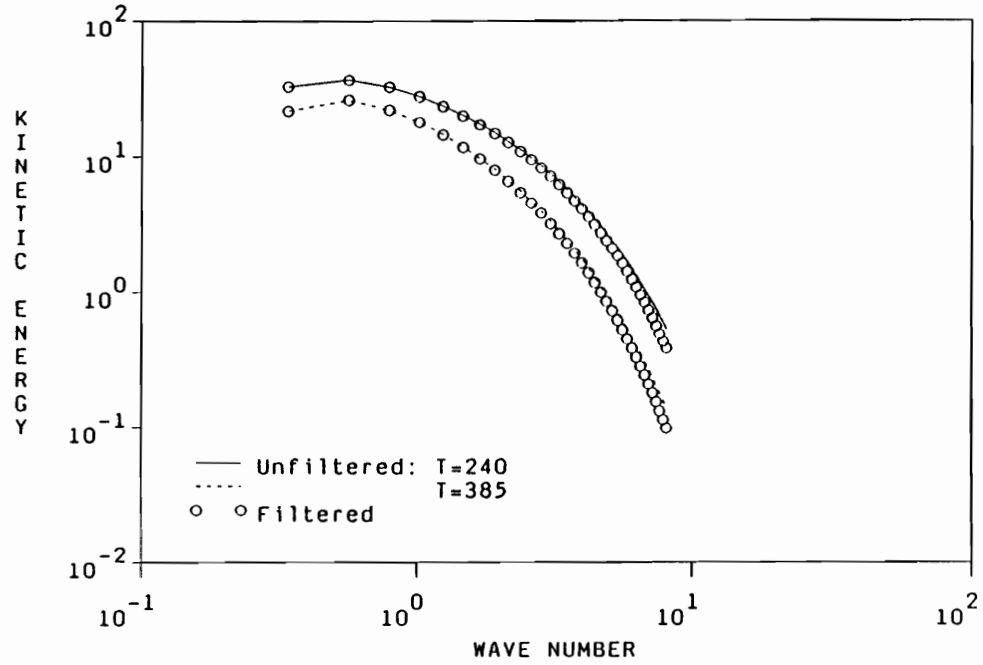

Figure 5.2. ***Attenuation of Turbulent Energy Spectra Due to Second-Order Central Differencing of the Convective Terms in the LES Equations.***

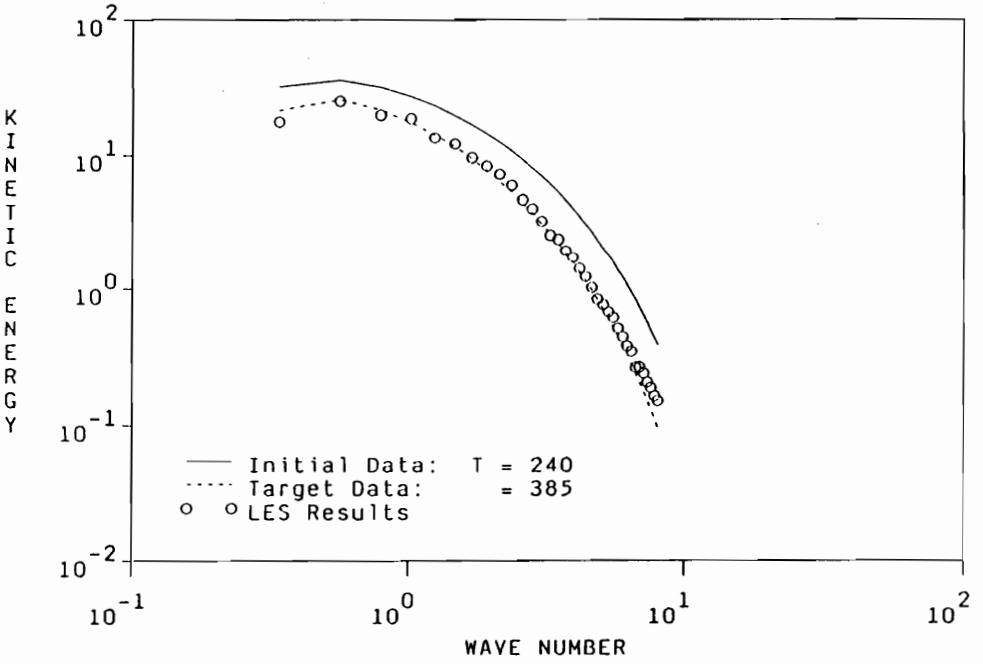

Figure 5.3. ***Comparisons of the Experimental Data (Comte-Bellot and Corrsin, 1971) and LES Results for the Decay of Isotropic Turbulence.***

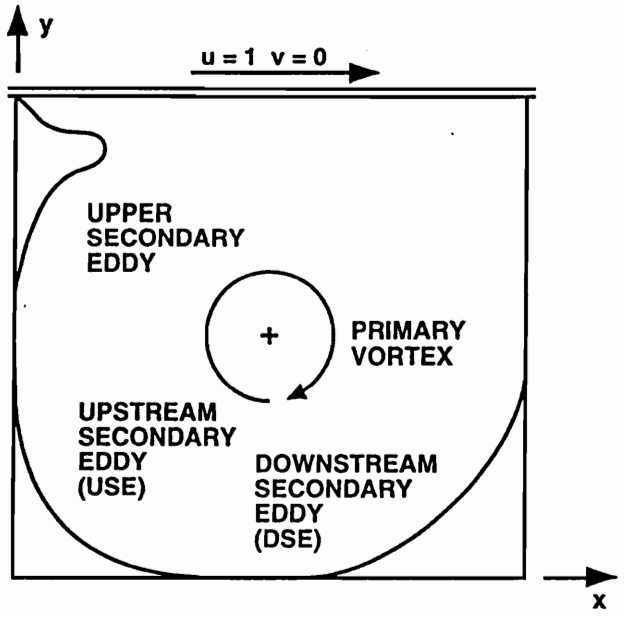

Figure 6.1. ***Sketch of the Basic Features of Recirculation in the Two-Dimensional Shear-Driven Cavity Flow Problem.***

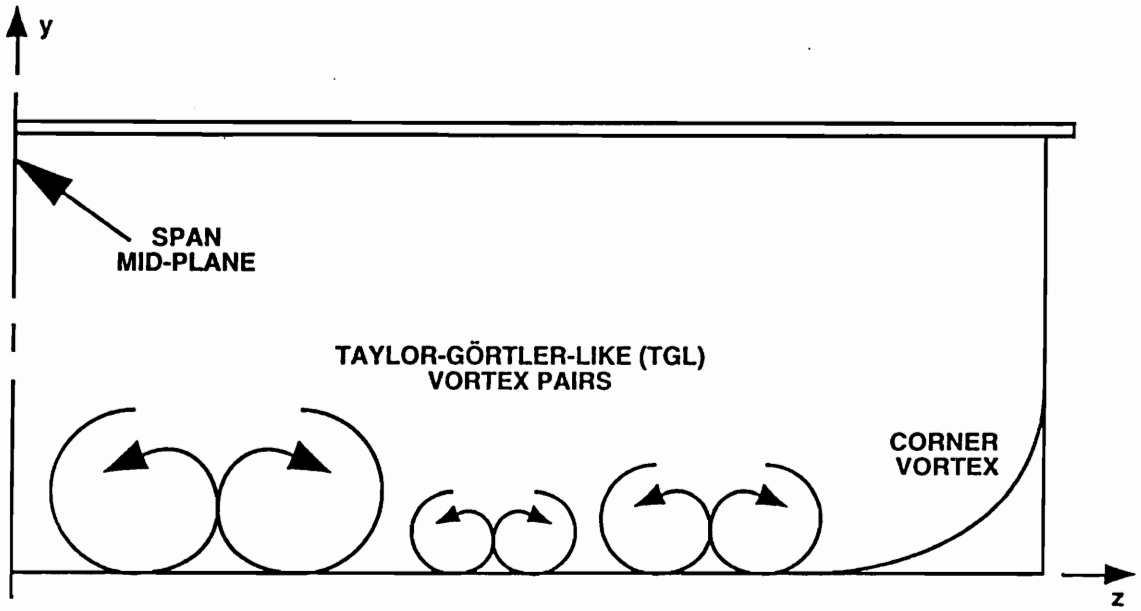

Figure 6.2. ***Sketch of the Taylor-Gortler-Like (TGL) Vortex Pairs as Observed in the Flow Visualization Experiments.***

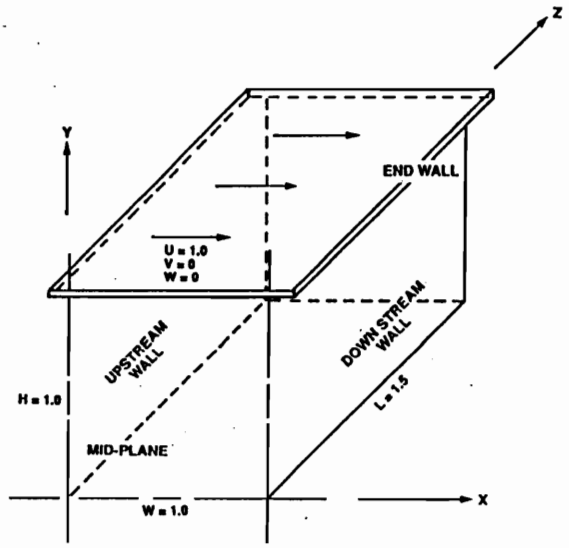

Figure 6.3. ***Model Problem for DNS and LES Predictions of the Shear-Driven Cavity Flow with Spanwise Aspect Ratio SAR = 3.0.***

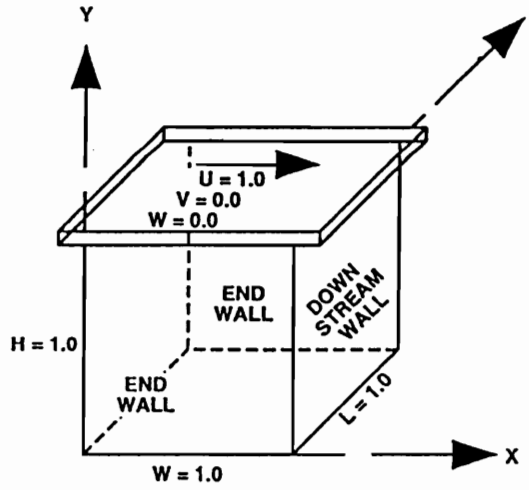

Figure 6.4. ***Model Problem for DNS and LES Predictions of the Shear-Driven Cavity Flow with Spanwise Aspect Ratio SAR = 1.0.***

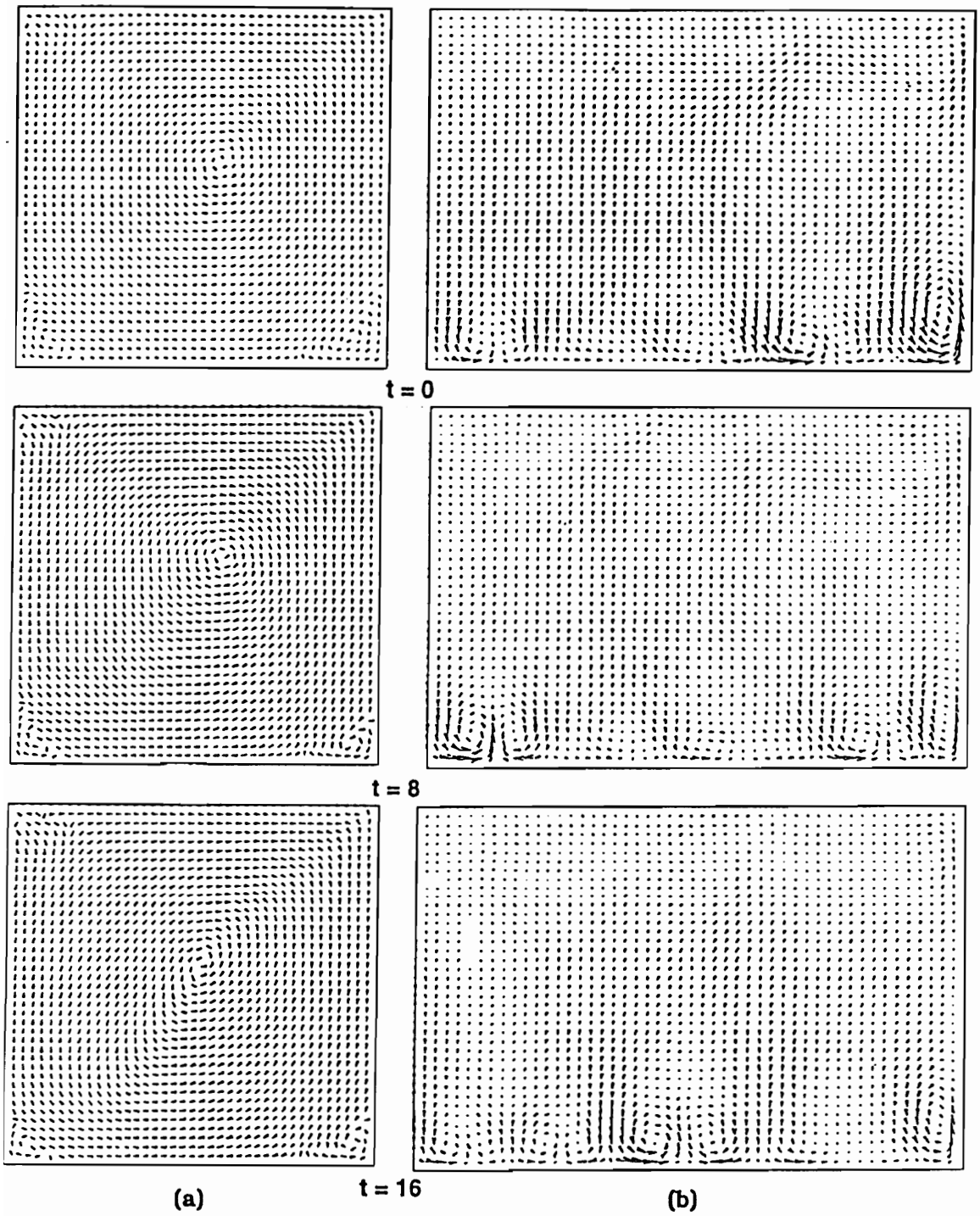

Figure 6.5. Snapshots of the Recirculation (a) and Spanwise flow (b) at Times T_f = 0.0, 8.0, 16.0 for Re = 2000. Recirculation Vectors Shown at the cavity Mid-Span. Spanwise Flow Shown at Plane X = 0.77.

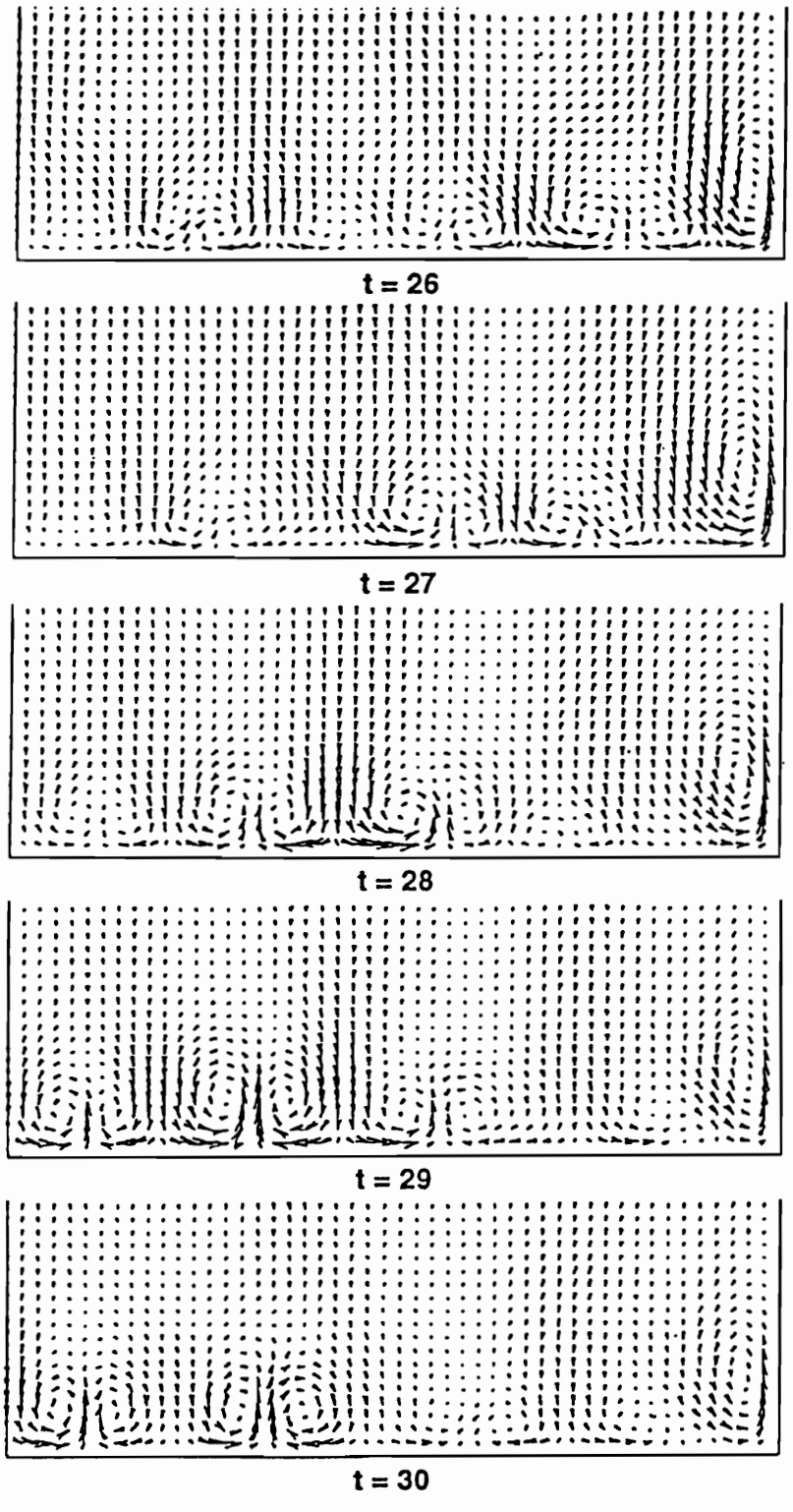

Figure 6.6. Snapshots of the Spanwise flow Showing Meander and Physical Size of TGL Vortices for Re = 2000.

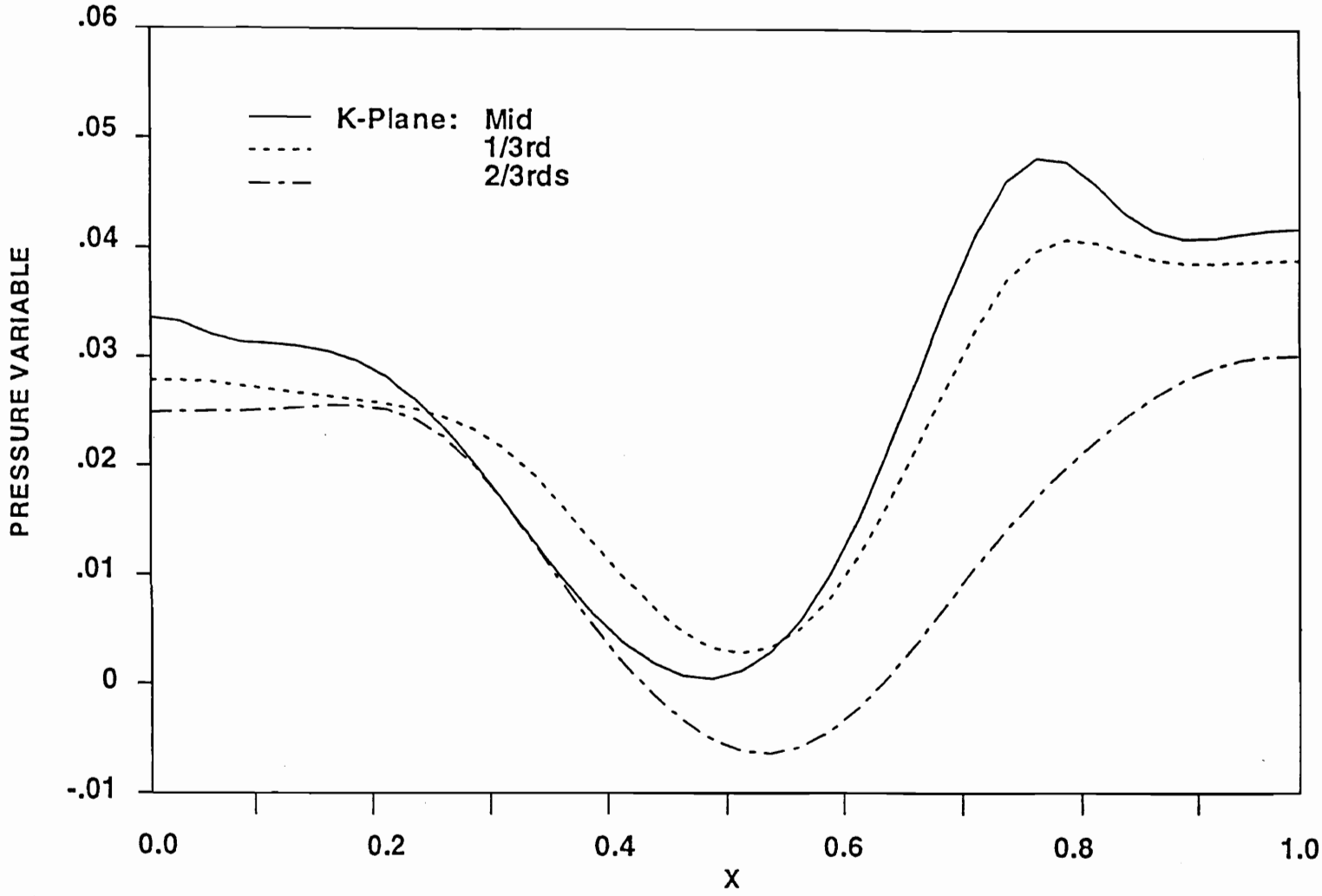

Figure 6.7. Pressure Variable Profiles at Y = 0.1 from the Upstream (x = 0.0) to the Downstream Wall (x = 1.0) at the Mid, 1/3rd and 2/3rds Planes in the Z Direction.

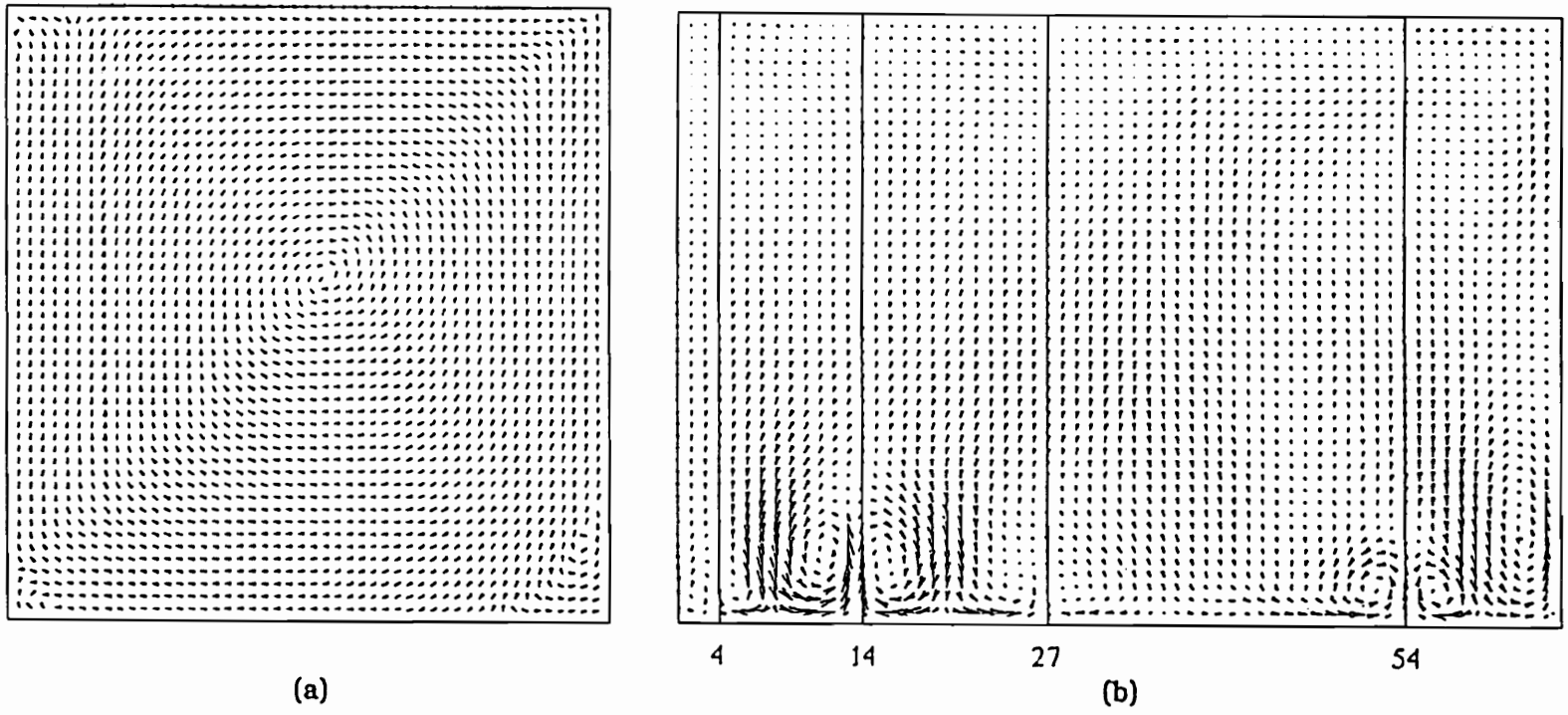

Figure 6.8. *Snapshots of the Recirculation (a) and Spanwise flow (b) at Time T_f = 12.0 for Re = 3200. Recirculation Vectors Shown at the cavity Mid-Span. Spanwise Flow Shown at Plane X = 0.77.*

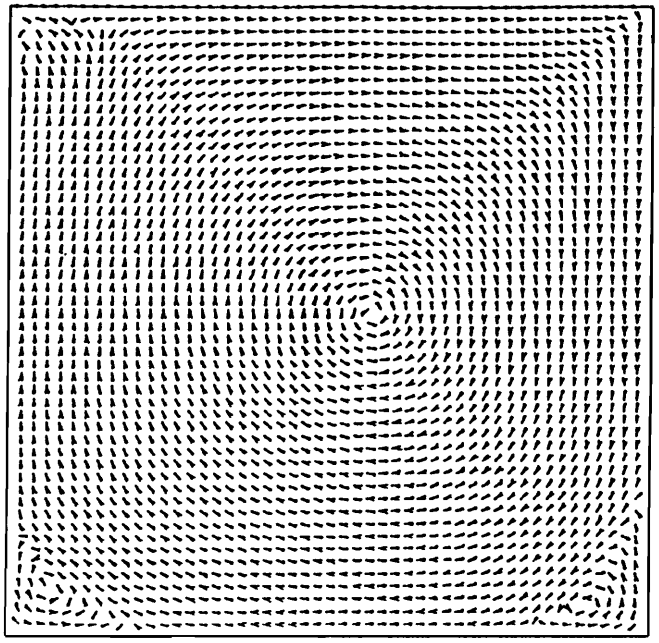

(a)

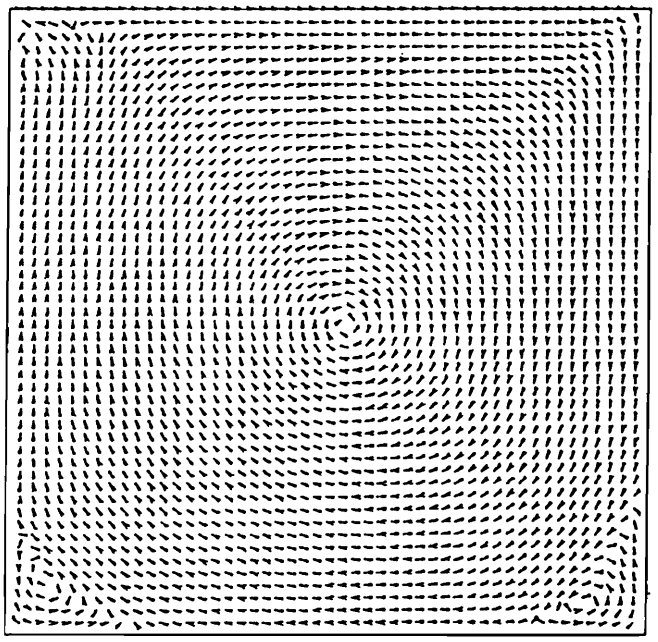

(b)

Figure 6.9. Recirculation Velocity Vectors Representing T_f = 1080 Sample Averages of the Shear-Driven Cavity flow at Re = 3200; (a) 1/3rd and (b) 2/3rds Planes from the Cavity Spanwise End-Wall.

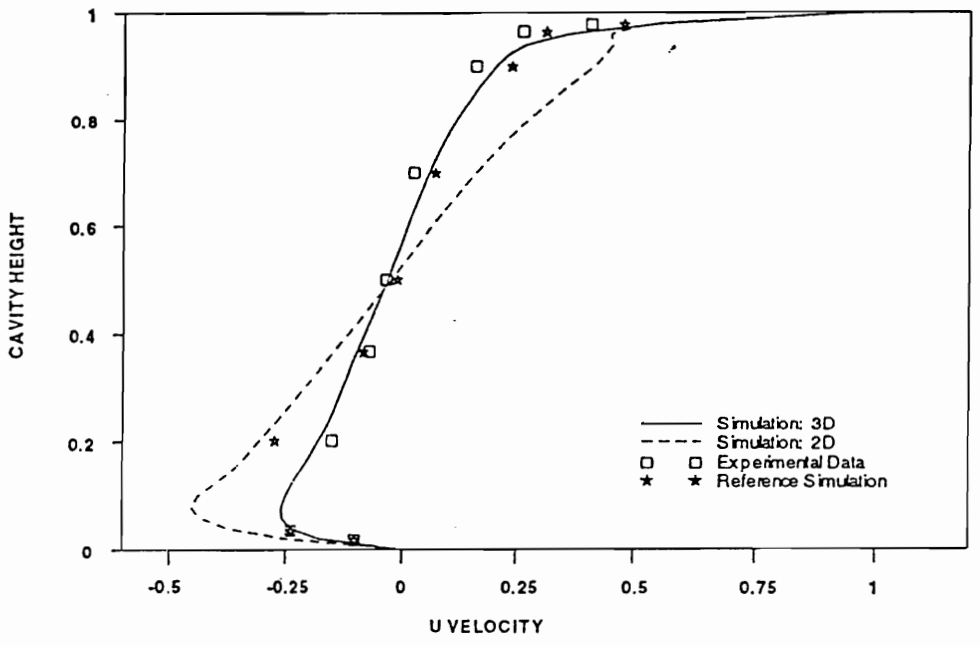

(a)

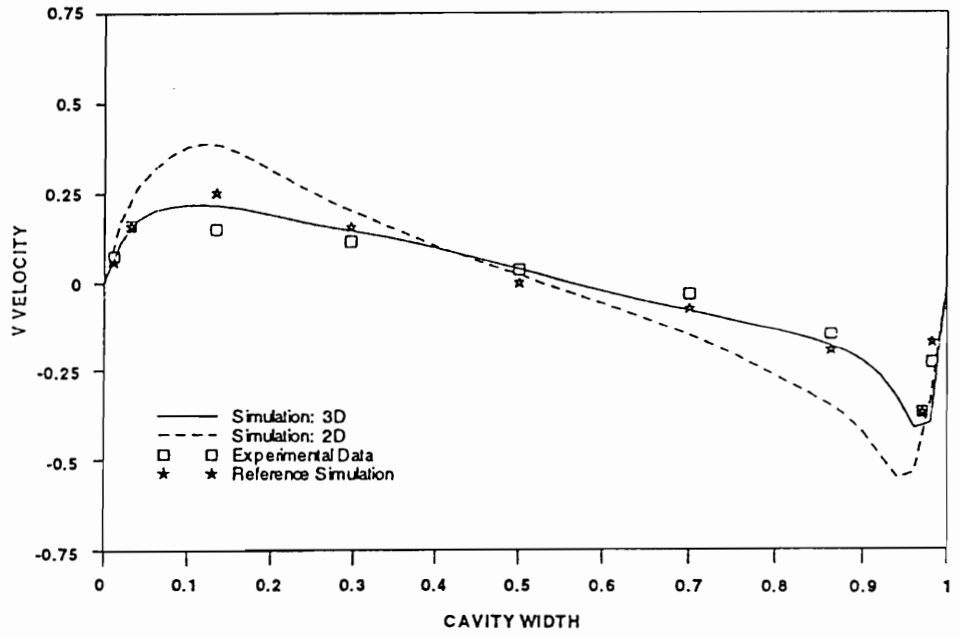

(b)

Figure 6.10. Comparison of Experimental and Computational Time-Averaged Velocity Profiles Through the Cavity center at the Mid-Span for Re = 3200. Experimental Data Taken from Koseff and Street (1984a) and Reference Simulation for Freitas et al. (1985); (a) U-Velocity, (b) V-Velocity.

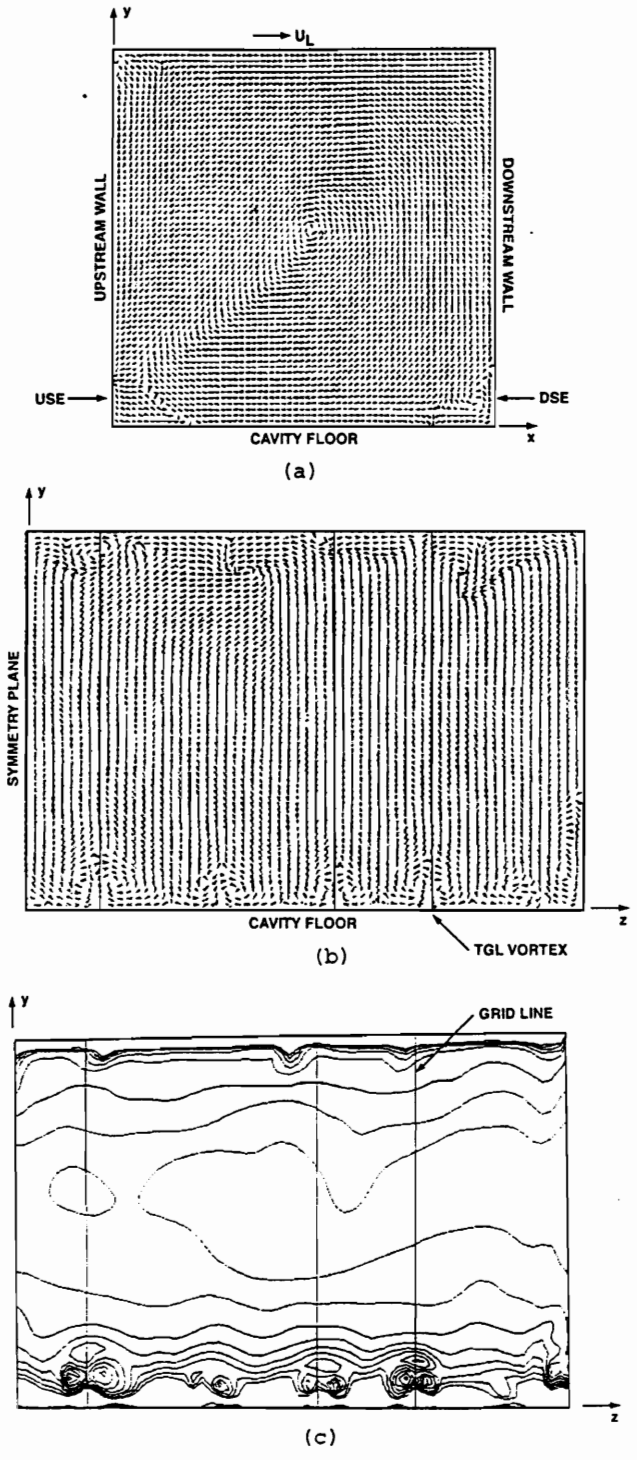

Figure 6.11. Snapshots of the Unsteady Velocity Vectors in the Shear-Driven Cavity Flow at Time T_f = 15.0; (a) Recirculation at Mid-Span Symmetry Plane, (b) TGL Vortices at Plane x = 0.77 and (c) Spanwise Static Pressure Contours; Re = 5000 and SAR = 3.0

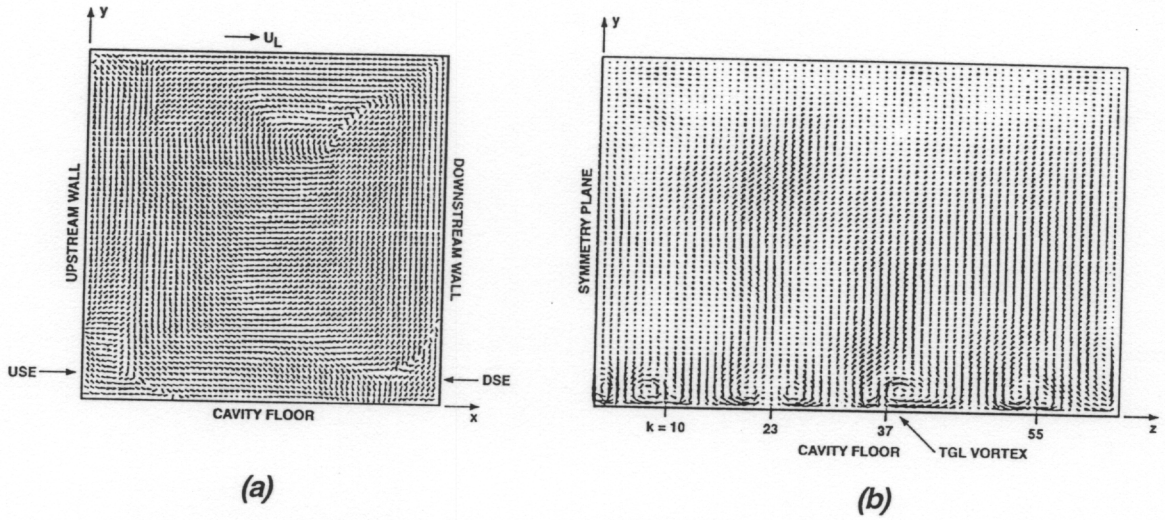

Figure 6.12. Snapshots of the Unsteady Velocity Vectors in the Shear-Driven Cavity Flow at Relative Time T_r = 181.0; (a) Recirculation at Mid-Span Symmetry Plane and (b) TGL Vortices at Plane x = 0.77.

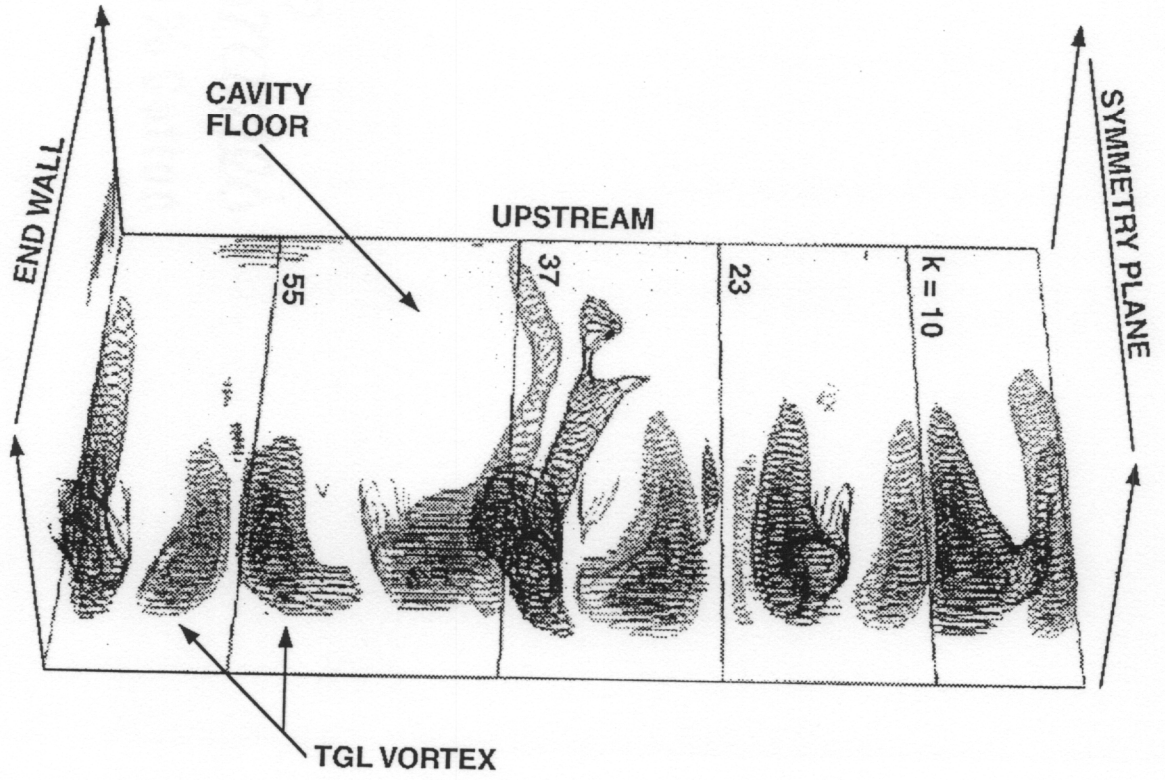

Figure 6.13. Spanwise Distribution and Streamwise Extent of TGL Vortex Contours at Completion of DNS Computation (T_r = 181.0).

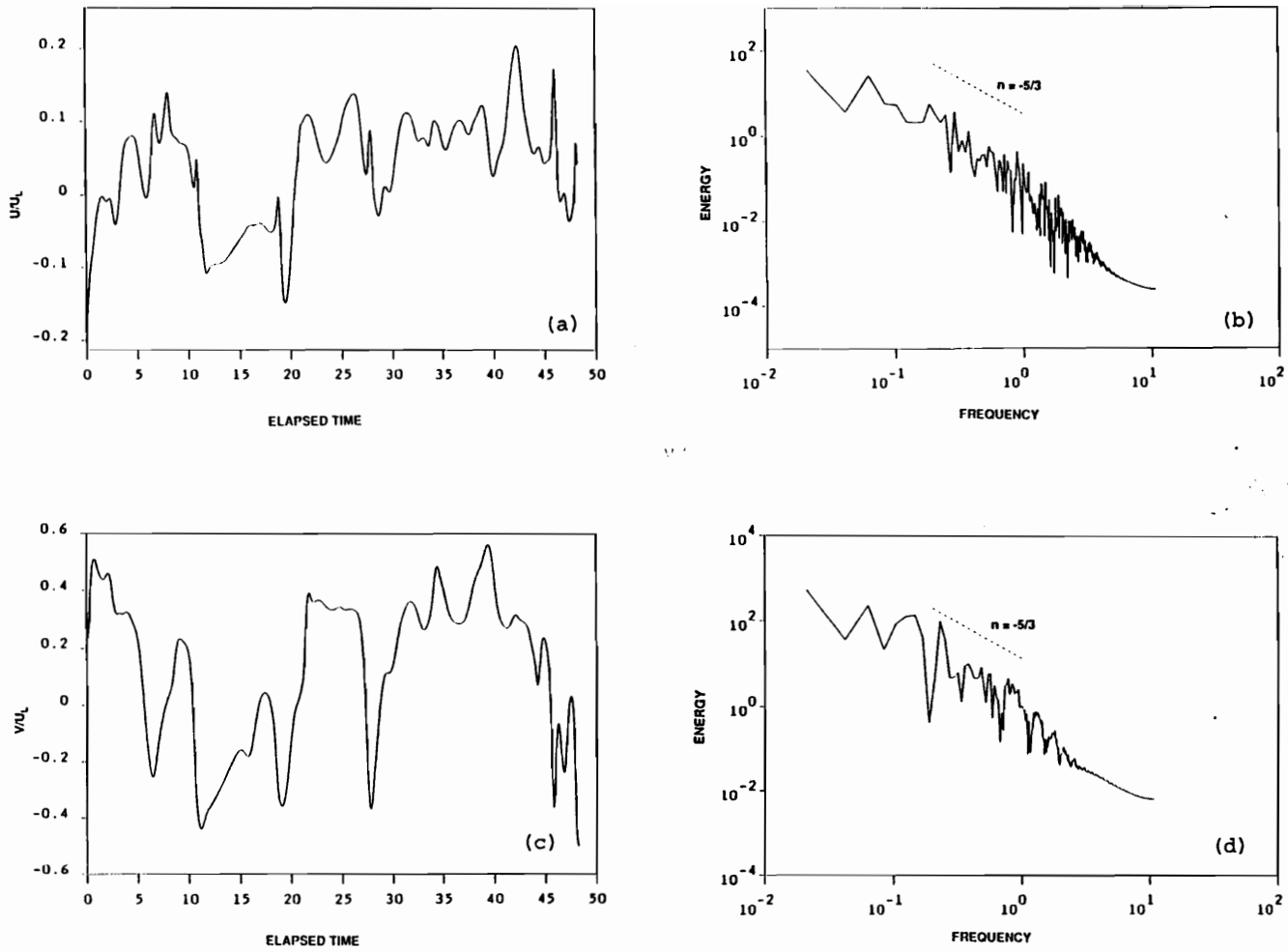

Figure 6.14. Time Traces (a) and (c) and Power Spectra (b) and (d) of Horizontal and Vertical Velocity Components Near the Downstream Free Shear Layer for Test Case Re = 5000.

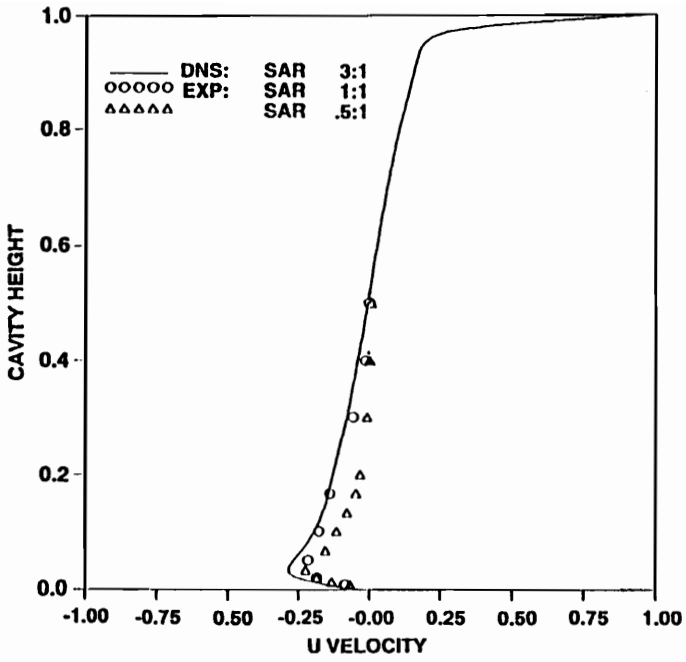

Figure 6.15. Quantitative Comparisons Between the DNS Results and Experimental Data (Prasad and Koseff, 1989) in Terms of the Center-Line Mean Velocities at the Cavity Mid-Span Plane; Re = 5000.

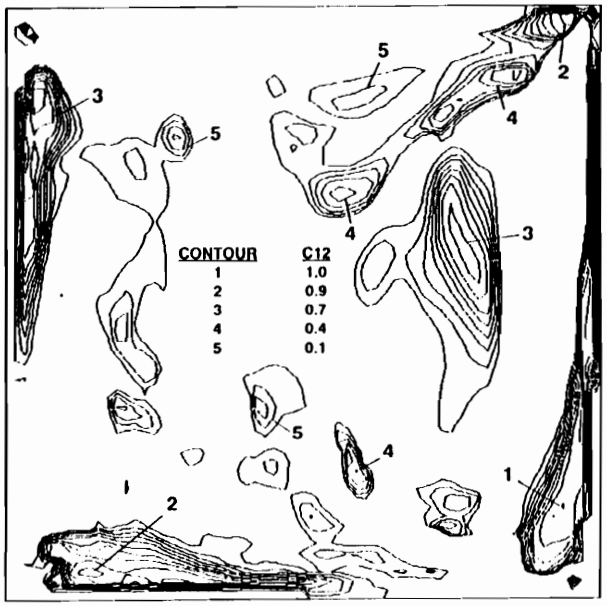

Figure 6.16. Distribution of Correlation Coefficient C_{12} Using Damping Parameters m = 8.0 and n = 0.14 and Smagorinsky Constant C_S = 0.1 in Turbulence Length Scale Definition. Correlation Computed from DNS Data Taken at Completion of Test Case Re = 5000 (T_f = 181.0).

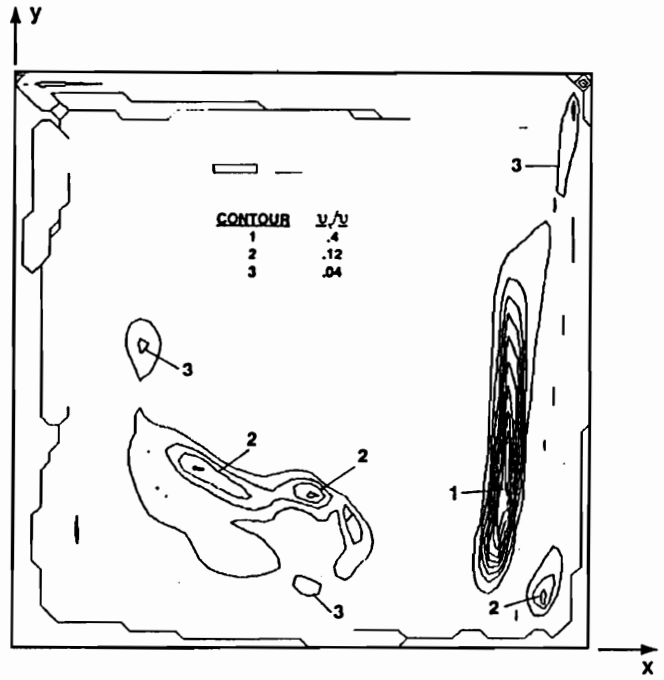

(a)

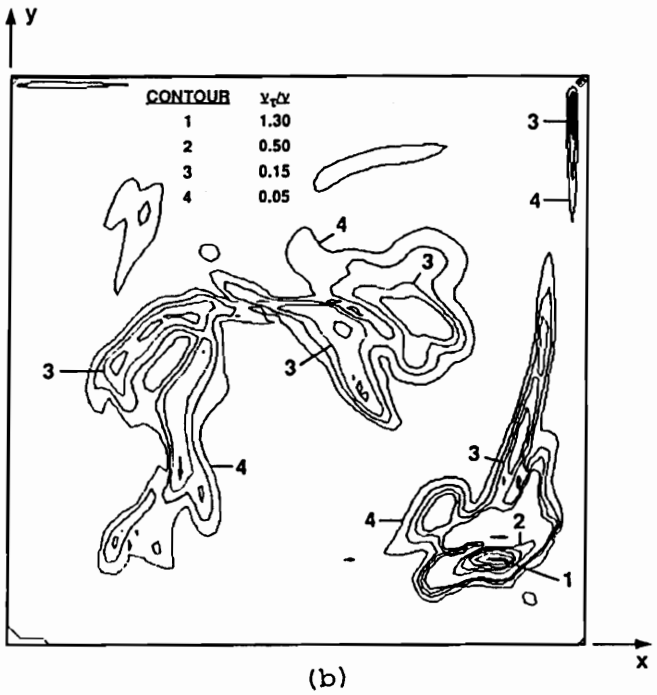

(b)

Figure 6.17. Turbulent Eddy Viscosity Levels (normalized by the kinematic viscosity) Computed from DNS Data Taken at Completion of Simulation; (a) Re = 5000 and (b) Re = 7500.

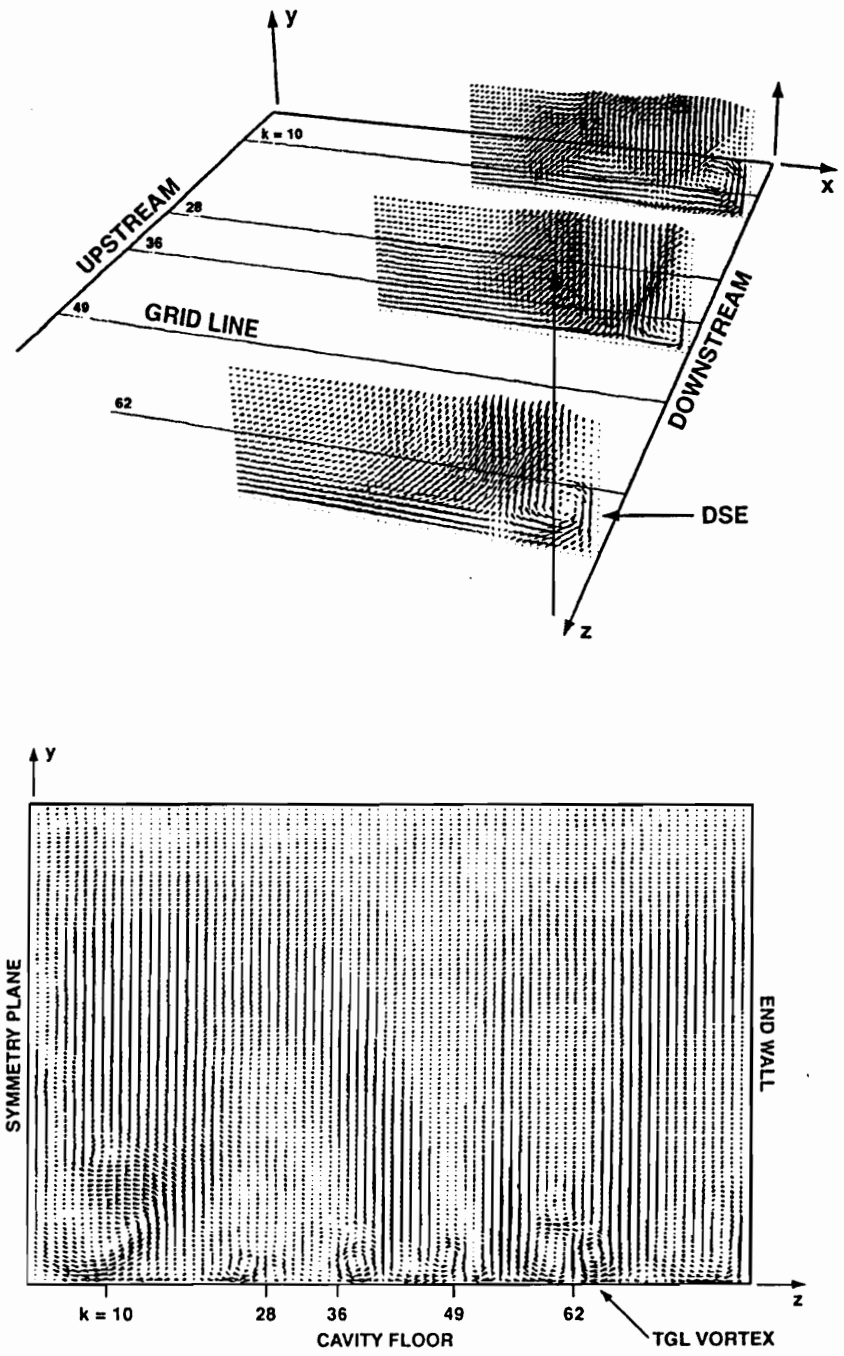

Figure 6.18. Velocity Vectors Illustrating (a) Regions of the Downstream Secondary Eddy and (b) TGL and Corner Vortices for LES Test Case Re = 10000 at Relative Time T_f = 6.5.

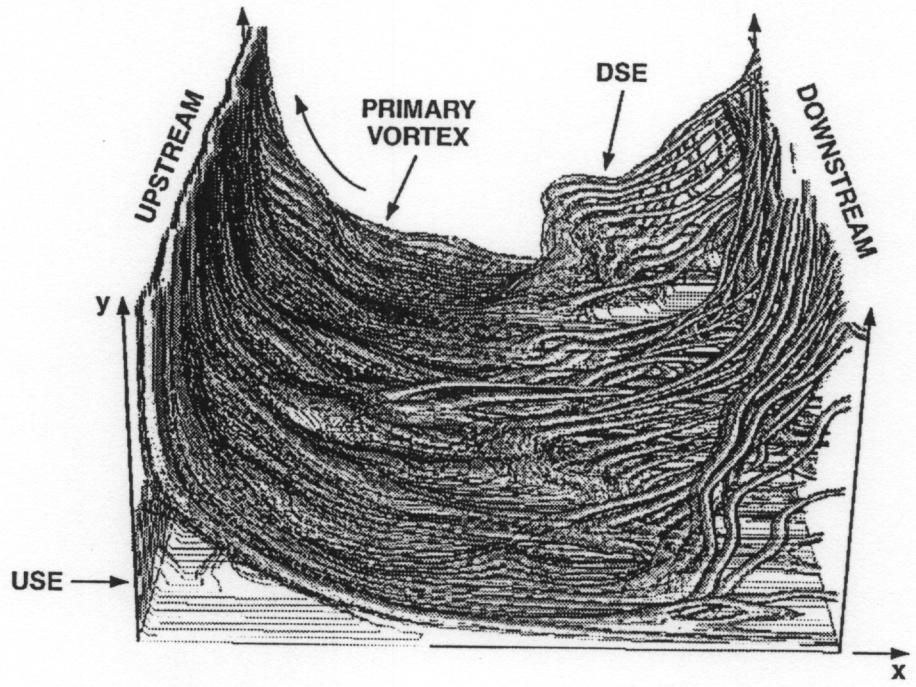

Figure 6.19. Stream Function Contours Showing the Downstream and Upstream Secondary Eddies in the LES Computation of the Shear-Driven Cavity Flow at Re = 10000 and Relative Time T_r = 6.5.

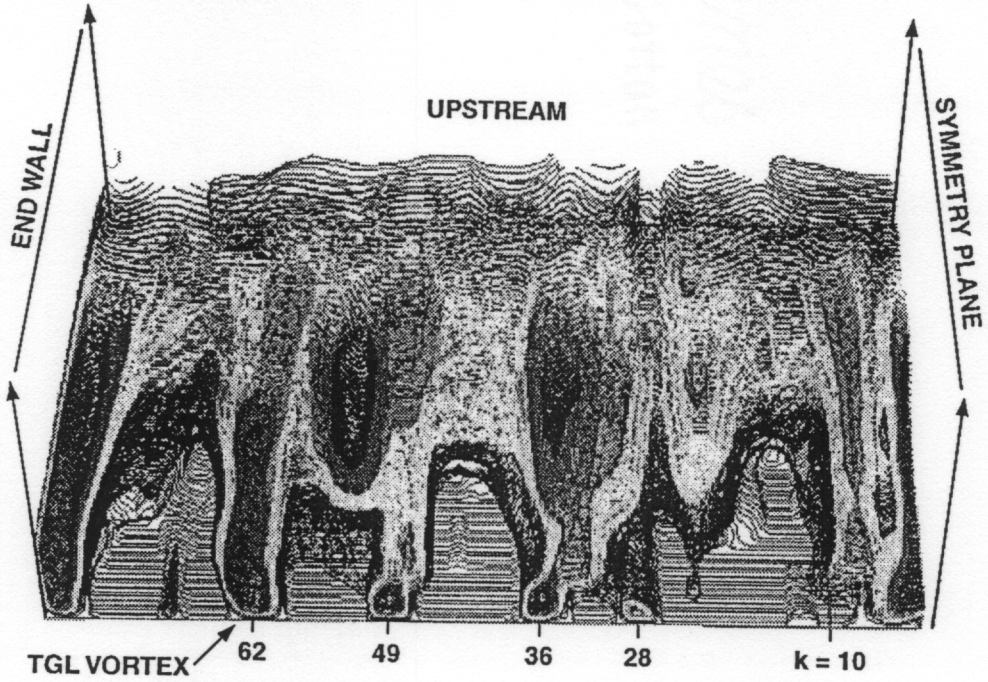

Figure 6.20. Stream Function Contours Showing the TGL and Corner Vortices in the LES Computation of the Shear-Driven Cavity Flow at Re = 10000 and Relative Time T_r = 6.5.

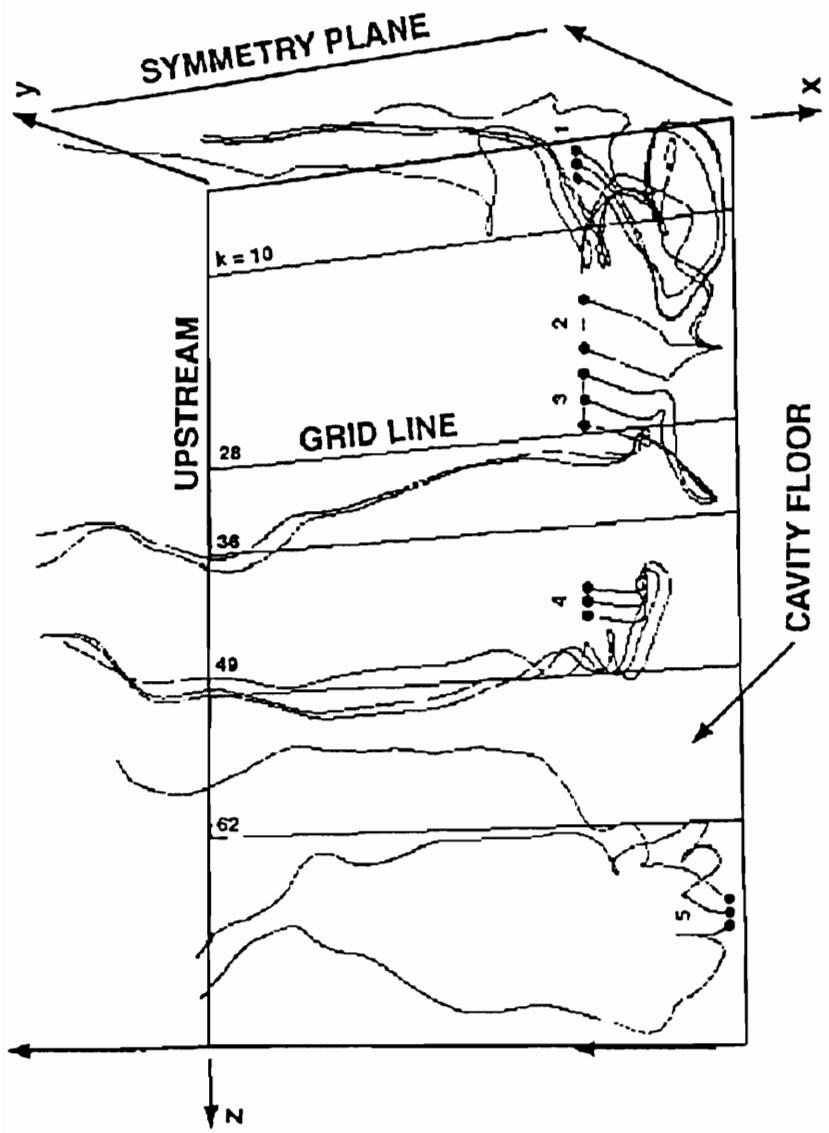

Figure 6.21. Five Sets of Particle Traces Illustrating the Interaction Among the Primary Recirculation Vortex, Downstream Secondary Eddy and TGL and Corner Vortices of the LES Computation at Relative Time $T_r = 6.5$.

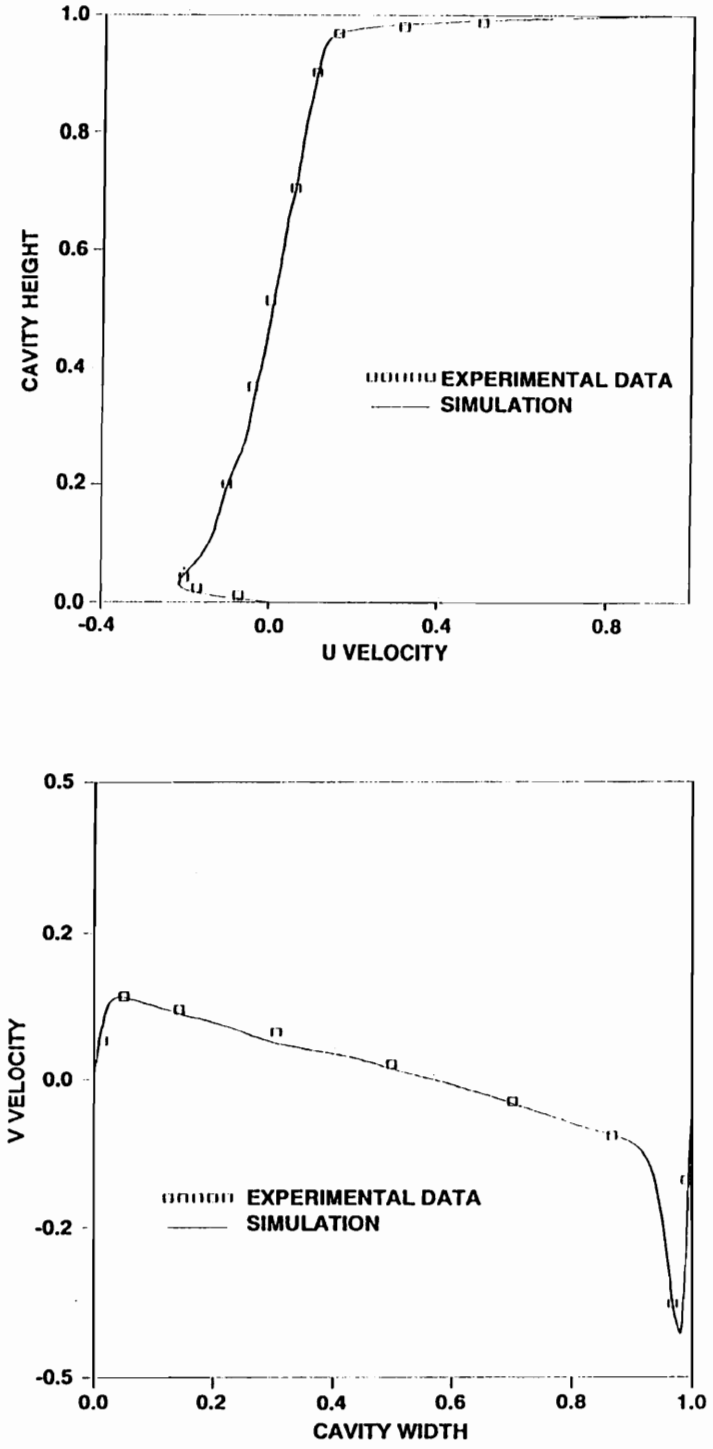

Figure 6.22. Comparison Between LES and Experimental (Koseff and Street, 1984c) Results in Terms of Centerline Mean Velocity Profiles; Simulation Profile at K15 Plane (z = 0.28) and Experimental Data Measured at Mid-Span Plane.

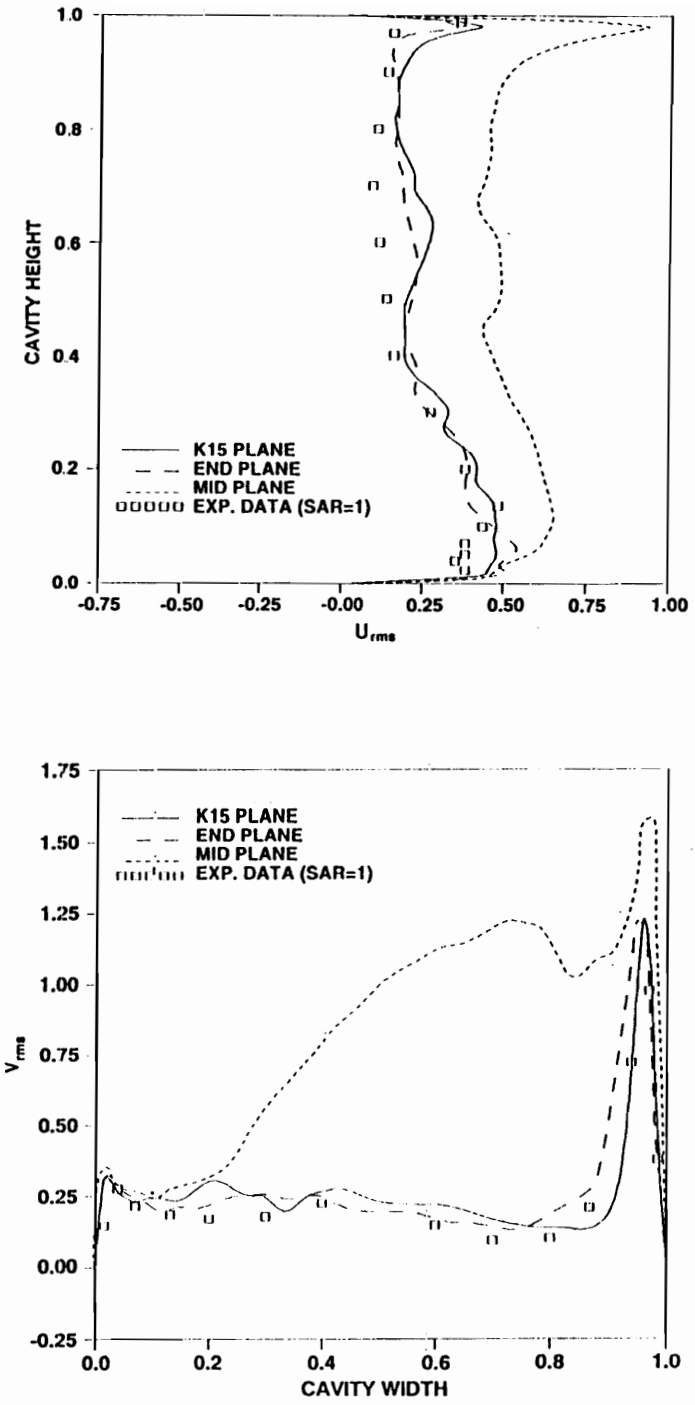

Figure 6.23. Profiles of Centerline Horizontal and Vertical RMS Velocity Fluctuations; LES Profiles are at the Spanwise K15, End and Mid-Span Planes While Experimental Data Taken at the Mid-Span Plane of Cavity with Spanwise Aspect Ratio (SAR) = 1.0.

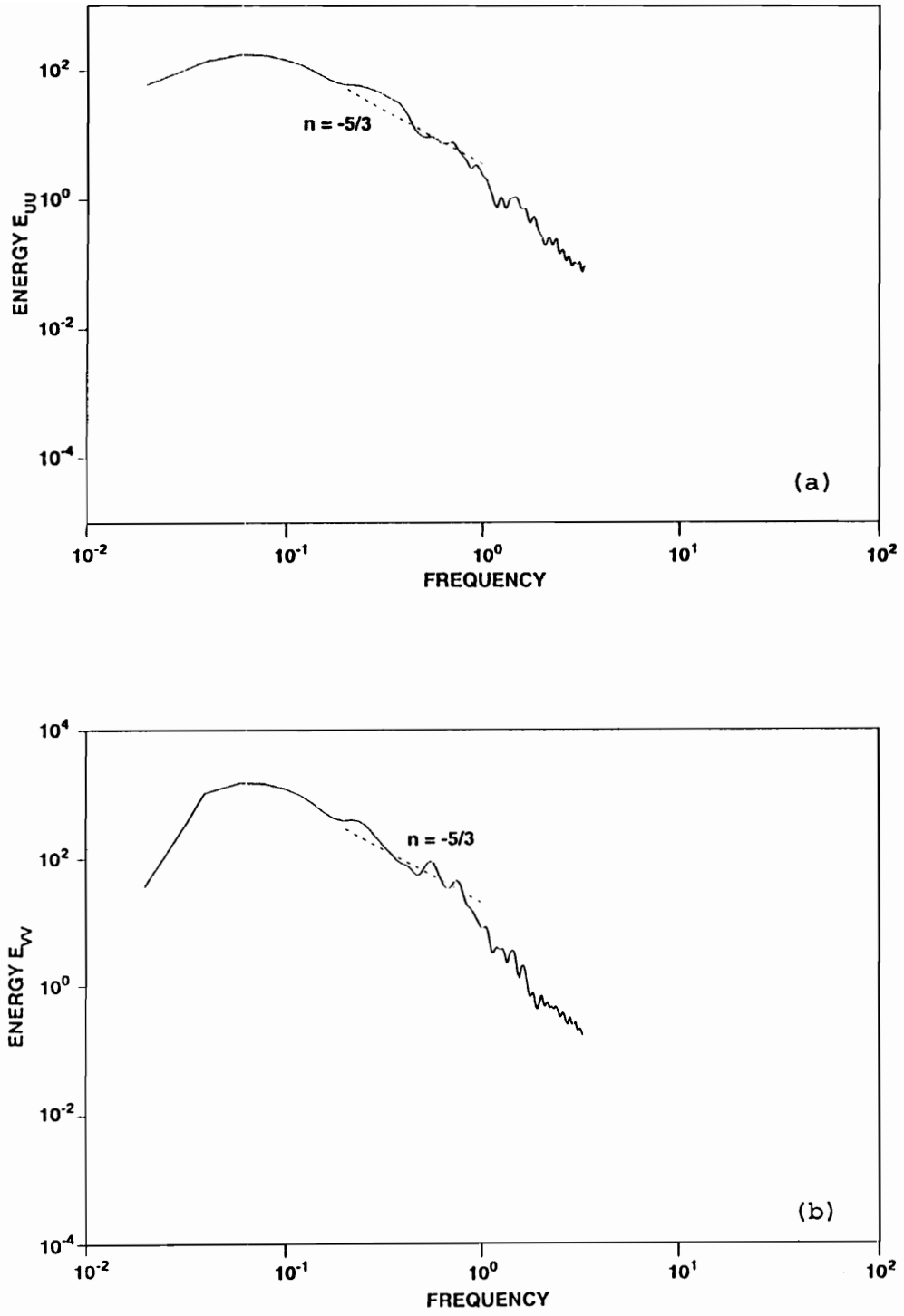

Figure 6.24. Power Spectra of Velocity Components Near the Downstream Free Shear Layer; (a) Horizontal, (b) Vertical.

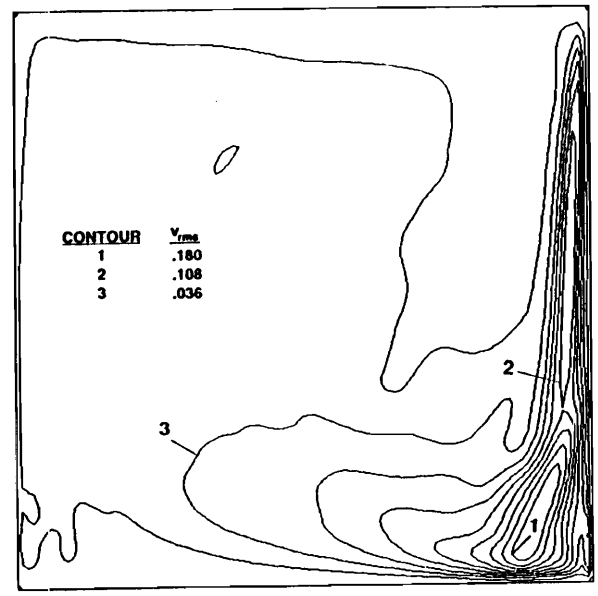

(a)

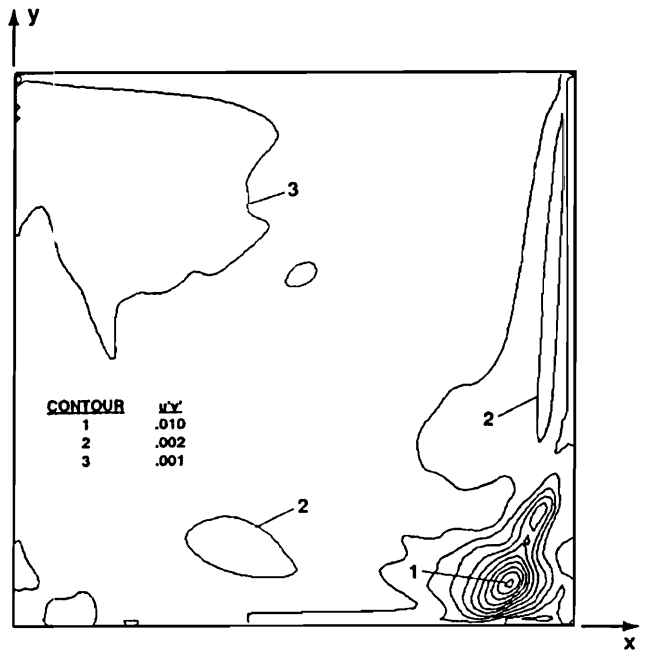

(b)

Figure 6.25. Distributions of the (a) Vertical RMS Fluctuations and (b) U'V' Turbulent Shear Stress Component at the K15 Plane; Re = 10000 and SAR = 3.0

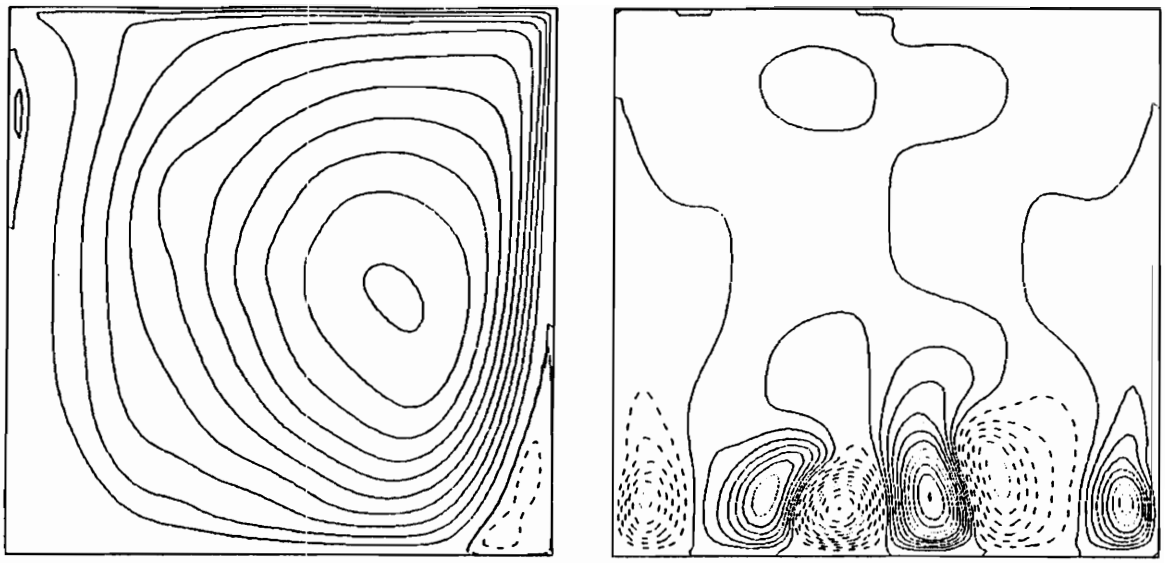

Figure 6.26. Stream Function Contours Showing the (a) Recirculation and (b) Spanwise Flow at the Mid-Span and I77 (x=0.77) Planes, Respectively; Time T = 0.0. Dashed Contours Signify Counter-Rotating Flow; Re = 5000 and SAR = 1.0

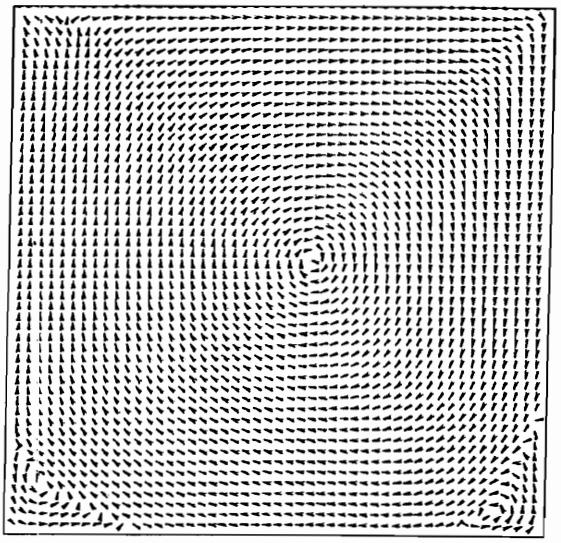

Figure 6.27. Time-Averaged Recirculation Flow Vectors at the Cavity Mid-Span Plane; Re = 5000 and SAR = 1.0

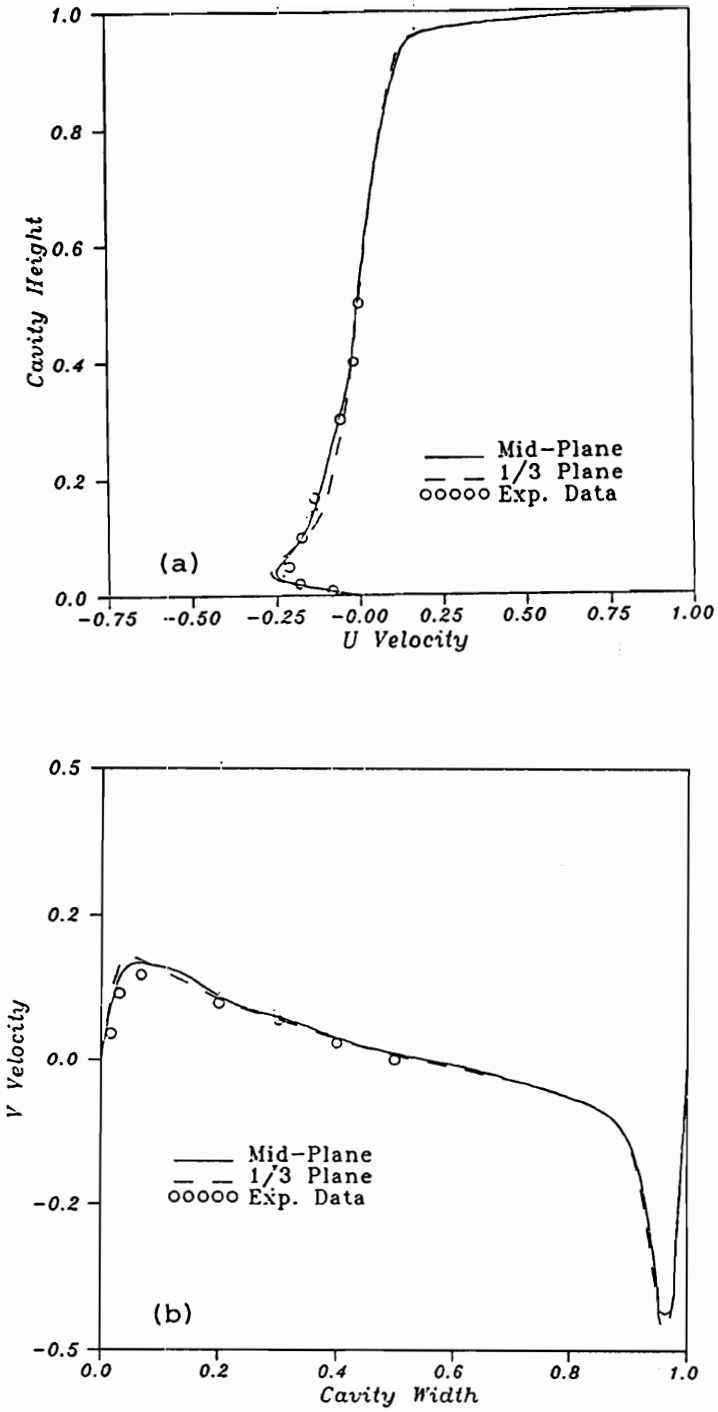

Figure 6.28. Quantitative Comparisons Between the DNS Results and Experimental Data (Koseff and Street, 1984c) in Terms of the Center-Line Mean Velocities.

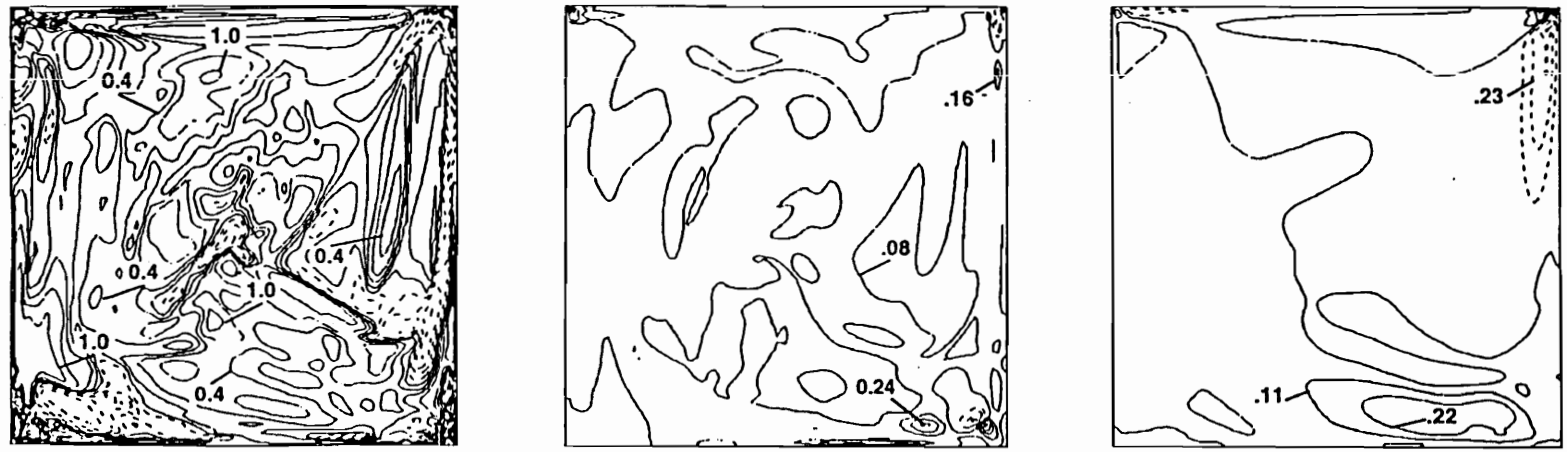

Figure 6.29. Distributions of (a) Correlation Coefficient C_{12} and (b and c) Turbulent Eddy Viscosity Using Lilly's Expression for Smagorinsky's Coefficient in the Dynamic Model Definition. Correlations and Turbulent Eddy Viscosity Levels Computed from the Initial DNS Data at Re = 5000.

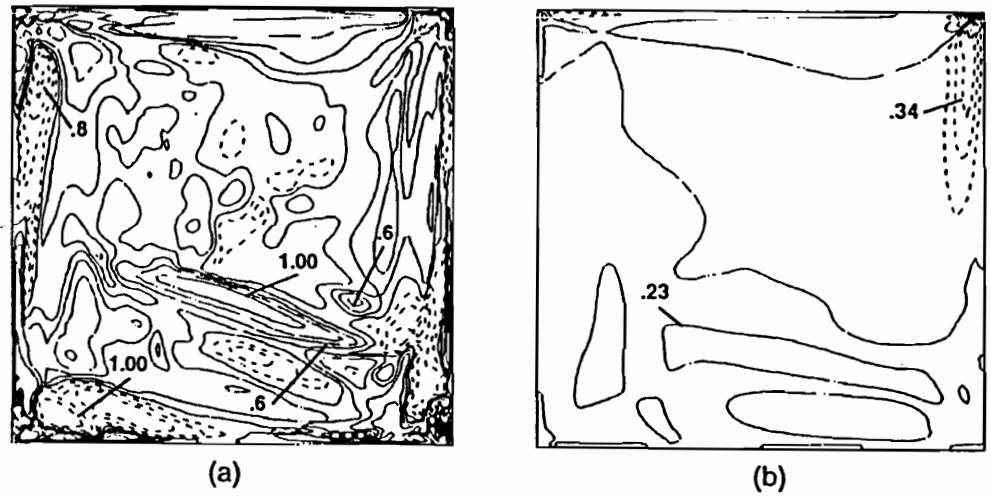

Figure 6.30. Correlation Coefficient and Turbulent Eddy Viscosity Distributions at Completion DNS Computation; Re = 5000 and SAR = 1.0.

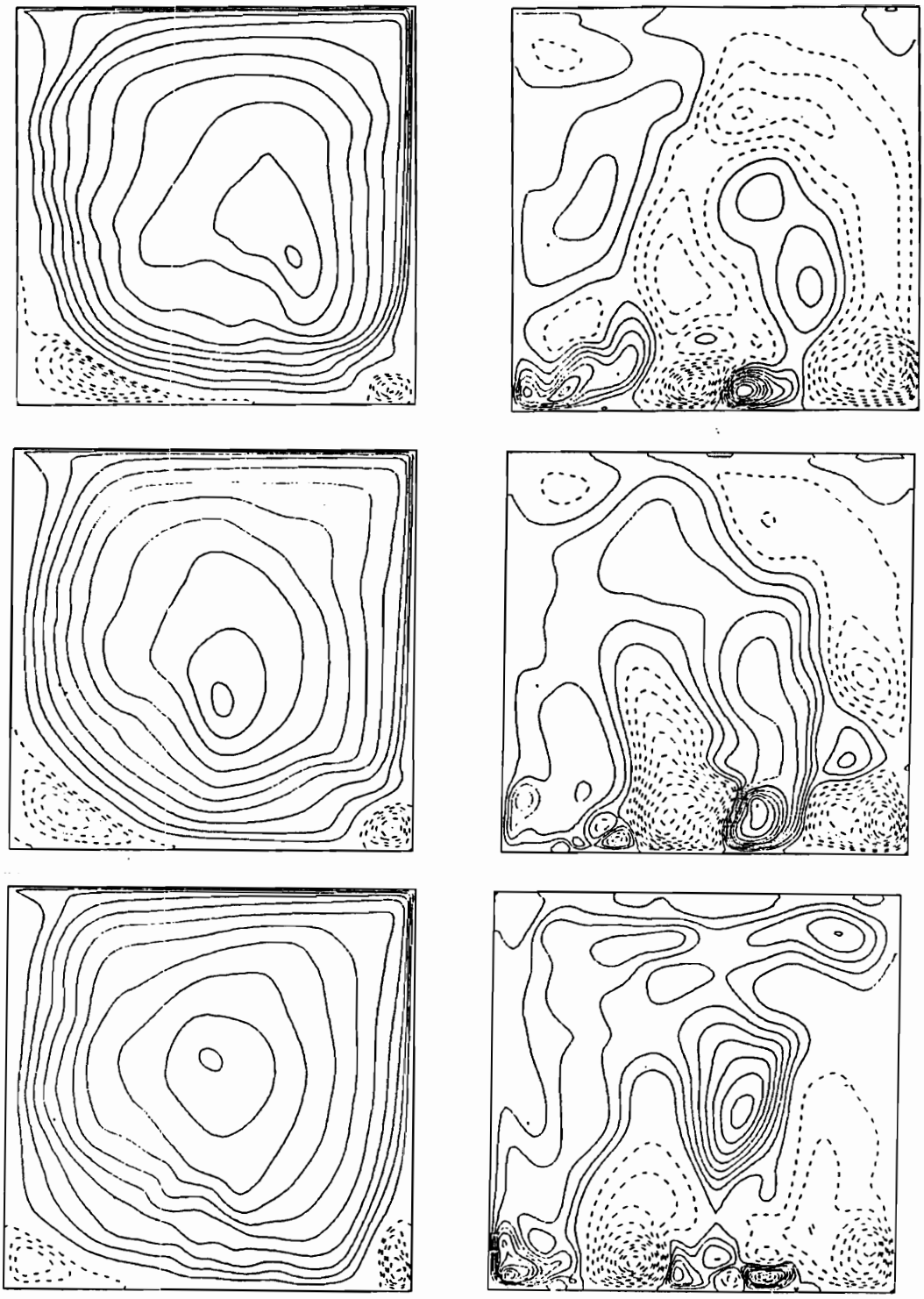

Figure 6.31. Time Sequence of Streamlines Showing the Recirculation and Spanwise Flow at the Mid-Span and I77 Planes, Respectively. The Dashed Streamlines Indicate Counter-Rotating Flow; Re = 10000 and SAR = 1.0.

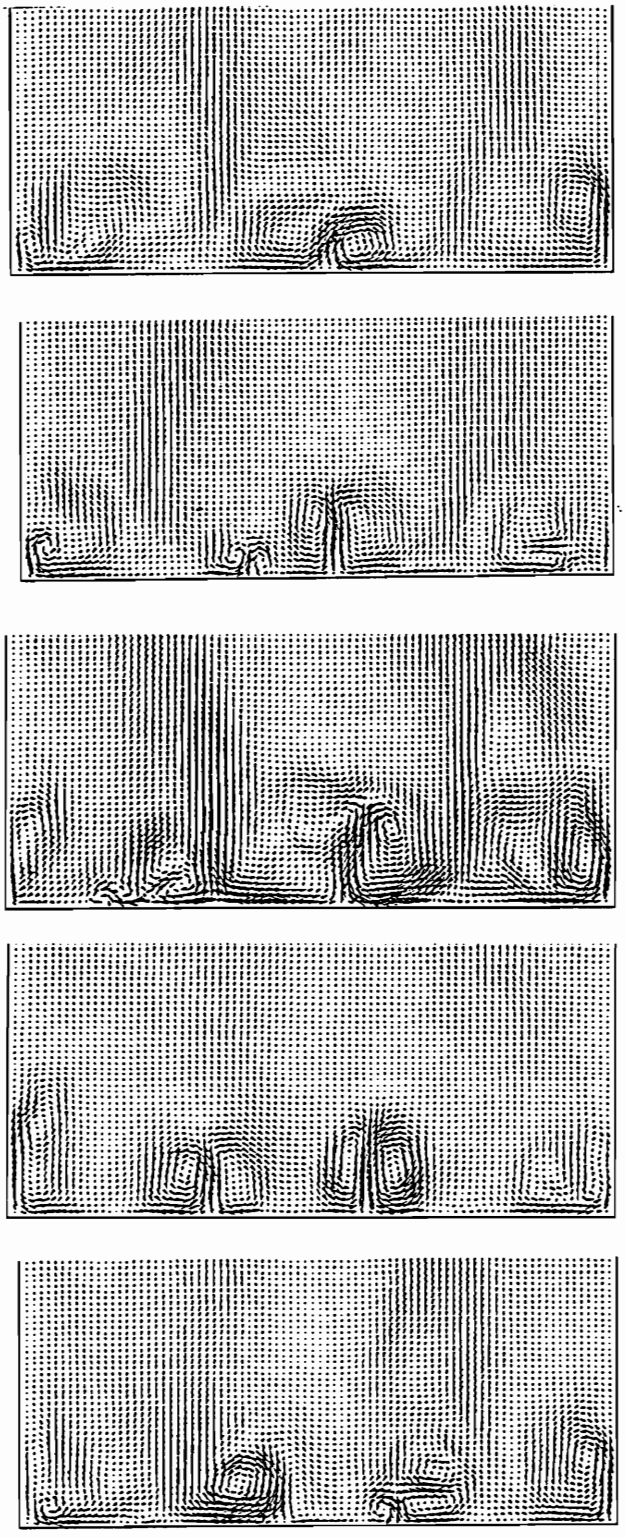

Figure 6.32. Snapshots of the Unsteady Spanwise Shear-Driven Cavity Flow at I77 Plane

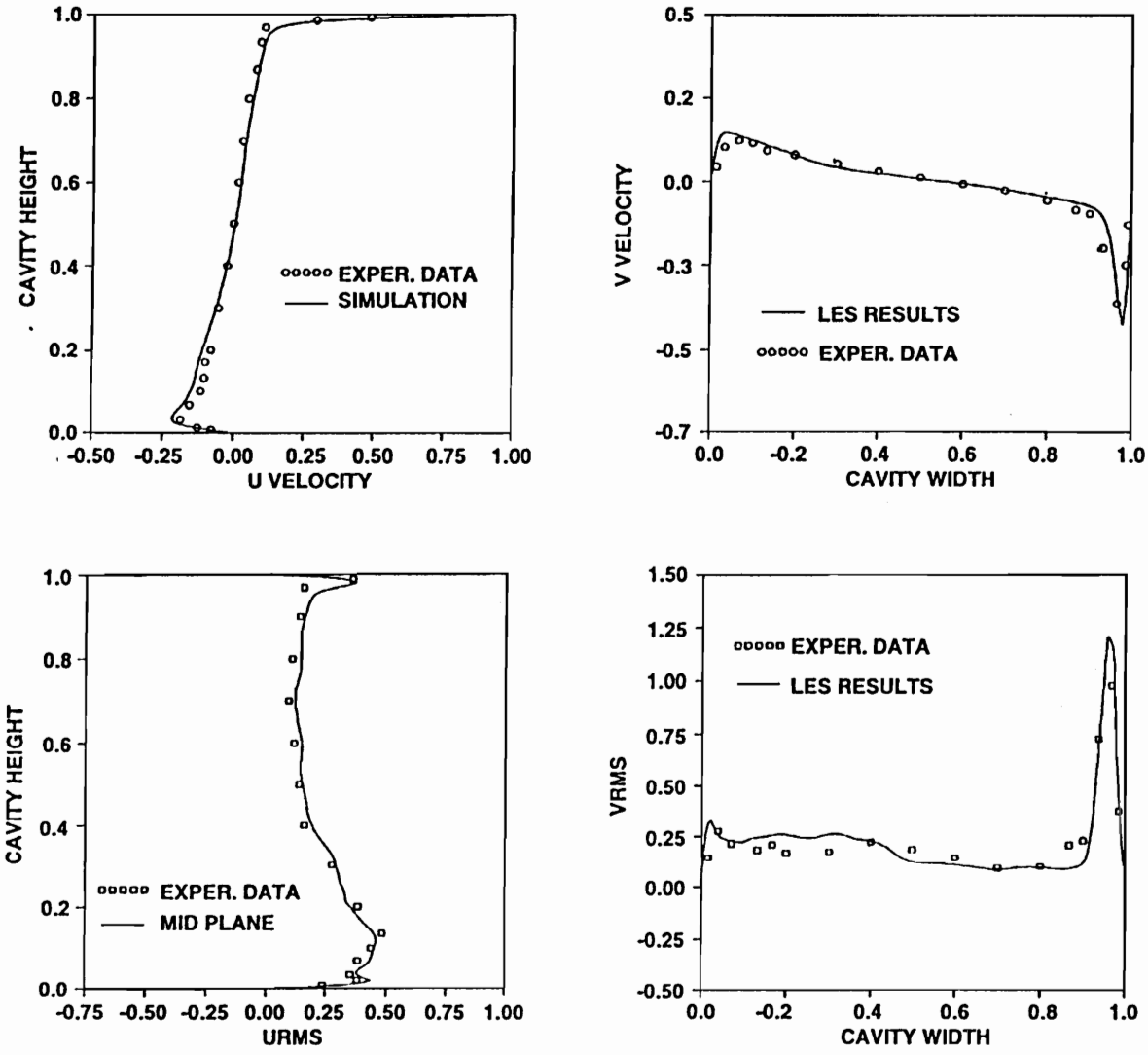

Figure 6.33. Centerline Mean and RMS Profiles of Horizontal and Vertical Velocity Fluctuations; Re = 10000.

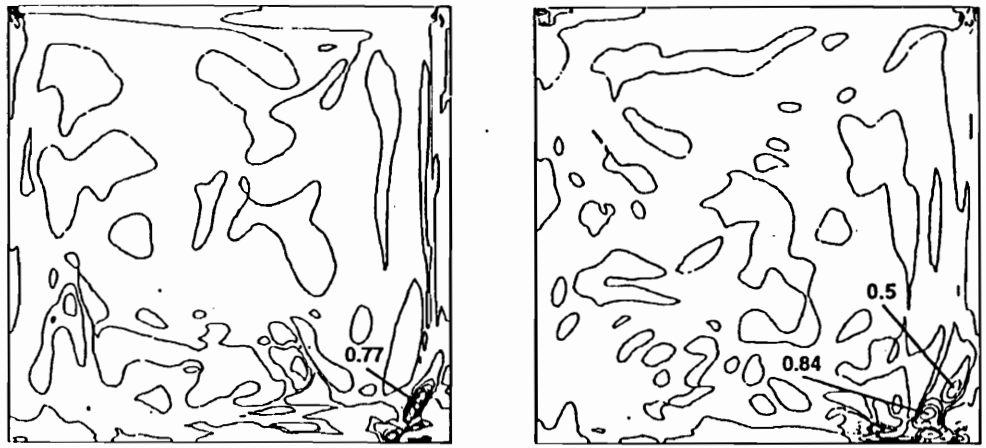

Figure 6.34. Turbulent Eddy Viscosity Distributions at Completion LES Computation; Re = 10000 and SAR = 1.0.

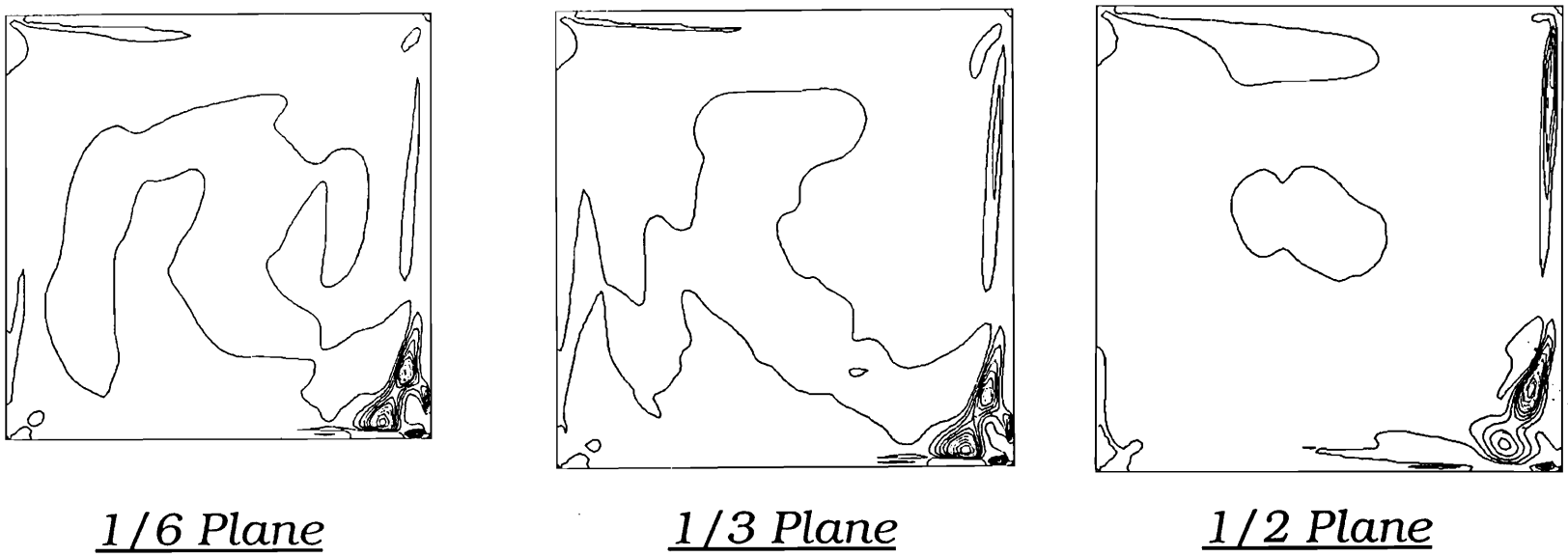

Figure 6.35. Time-Averaged Turbulent Production Levels at Spanwise Planes Z = 1/6, 1/3 and Mid-Span; Re = 10000 and SAR = 1.0.

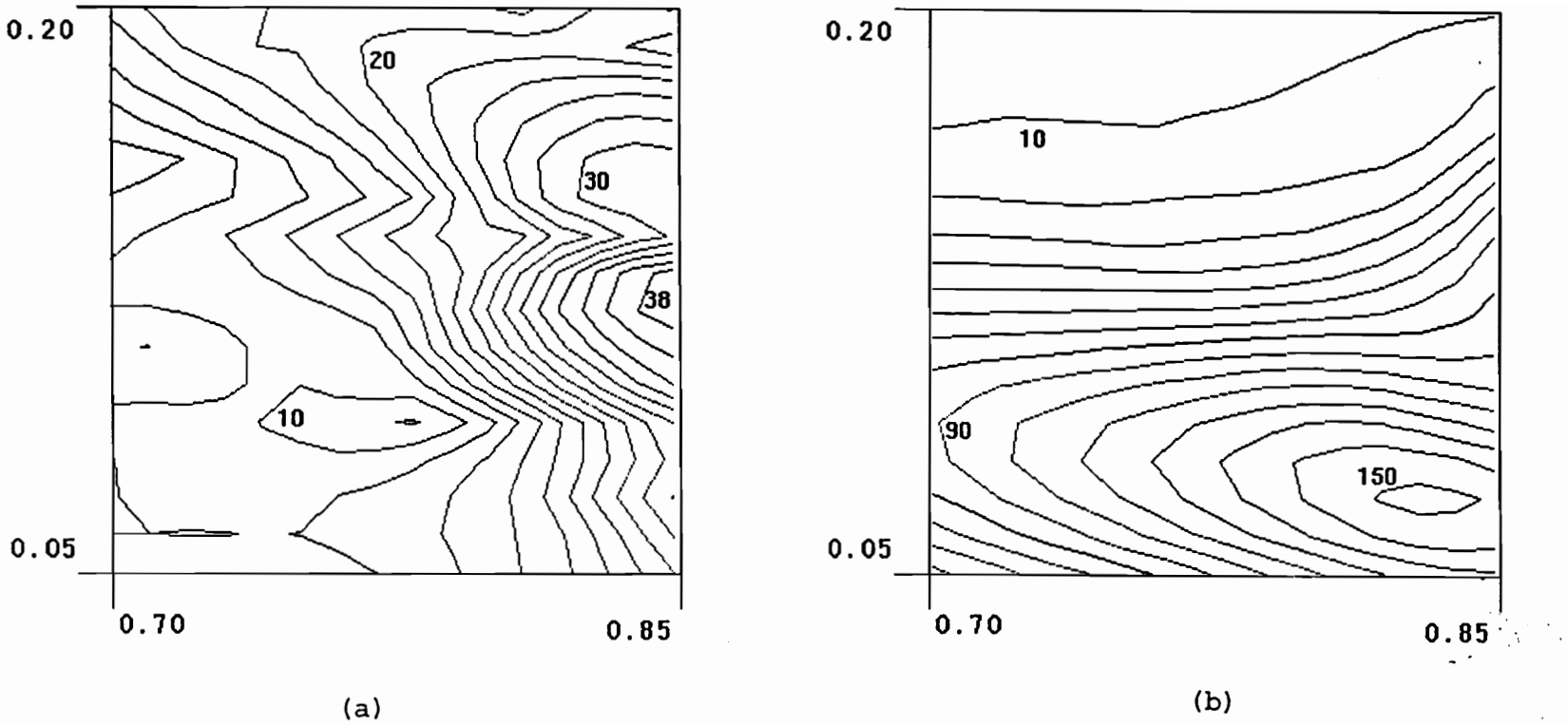

Figure 6.36. Maximum Power Spectral Energy of the Velocity Fluctuations at the Mid Span Plane; (a) Horizontal, (b) Vertical; Re = 10000 and SAR = 1.0.

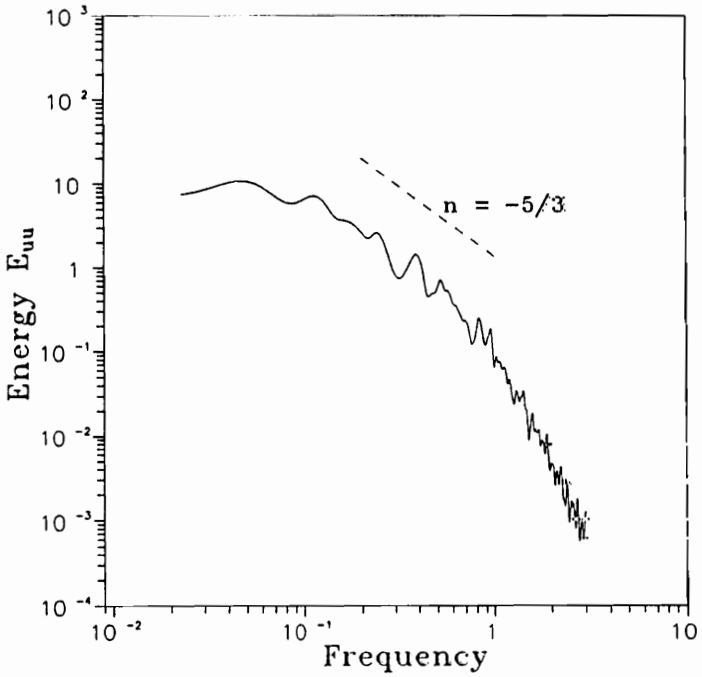

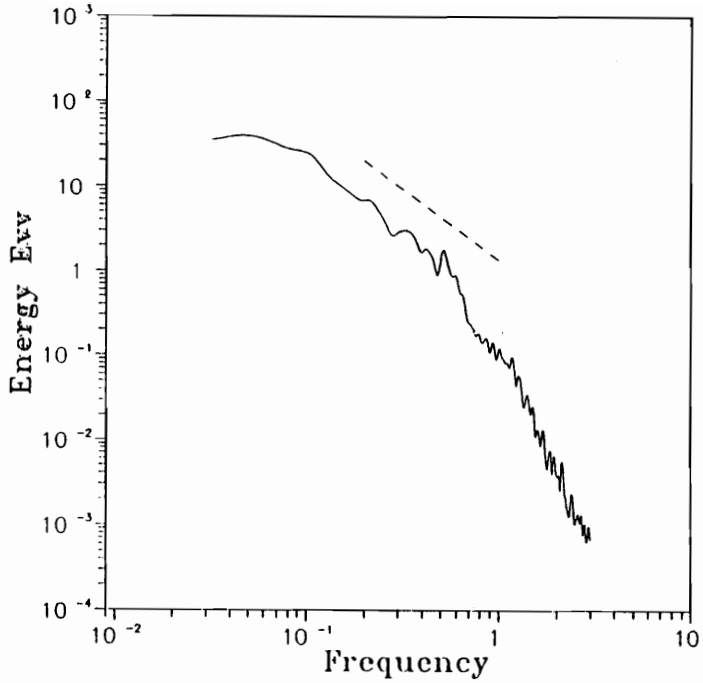

Figure 6.37. Typical Frequency Spectra of Velocity Fluctuations Within the Region of the Downstream Secondary Eddy; (a) Horizontal, (b) Vertical. Corresponding Time Trace Data Generated at 20 Hz Sampling Rate.

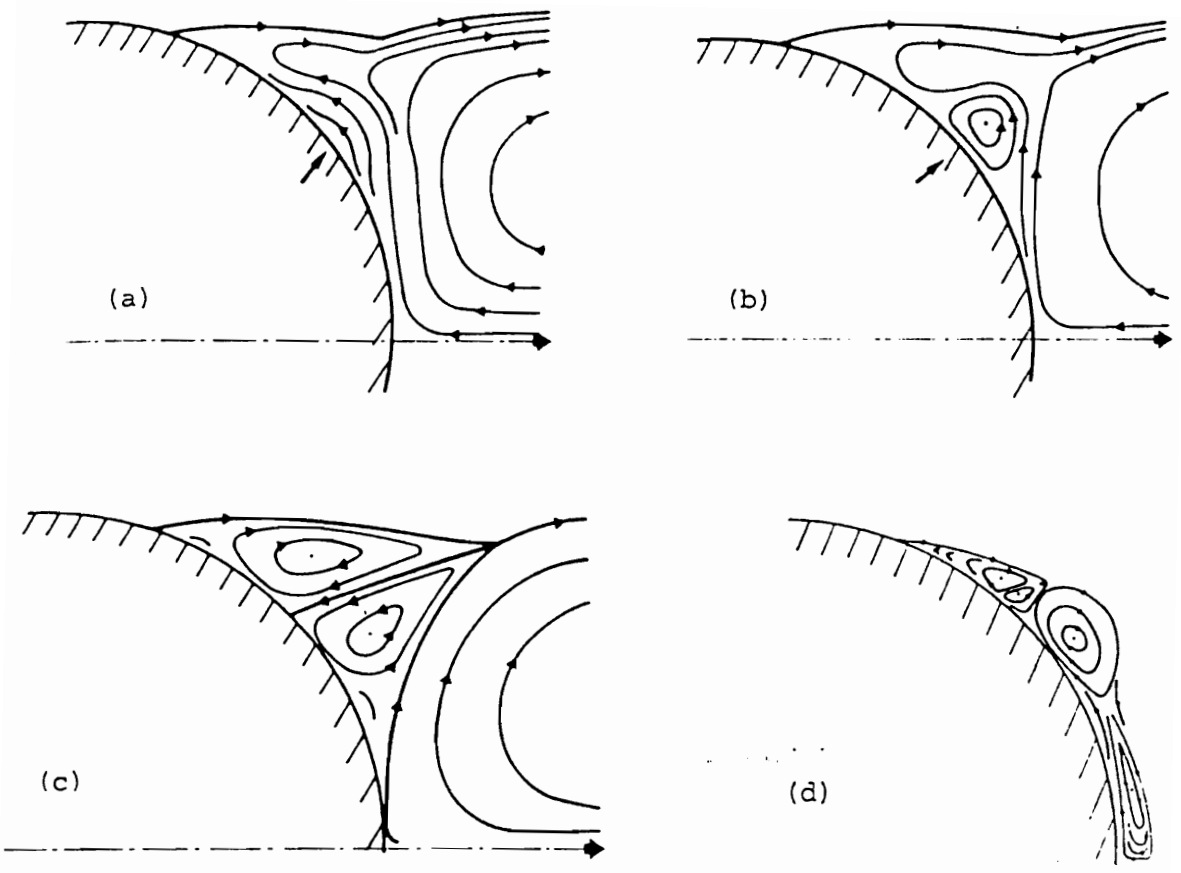

Figure 7.1. Sketches of Early Cylinder Wake Characteristics; (a) $T \equiv$ 1, $100 \leq Re \leq 500$, (b) $T > 1$, $500 \leq Re \leq 800$, (c) $T > 1$, $Re > 800$ and (d) $T < 1.5$, $Re > 3000$.

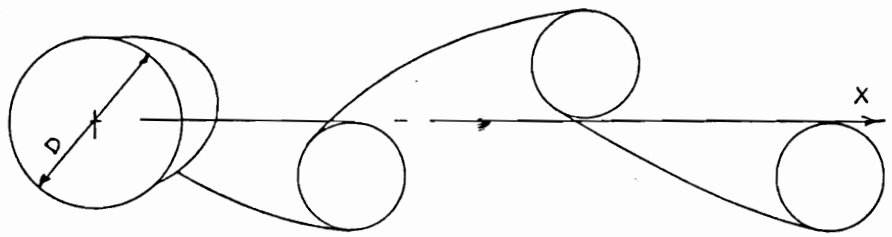

Figure 7.2. Topology of the Cylinder Near Wake at Re = 5600.

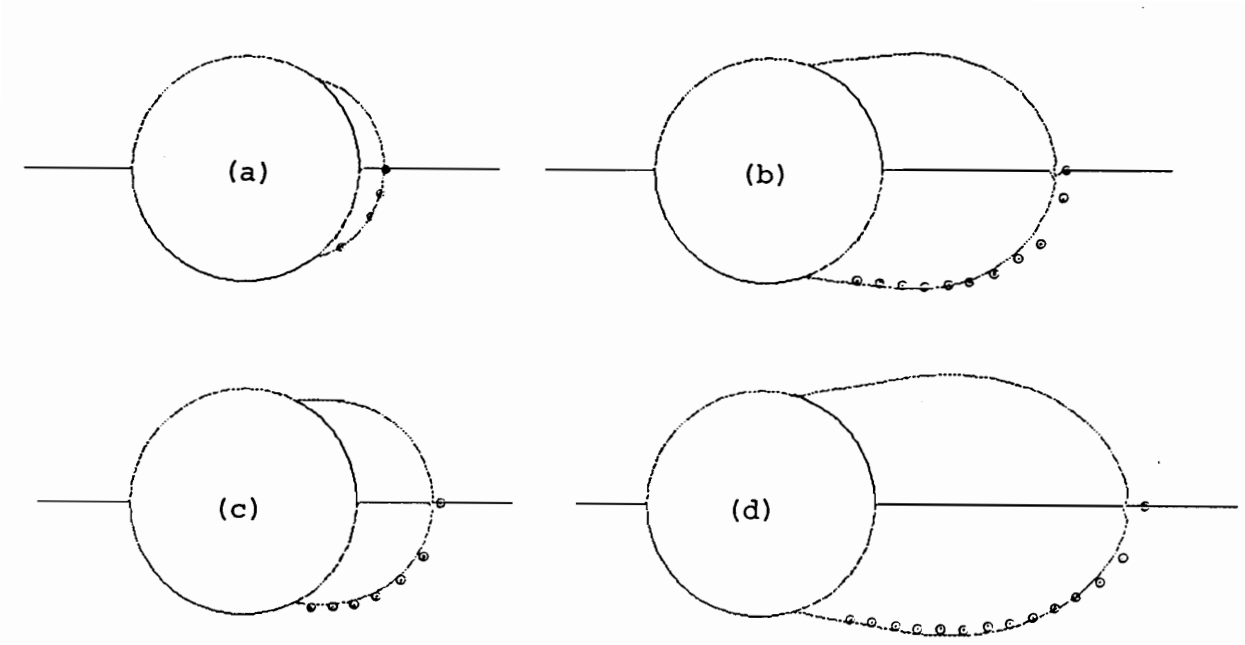

Figure 7.3. ***Early Wake Flow Comparisons of DNS Results and Experimental Data (Bouard and Coutanceau, 1980) of the Exterior Wake Boundary for Re = 200 and at Times (a) T = 0.5, (b) T = 1.0, (c) T = 2.0, and (d) T = 3.0.***

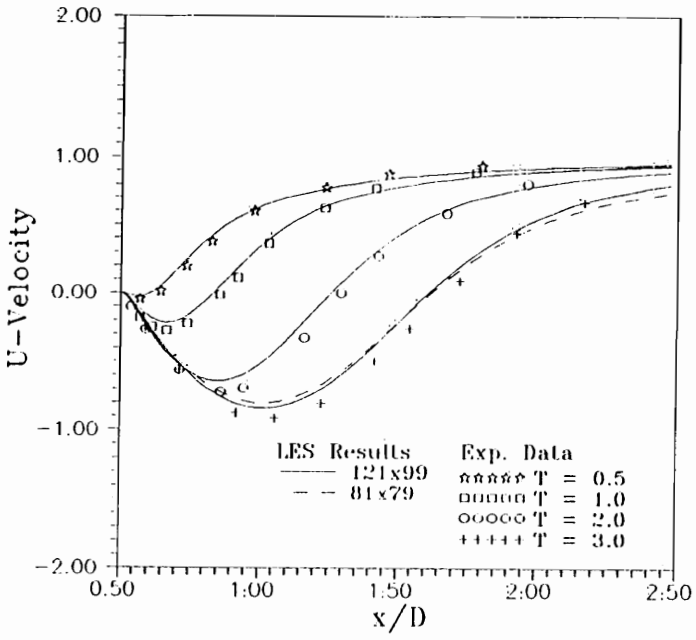

Figure 7.4. ***Early Wake Flow Comparisons of DNS Results and Experimental Data (Bouard and Coutanceau, 1980) of the Horizontal Centerline Velocity for Re = 200***

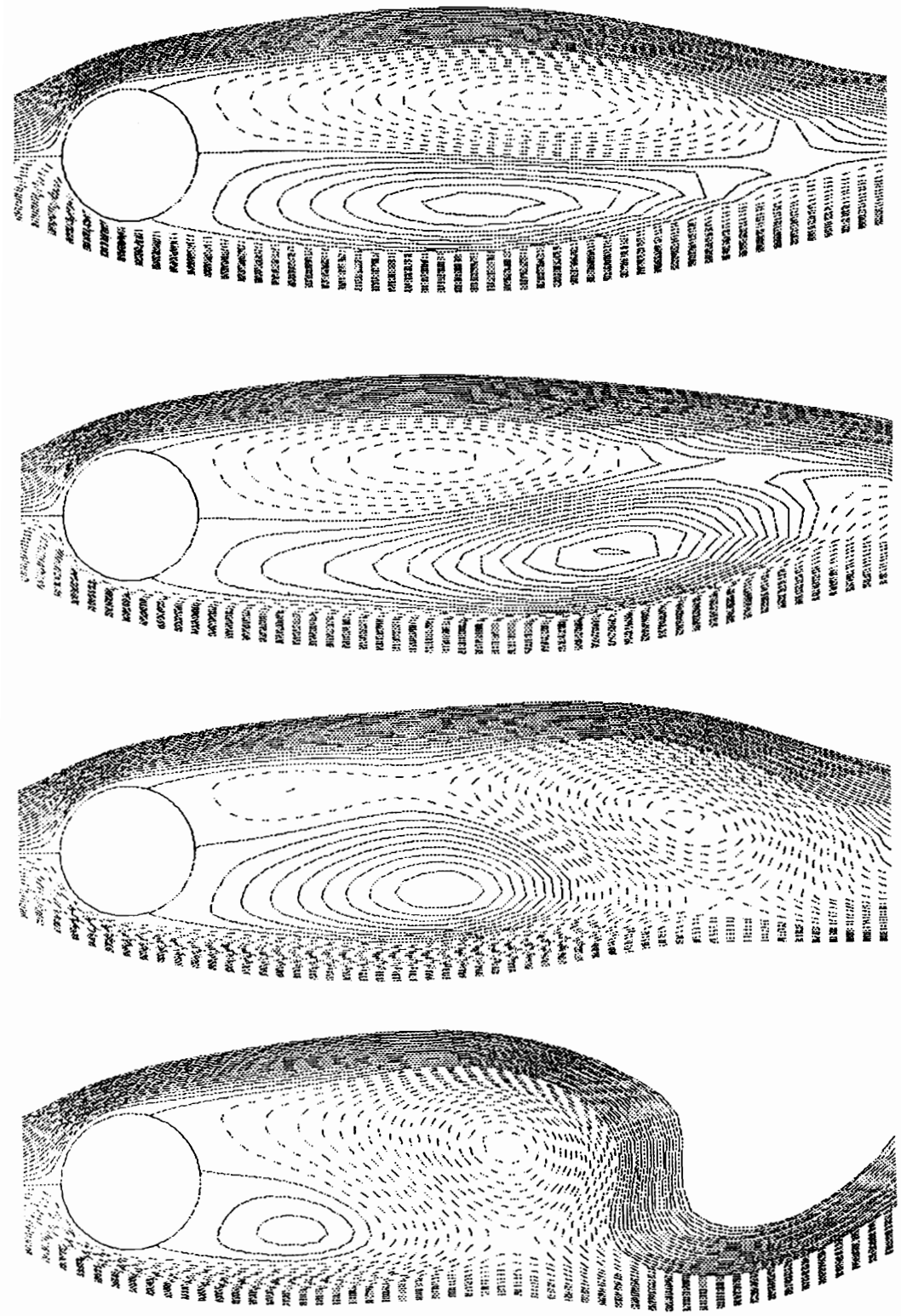

Figure 7.5. Visualization of Transition from the Stable Wake to Vortex Shedding for Re = 200.

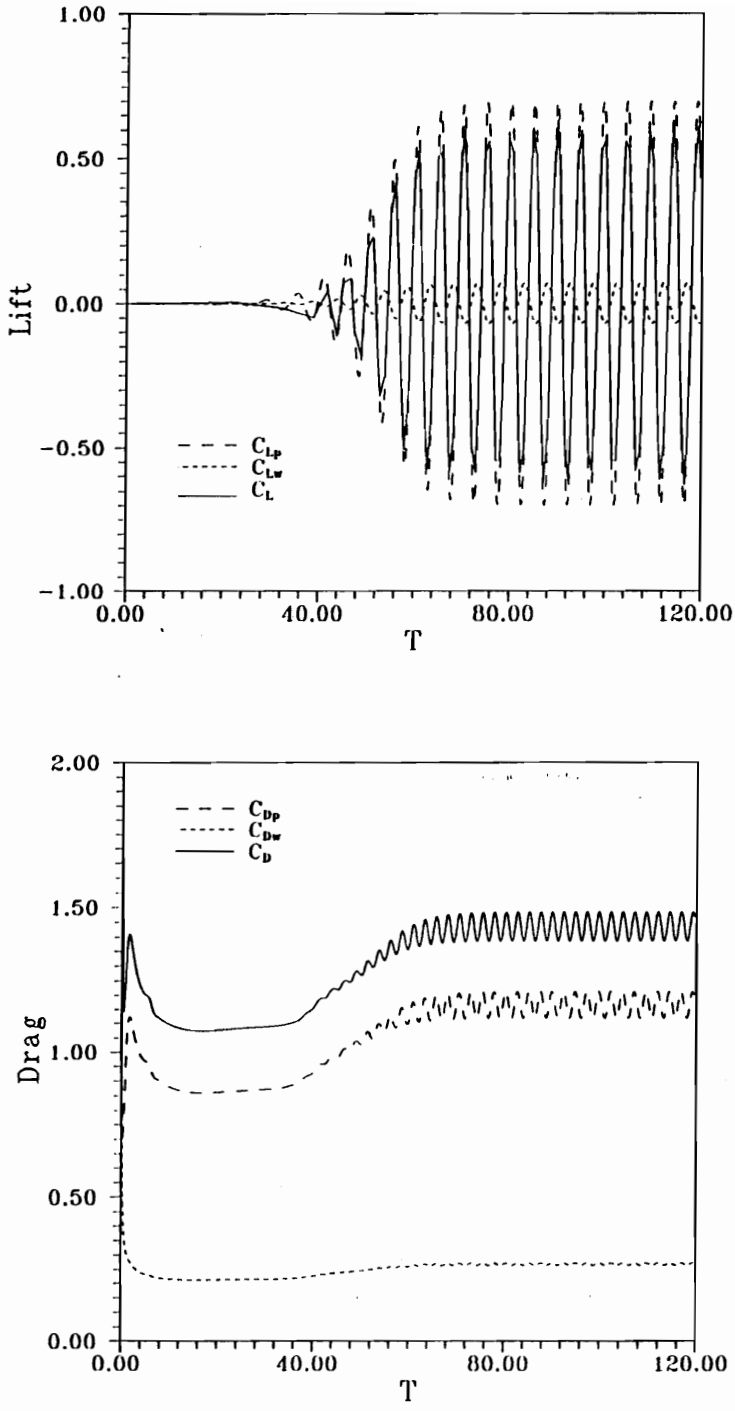

Figure 7.6. Profiles of Force Coefficients During Early Wake Formation of a Circular Cylinder at Re = 200.

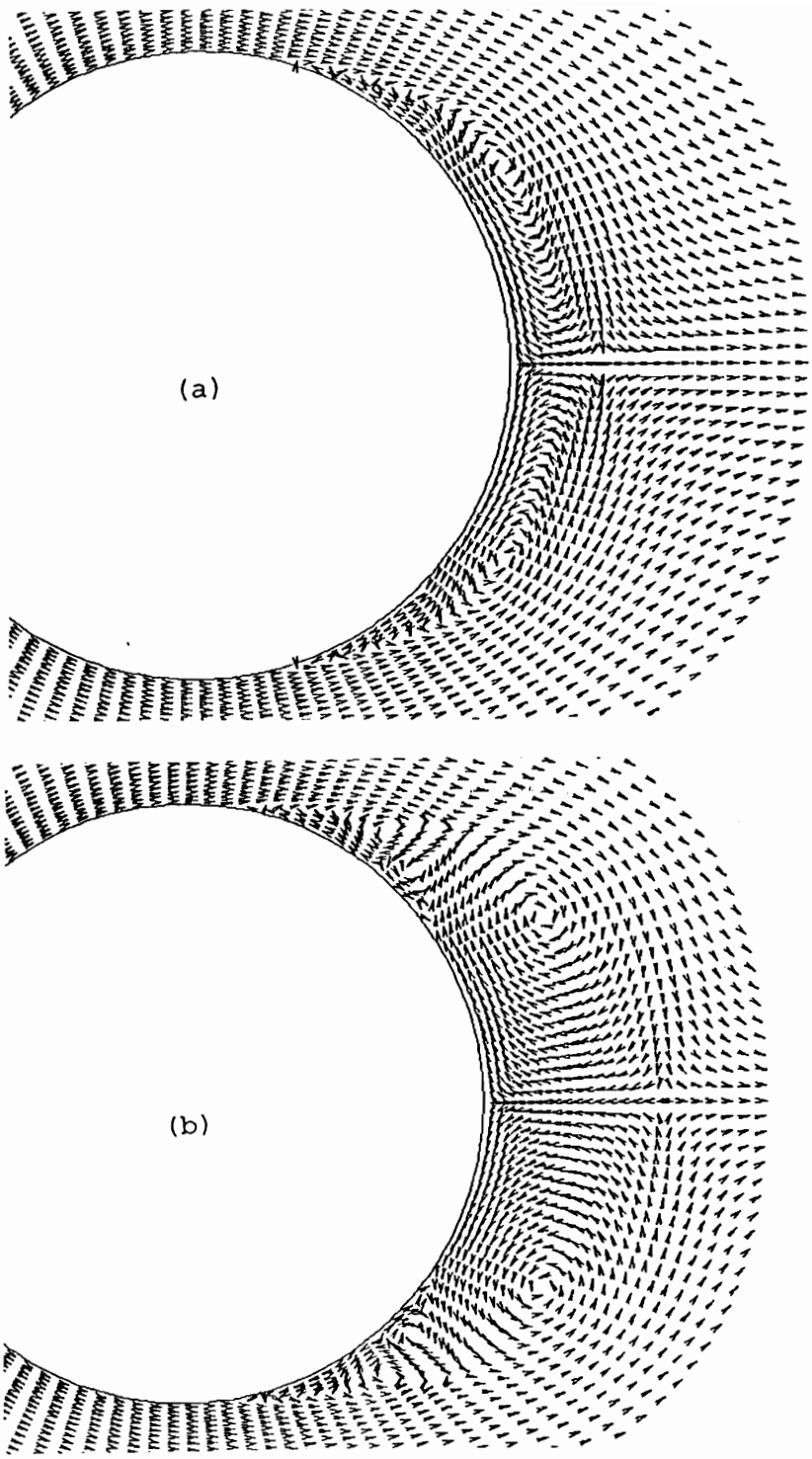

Figure 7.7. Snapshots of Early Wake Formation of Circular Cylinder at Re = 3000; (a) T = 1.0 and (b) T = 1.5.

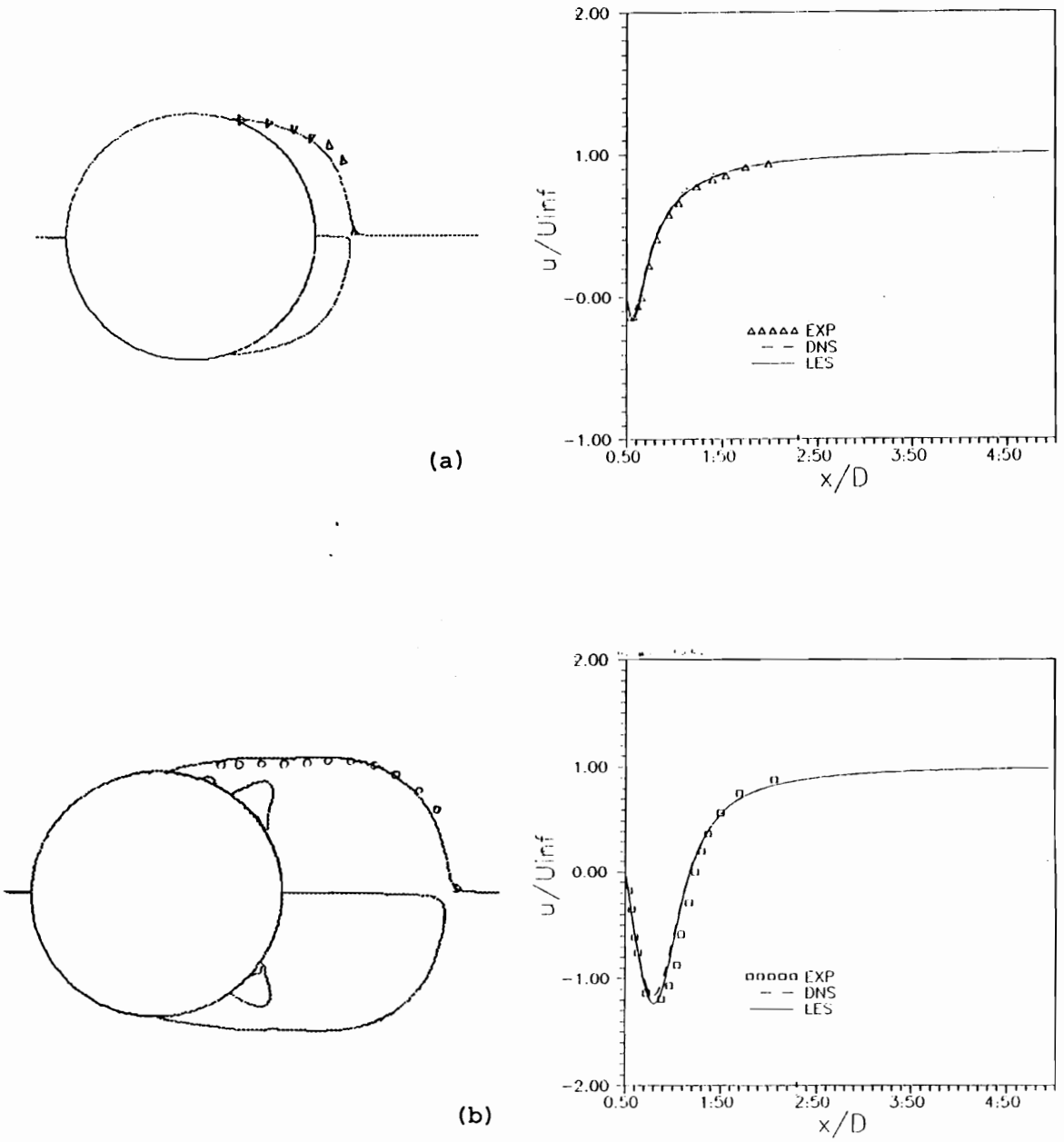

Figure 7.8. ***Early Wake Flow Comparisons of LES Results and Experimental Data (Bouard and Coutanceau, 1980) of the Exterior Wake Boundary and Horizontal Centerline Velocity for Re = 3000 and at Times (a) T = 1.0 and (b) T = 2.5.***

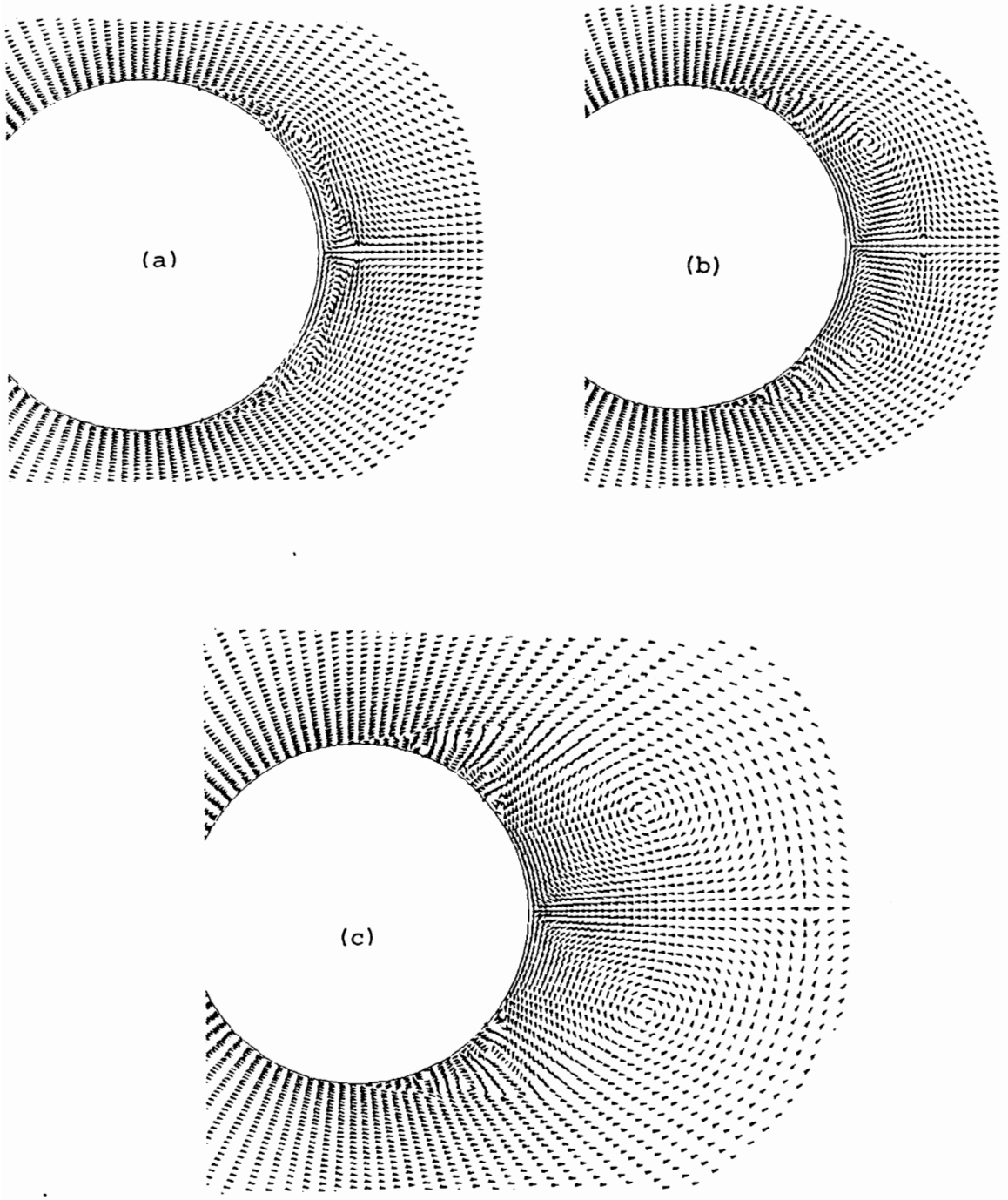

Figure 7.9. ***Snapshots of Early Wake Formation of Circular Cylinder at Re = 5600; (a) T = 1.0, (b) T = 1.5 and (c) T = 3.0.***

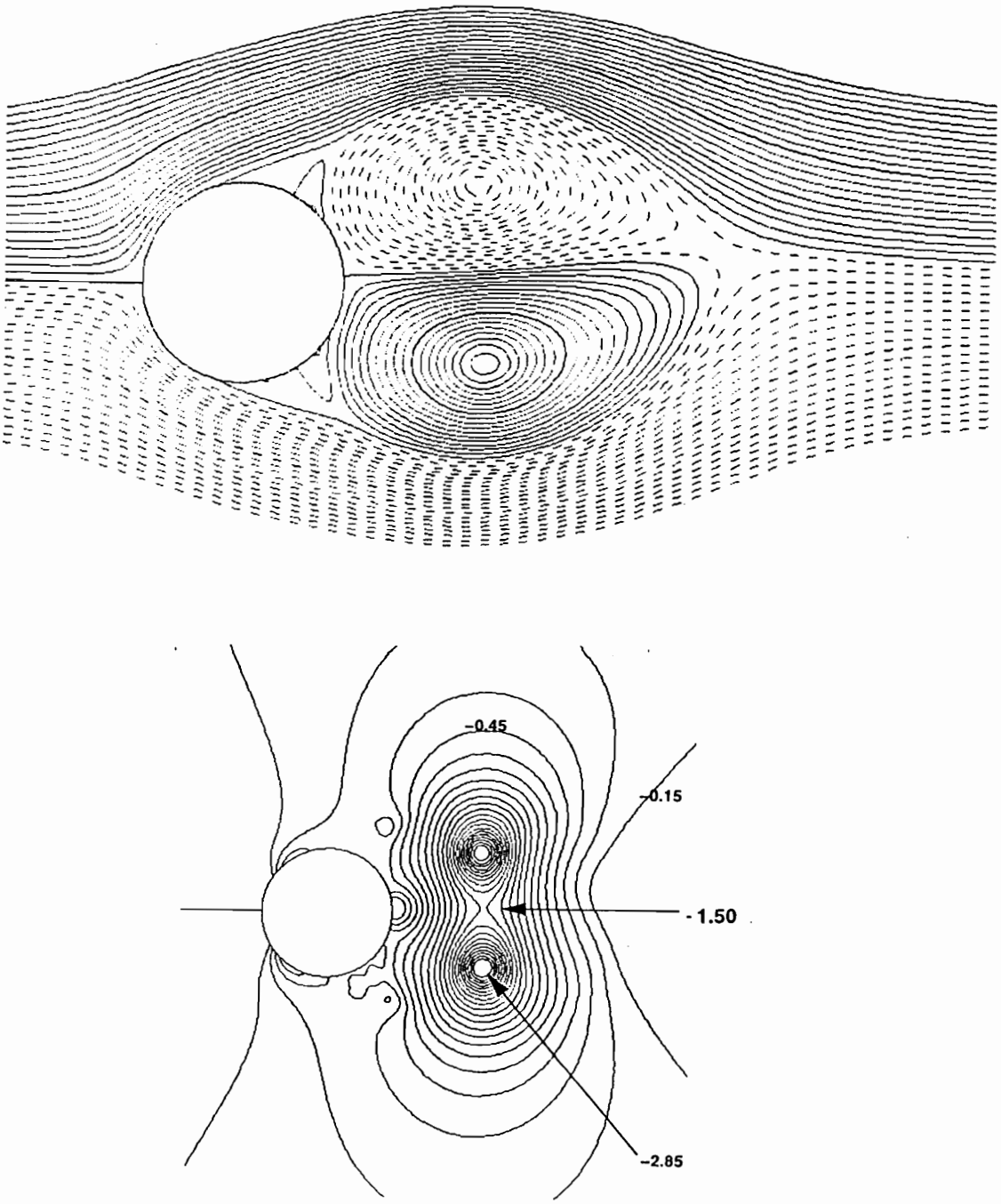

Figure 7.10. Streamlines and Pressure Contours at Initial Destabilization of Early Wake; T = 11 and Re = 5600.

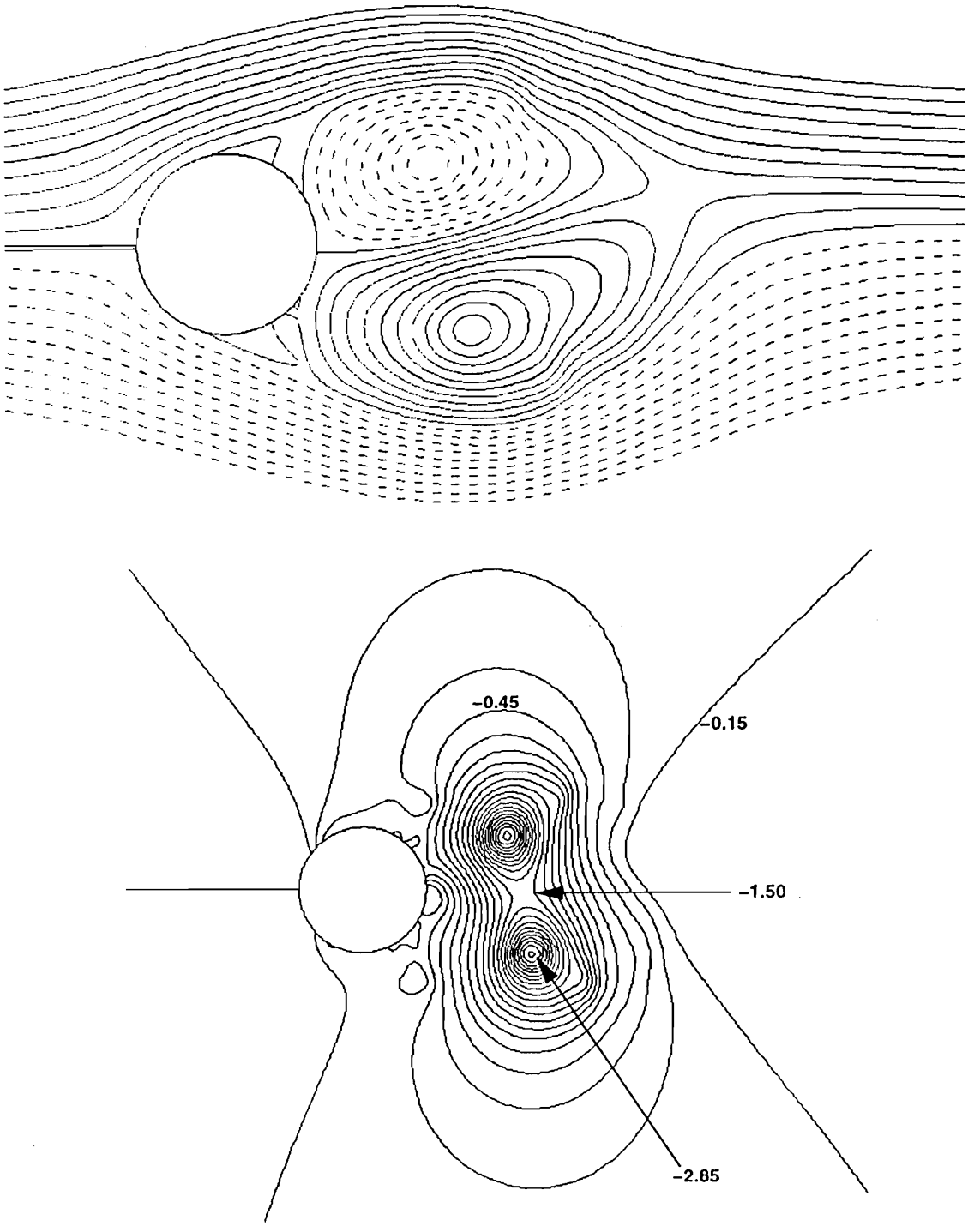

Figure 7.11. Streamlines and Pressure Contours of Destabilizing Wake at Time T = 13; Re = 5600.

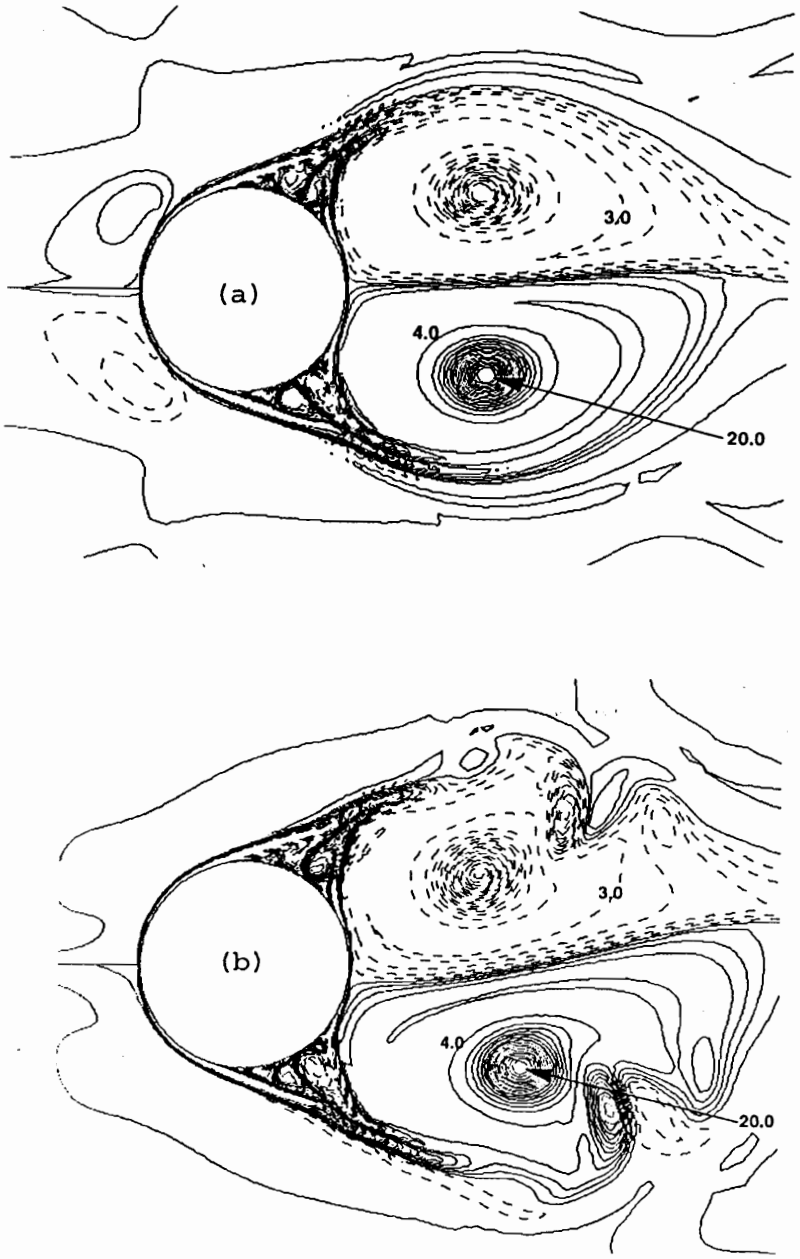

Figure 7.12. Vorticity Contours of Desatabilizing Wake at Times (a) T = 11 and (b) T = 13; Re = 5600. Negative Contours Depicted by Dashed Lines.

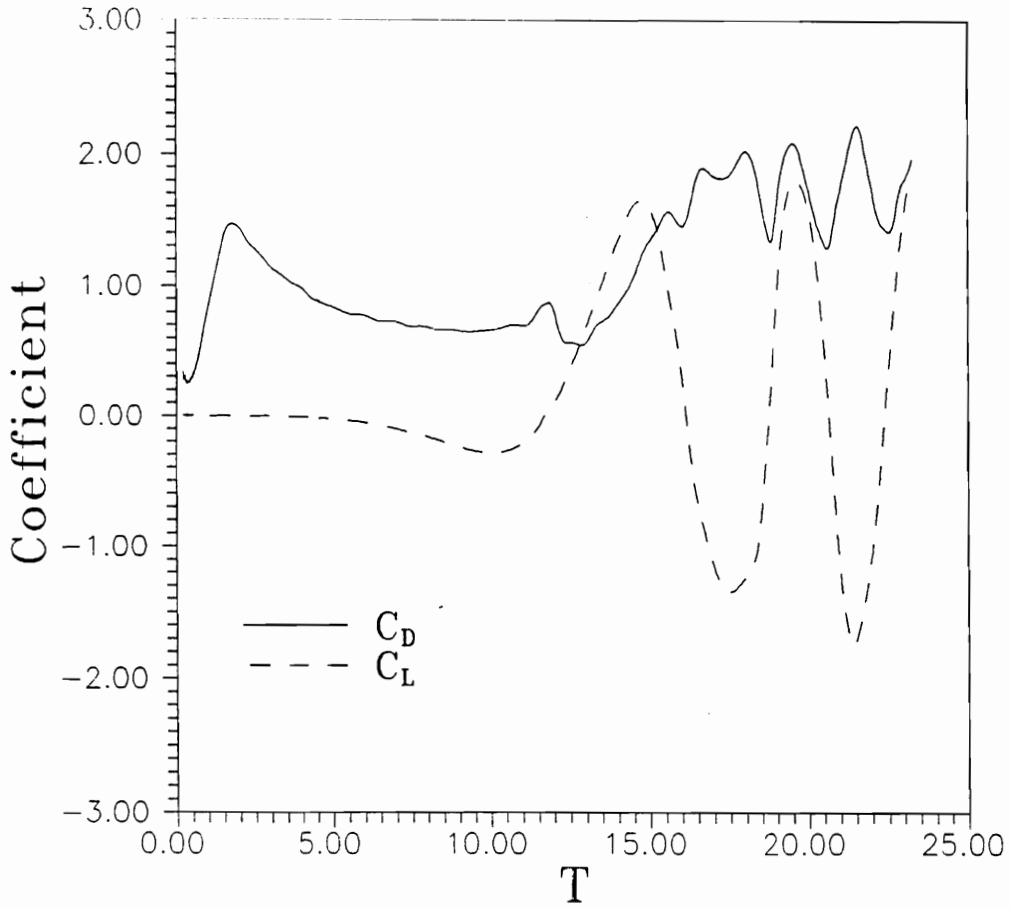

Figure 7.13. Profiles of Force Coefficients During Early Wake Development at Re = 5600.

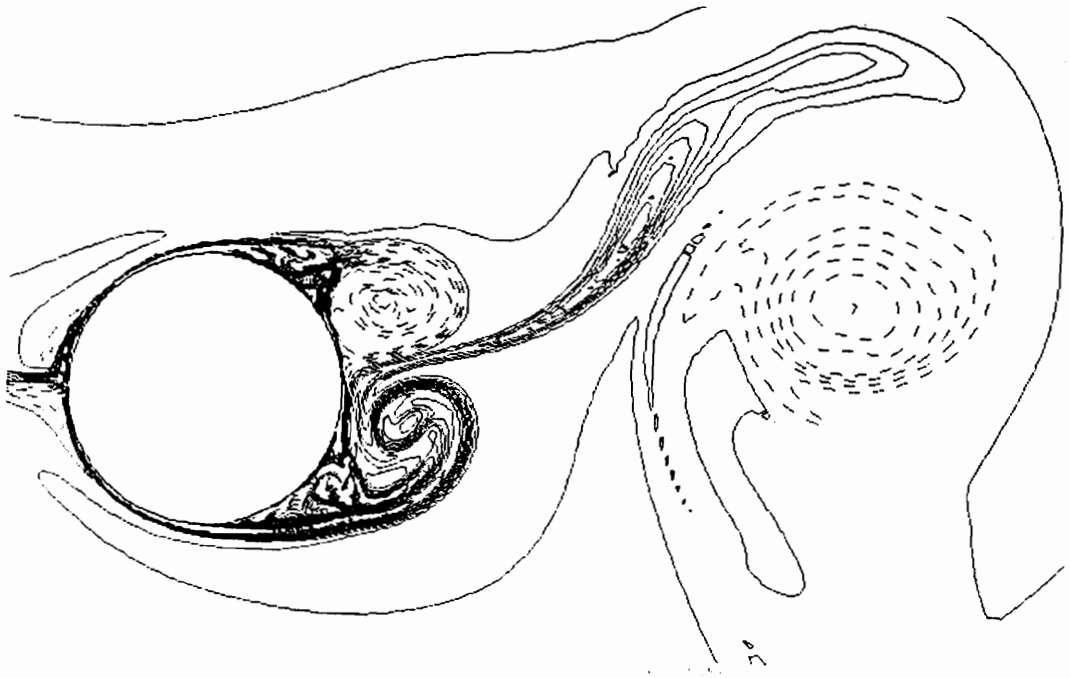

Figure 7.14. Snapshot of the Voticity Contours Near the Cylinder Surface; Re = 5600.

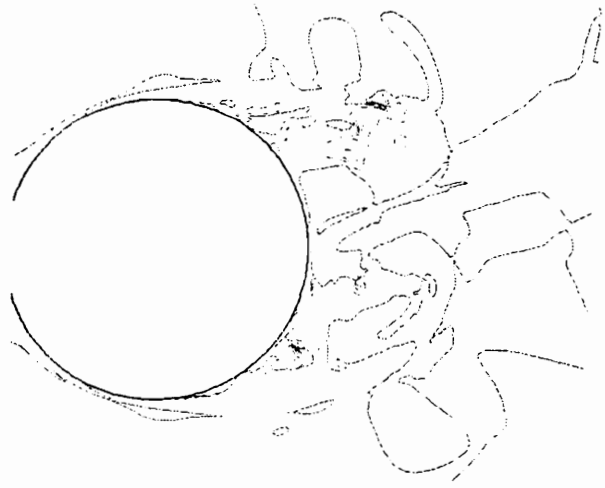

Figure 7.15. Turbulent Eddy Viscosity Levels Corresponding to the Vorticity Contours Shown in Fig. 7.14.

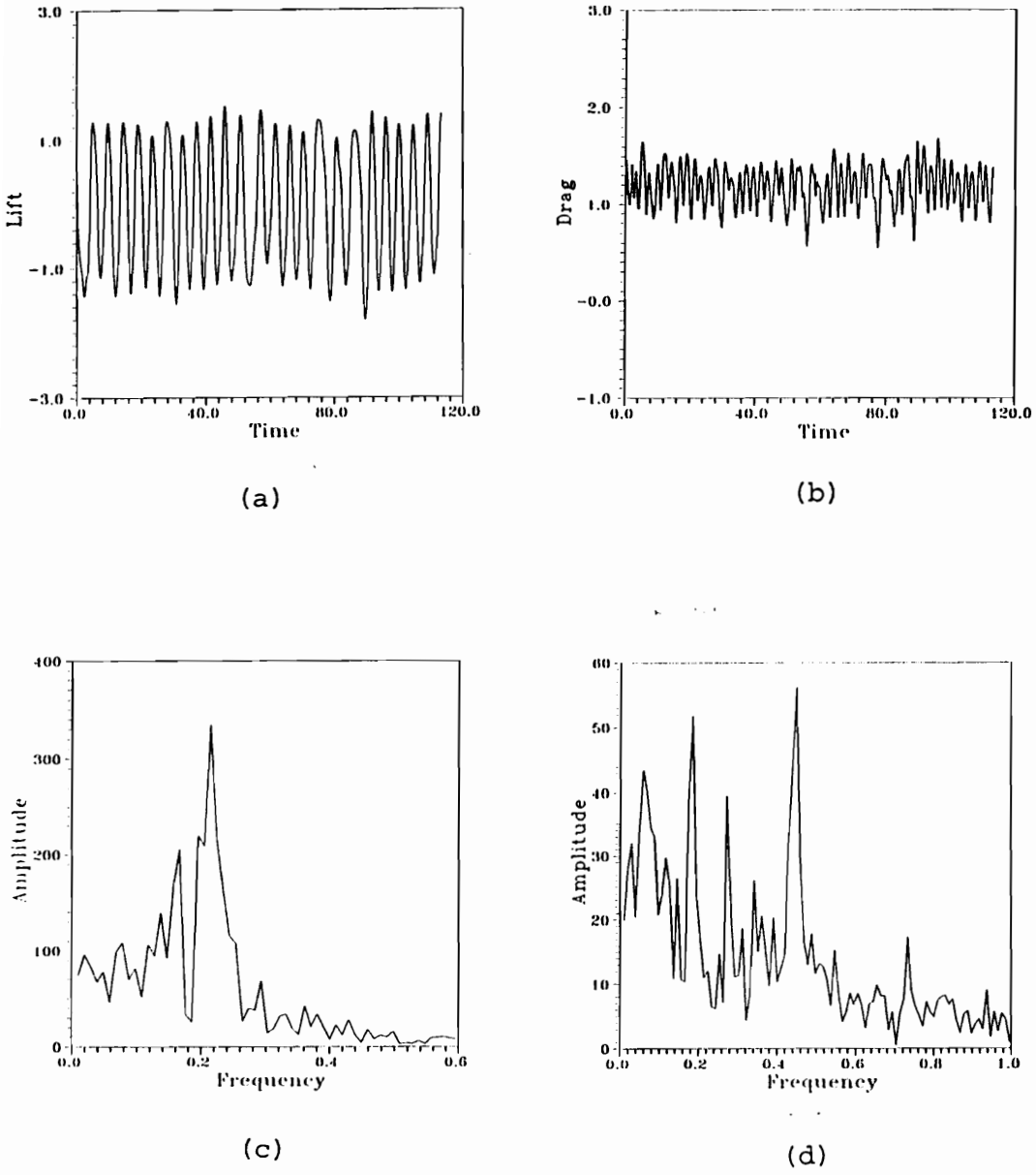

Figure 7.16. Drag and Lift Force Profiles Over Approximately 23 Cycles and Amplitudes of Corresponding Transform Coefficients; (a) Lift Force, (b) Drag Force, (c) FTT Lift Coefficient and (d) FFT Drag Coefficient. Sampling Rate was 10 Hz.

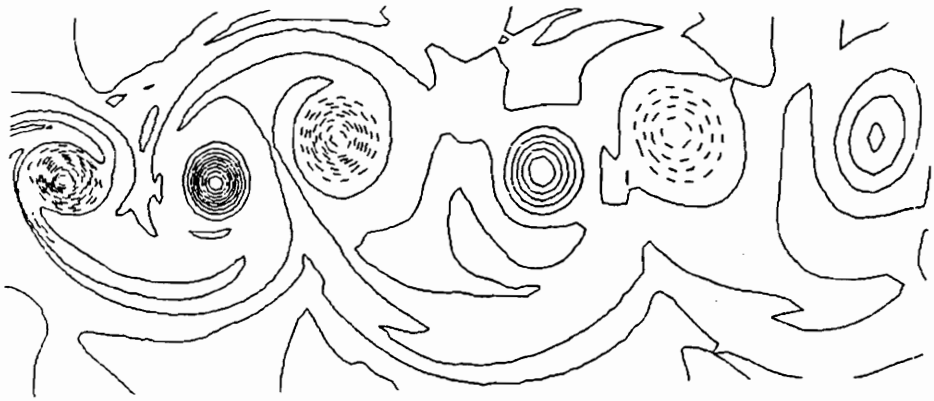

Figure 7.17. Snapshot of Shed Vortices in Cylinder Wake. Dashed Contours Signifiy Negative Vorticity.

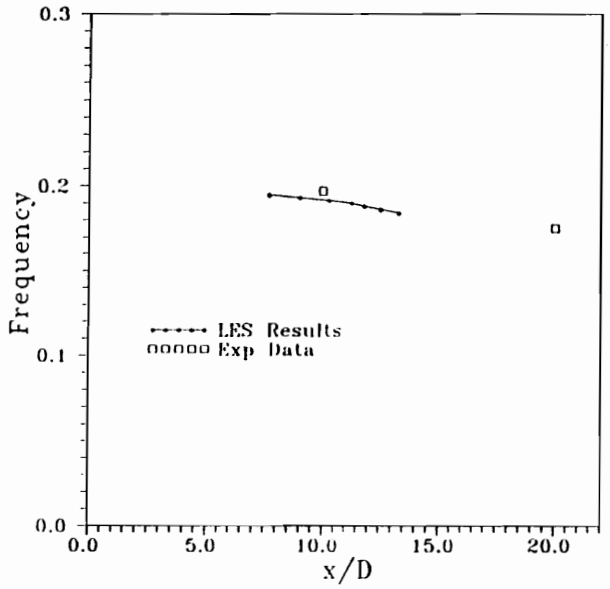

Figure 7.18. Comparison of Experimental (Zhou and Antonia, 1993) and LES Time - Averaged Downstream Decay of the Vortex Detection Frequency; Re = 5600.

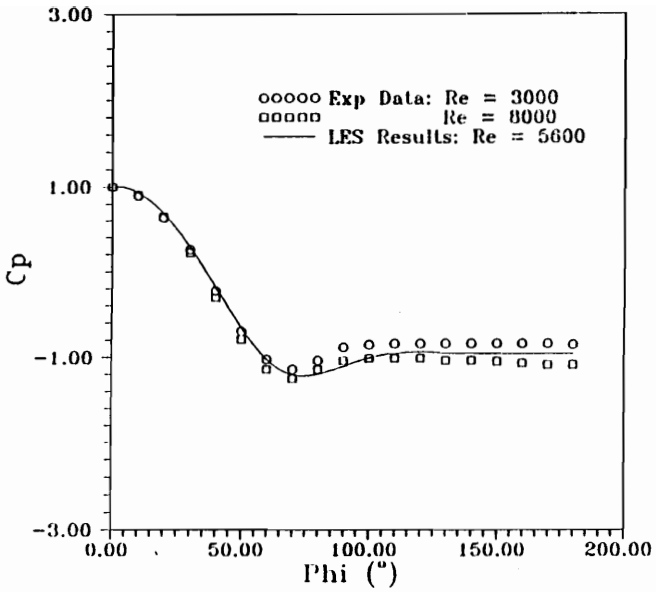

(a)

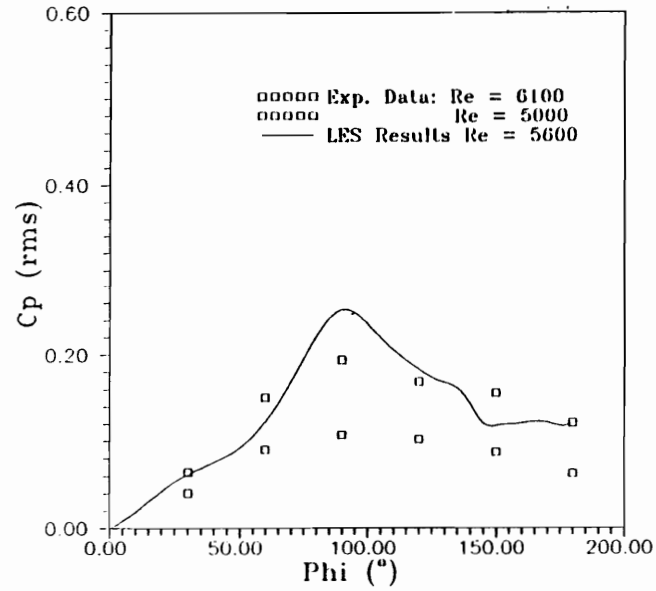

(b)

Figure 7.19. Comparsions of Experimental (Norberg, 1992) and LES Pressure Distributions Along the Cylinder Surface at Re = 5600; (a) Mean and (b) R.M.S.

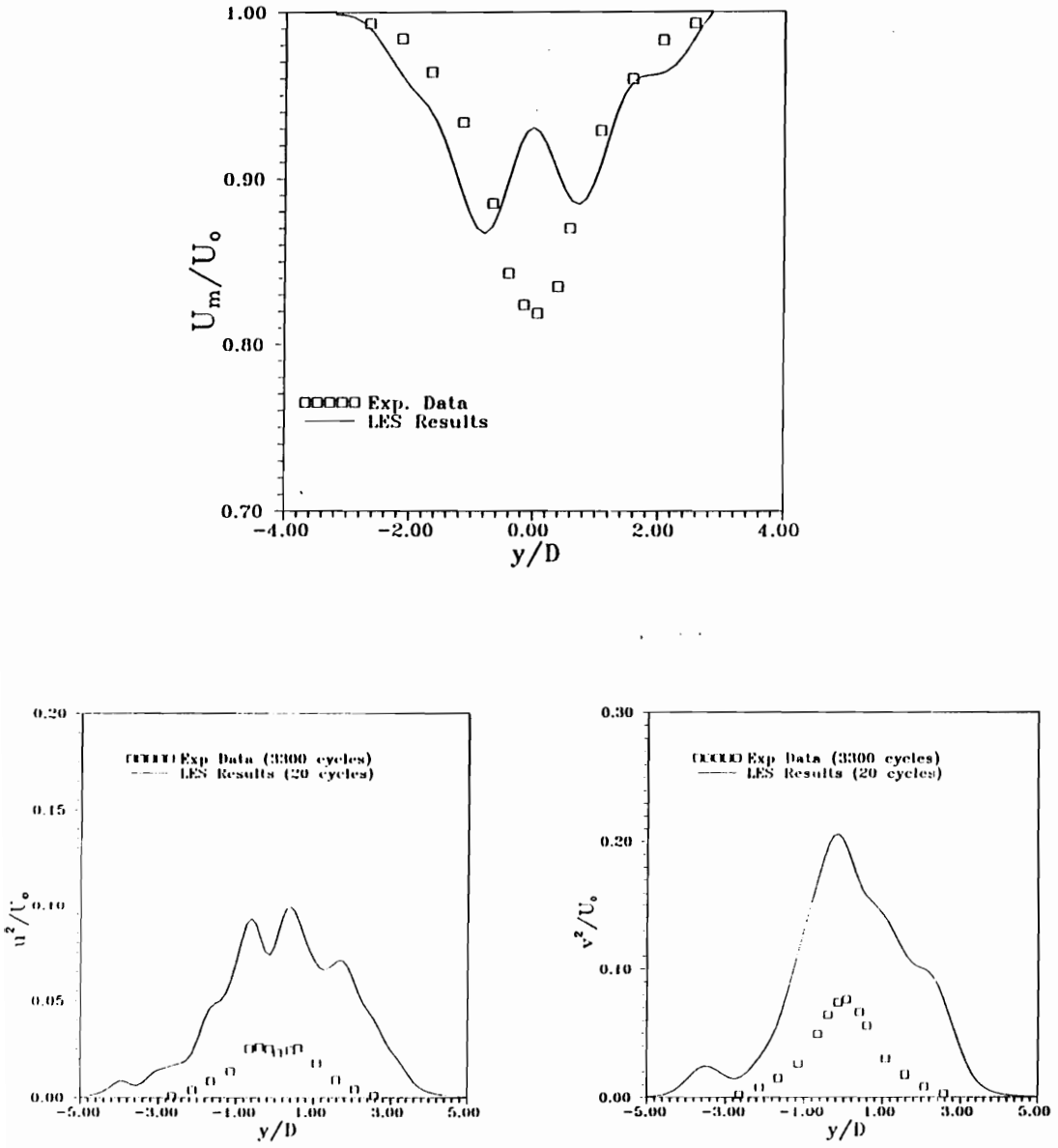

Figure 7.20. Mean Velocity and Normal Reynolds Stress Profiles of LES Results Compared to the Experimental Data of Zhou and Antonia (1993) at 10 Diameters Downstream of Cylinder for Re = 5600. LES Results Time-Averaged Over 20 Cycles and Experimental Data Time-Averaged Over 3300 Cycles.

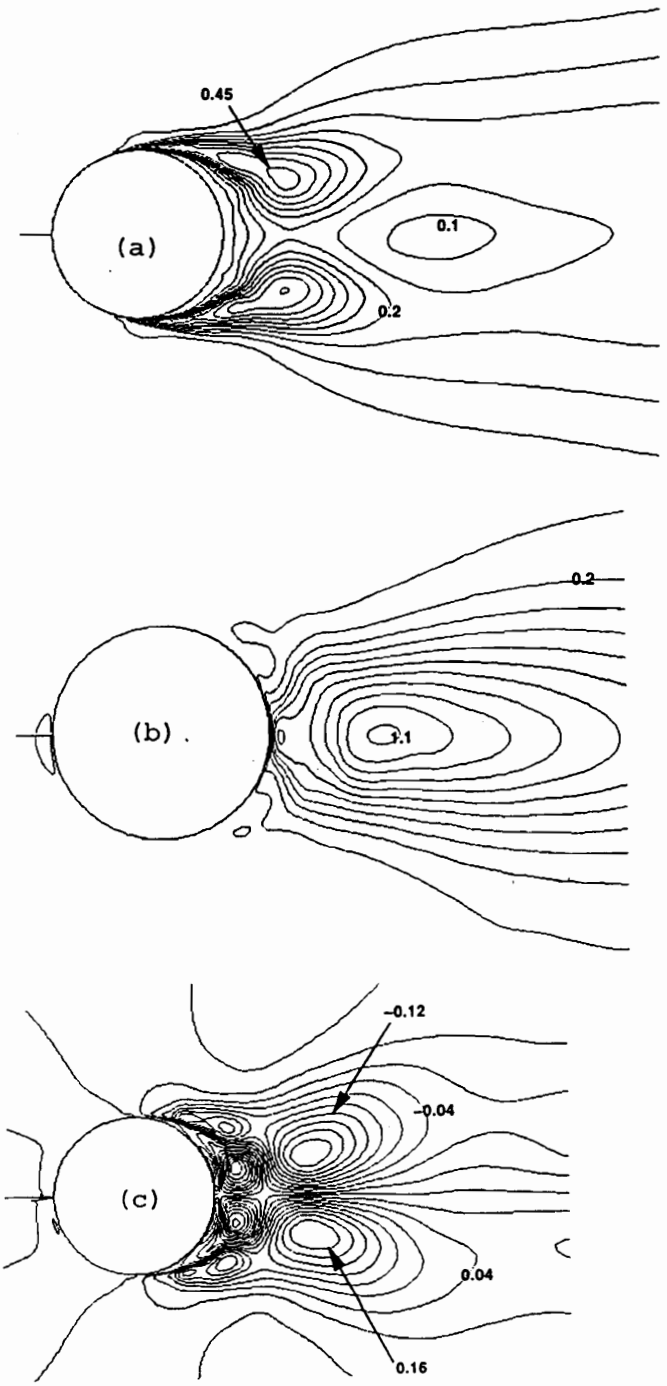

Figure 7.21. Contours of Mean Streamwise and Crossflow Reynolds Normal Stress and Mean Reynolds Shearing Stress in the Vicinity of the Cylinder Immediate Wake for Re = 5600; (a) Streamwise, (b) Crossflow and (c) Shear.

VITA

The author of this dissertation was born on September 25, 1951. He received his Bachelor of Science degree from the University of Rhode Island in 1976. For this degree, he majored in Civil Engineering with special emphasis on structural design. On June 4, 1976, the author began employment as an engineer at the then Norfolk and Western Railway Company in Roanoke, VA. After six months of management training, he was assigned to the building department in Roanoke as a structural designer. Two years later, he began his masters program at Virginia Tech in Civil Engineering with concentration in Geotechnics. Soon he was transferred by the Railway to the bridge department as a soils engineering, also in Roanoke. He completed his master degree in 1980. In that same year, the author moved back to his birthplace to undertake employment as manager of a marine geotechnical program at the University of Rhode Island. Two years later, he enrolled in the Ocean Engineering program at the University as a part-time student. In June of 1984, the author began employment as a Mechanical Engineer at his current employer; the Naval Undersea Warfare Center (NUWC) in Newport, RI. Since that time, his work at NUWC has been focused on computational fluid dynamics. He was later accepted by the Aerospace and Ocean Engineering Department at Virginia Tech for enrollment in the Ph.D. program for the 1990 Fall semester. The following semester, he transferred to the Engineering Science and Mechanics department with Dr. Saad Ragab as his major advisor. Completion of his Ph.D. program at Virginia Tech is anticipated for 1994. Being of age 42 now, no plans for future coursework in the near or far distance future is expected.

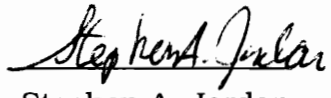

Stephen A. Jordan